# Intrathecal Magnetic Drug Targeting for Treatment of Central Nervous System Diseases

BY

INDU VENUGOPAL
M.S., University College London, 2010
B.S., Manipal Institute of Technology, 2009

THESIS

Submitted as partial fulfillment of the requirements for
the degree of Doctor of Philosophy in Bioengineering
in the Graduate College of the
University of Illinois at Chicago, 2017

Chicago, IL

Defense Committee:

Prof. Andreas Linninger, Chair and Advisor
Dr. Ali Alaraj, Neurosurgery, University of Illinois College of Medicine
Dr. Ankit Mehta, Neurosurgery, University of Illinois College of Medicine
Prof. Michael Stroscio, Bioengineering
Prof. Tolou Shokuhfar, Bioengineering

## DEDICATION

This thesis is dedicated to my parents – Latha and Venu. My mother's constant

encouragement and level-headedness, as well as my father's strength of character and

unending love, were the greatest factors in enabling me to achieving this milestone.

Without their belief in my abilities throughout my life, this dissertation would not have

been possible.

# ACKNOWLEDGMENTS

I would like to express sincere gratitude to my PhD advisor Prof. Andreas Linninger for his guidance and continuous support throughout my research. He has always given me the freedom to pursue my own ideas, and believed in my ability to do good research. I greatly appreciate his mentorship, without which this dissertation would not have been possible.

I would like to thank all my thesis committee members for their suggestions, feedback and guidance during my doctoral research. I am grateful to Dr. Ankit Mehta for his excellent advice and help with animal experiments, and Dr. Ali Alaraj for his guidance on the *in vitro* experimental research. I would like to thank Prof. Tolou Shokuhfar and Prof. Michael Stroscio for their valuable ideas and suggestions during my preliminary examination. I am also deeply indebted to Dr. Herbert Engelhard for his knowledge, kindness, support and advice throughout my PhD research.

I want to extend my gratitude to all my lab colleagues: Chih-Yang, Eric, Jacek, Sebastian, Mahsa, Narsi, Abhay, Nazia, Grant, Kevin, Ian, and Ying. They have all provided valuable suggestions about my work, and motivated me whenever necessary. It would have been impossible to complete the MRI imaging and analysis portion of this dissertation without Chih-Yang's knowledge and support. He has also helped me on several other occasions for resolving technical problems, both big and small, for which I will always be thankful to him. I would like to acknowledge the significant support that Eric provided for helping me get started with my intrathecal magnetic drug targeting research. I have also had many excellent technical discussions with Jacek, Sebastian and Ying which greatly aided my experimental research. Nazia was very instrumental in helping me complete the last phase of my PhD research. I was also extremely fortunate to have found wonderful

# CONTRIBUTION OF AUTHORS

Chapter 1 is a literature review that places my dissertation question in the context of the larger field, highlighting the significance of my dissertation work. It also details the specific aims of my doctoral research. Chapter 2 presents computational modeling of magnetic fields and simulation work which is relevant for the optimization of the experimental research detailed in the remaining chapters of this dissertation. Chapter 3 represents a published manuscript (*Venugopal, Indu, Sebastian Pernal, Taylor Fusinatto, David Ashkenaz, and Andreas Linninger. "Quantum Dot Conjugated Magnetic Nanoparticles for Targeted Drug Delivery and Imaging." Nano Biomedicine & Engineering 8, no. 1 (2016)*) for which I was the primary author and major driver of the research. Sebastian Pernal assisted in performing the synthesis of nanoparticles and editing of the final manuscript. Taylor Fusinatto and David Ashkenaz also helped with the synthesis and cell-based work detailed in this chapter. My research mentor, Dr. Andreas Linninger contributed to the writing of the manuscript and directed the research. Chapter 4 represents a published manuscript (*Venugopal, Indu, Sebastian Pernal, Alexandra Duproz, Jeromy Bentley, Herbert Engelhard, and Andreas Linninger. "Magnetic field-enhanced cellular uptake of doxorubicin loaded magnetic nanoparticles for tumor treatment." Materials Research Express 3, no. 9 (2016): 095010.*) for which I was the primary author. Sebastian Pernal and Jeromy Bentley assisted in developing the synthesis route for the doxorubicin loaded nanoparticles. Alexandra Duproz played a significant role in completing the cell-based assay work required for the publication. Drs. Herbert Engelhard and Andreas Linninger contributed to the writing of the manuscript and provided direction to the overall research. Chapter 5 details the *in vivo* animal work which proved the feasibility of the novel drug targeting technique detailed in

this dissertation. This work hasn't yet been published and I anticipate that this line of

research will be continued in the laboratory after I leave and that this work will ultimately

be published as part of a co- authored manuscript. Chapter 6 provided a quick summary of

the other chapters, and details the conclusions and future directions of my research

endeavors. Appendix Section A represents a published manuscript (*Lueshen, Eric, Indu

Venugopal, Joseph Kanikunnel, Tejen Soni, Ali Alaraj, and Andreas Linninger. "Intrathecal

magnetic drug targeting using gold-coated magnetite nanoparticles in a human spine model."

Nanomedicine 9, no. 8 (2014): 1155-1169.*) for which I was the second author. This section

presents the *in vitro* work which was used to demonstrate the efficacy of the novel drug

targeting technique which forms the basis of this dissertation. My work relating to this

manuscript involved synthesis and characterization of the magnetic nanoparticles, which

generated figure 43. I also aided in the construction of the bench-top human spine model

depicted in figure 44 as well as performing the nanoparticle collection efficiency

experiments.

**TABLE OF CONTENTS**

## LIST OF TABLES

# LIST OF FIGURES

# LIST OF ABBREVIATIONS

| | |
|---|---|
| BBB | blood-brain barrier |
| BCB | blood-CSF barrier |
| bpm | beats per minute |
| CE | collection efficiency |
| CNS | central nervous system |
| CSF | cerebrospinal fluid |
| DOX | doxorubicin |
| DOX-MNPs | doxorubicin-loaded magnetic nanoparticles |
| EDS | energy dispersive x-ray spectroscopy |
| EMF | electromagnetic field |
| FTIR | fourier transform infrared spectroscopy |
| FDA | Federal Drug Administration |
| FMT | fluorescence molecular tomography |
| GSH | glutathione |
| H&E | hematoxylin and eosin |
| IT-MDT | intrathecal magnetic drug targeting |
| MDT | magnetic drug targeting |
| MNP | magnetic nanoparticle |
| MRI | magnetic resonance imaging |
| MTT | 3-(4,5-dimethylthiazol-2-yl)-2,5-diphenyltetrazolium bromide |
| NIH | National institute of Health |
| NdFeB | neodynium-iron-boron |
| PBS | phosphate buffer solution |

| | |
|---|---|
| PEG | poly(ethylene glycol) |
| PLGA | poly(lactic-co-glycolic acid) |
| QD | quantum dot |
| SAED | selected area electron diffraction |
| SCI | spinal cord injury |
| SPIONs | superparamagnetic iron oxides nanoparticles |
| TE | time of echo |
| TEM | transmission electron microscopy |
| UIC | University of Illinois at Chicago |
| UV-Vis | Ultraviolet-Visible |
| ZP | zeta potential |

# 1. INTRODUCTION

## 1.1. <u>Summary</u>

The development of a wide spectrum of nanoparticles with tunable properties has the potential to change the medical landscape in terms of disease diagnosis, imaging, treatment, and prevention. The versatility of size and chemical composition make it relatively easy to tailor the functional properties of nanoparticles for specific medical applications. For example, nanomaterials have been used for reducing drug dosage, drug-related side effects and for sustained drug delivery purposes. In order to tailor nanoparticle properties for specific medical needs, they can synthesized with (i) surface ligands such as antibodies that enable targeting to specific cells/organs[1], (ii) tunable absorption and emission properties for biomedical imaging purposes[2], (iii) coatings that deter detection by macrophages or confer special properties[3] (iv) specific sizes for hyperthermia treatment[4] and many other similar useful properties.

In more recent times, there has been an increased focus on using them for delivering drugs to the central nervous system (CNS). Drug delivery to the CNS has always remained a challenge due to barriers such as the blood brain barrier and blood cerebrospinal fluid barrier, which hinder drug molecules from reaching the brain and spinal cord tissue.

In the past few decades, magnetic nanoparticles (MNPs) with special properties for medical applications in the CNS have been developed. Although MNP-based applications have been more commonly studied in the brain, a steady increase has been observed for use of MNPs in the spine. MNP delivery in the spine holds inherent anatomical and physiological challenges including cerebrospinal fluid (CSF) pulsations and difficulty in localization them to specific locations. This dissertation focuses on a novel technique of

1

using MNPs for CNS-based drug delivery, termed intrathecal magnetic drug targeting. This chapter begins with a detailed description of application of MNPs in the CNS, followed by the specific aims of my dissertation.

## 1.2. Use of magnetic nanoparticles for medical applications in the CNS

In the CNS, the primary advantage of using nanoparticles is the fact that they can be engineered to circumvent the blood-brain barrier (BBB), which prevents delivery of therapeutic molecules to the brain and spine. The BBB is an intricate network of blood vessels with tight capillary junctions that only permit entry of essential nutrients to the brain and spinal cord tissue, while preventing large molecules to pass through the vessel walls. In addition to the BBB, the blood-CSF barrier (BCB), which is formed by tight junctions between epithelial cells of choroid plexus, also facilitates transport of specific substances to CNS tissue, due to its distinct structure.

Overcoming the challenge of drug delivery posed by the BBB in the CNS has turned out to be the single-biggest challenge that is being currently tackled using nanotechnology Various types of nanoparticles are currently being developed for CNS applications, including solid lipid nanoparticles[5], liposomes[6], micelles[7], nanotubes[8], quantum dots[9], dendrimers[10] and polymeric nanoparticles[11]. One of the most promising types of nanoparticles for biomedical applications are magnetic nanoparticles. A simple MNP consists of a core made up of an inorganic magnetic material and a biocompatible surface coating that stabilizes the particle in physiological conditions.

In the CNS, there are three main clinical applications for MNPs - drug delivery via magnetic drug targeting (MDT), medical imaging and hyperthermia. MDT therapy entails injecting drug-loaded magnetic nanoparticles in a body fluid, and using external magnetic

fields to guide and retain the particles at specific sites in the body. The MNPs, when synthesized in a suitable size, can effectively penetrate the tissue at the localized region, and release the drug. MDT has potential to reduce drug dosage for CNS treatments due to targeted administration of therapeutic agents, as well as eliminate side effects of drugs by minimizing systemic distribution.

Most MNP applications in the CNS relate to treatments within the brain to overcome the BBB. Within the brain, nanoparticles have been mainly used for tumor treatment, to visualize the tumor site ([12], [13]), for site-specific chemotherapeutic drug delivery ([14], [15], [16]) and for hyperthermia treatment ([17], [18]). More recently, newer applications of MNPs for diseases in the spine have emerged, especially for treatment of spinal cord injury, bone regeneration and neuroprotection, which have been described in detail in the following sections. This shows us that MNPs have immense potential for treatment of CNS, and particularly spinal disease conditions, for which very few treatment options exist.

### 1.2.1. Magnetic drug targeting

In the late 1970s, Widder and colleagues introduced the concept of MDT ([19], [20]). MNPs below 20-30 nm in diameter display the phenomenon of superparamagnetism, and therefore, do not retain remnant magnetization after removal of an external magnetic field as shown in Figure 1. This is advantageous for drug delivery applications as it reduces undesirable particle aggregation. Newer MNP-based drug delivery and imaging agents incorporate novel cores such as doped iron oxide nanocrystals, metallic/alloy nanoparticles, and nanocomposites, which exhibit high magnetic moments.
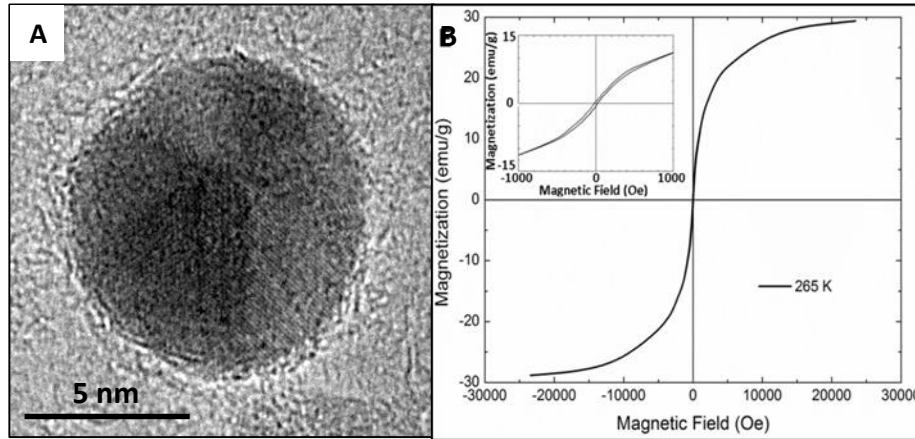
Figure 1. Properties of superparamagnetic nanoparticles (A). Transmission Electron Microscopy (TEM) image of a superparamagnetic magnetite nanoparticle with a diameter of 10 nm (B). SQUID (superconducting quantum interference device) magnetometry graph of the superparamagnetic nanoparticles. The hysteresis loop indicates no remnant magnetism in the MNPs after removal of magnetic field.

Most of the MDT-based applications in the CNS target the brain. For example, Chertok ([21], [22]) has shown the feasibility of using iron-oxide MNPs for magnetic resonance imaging (MRI) monitored drug delivery for brain tumors in rats. The toxicity of MNPs depends on numerous factors including the dose, composition, size, structure, surface chemistry, route of administration, biodegradability and pharmacokinetics [23]. Other experiments have shown that administration of commonly used iron oxide nanoparticles, cause no immunoreactivity or neuronal cell changes in the CNS, indicating potential for therapeutic applications within the spine [24]. There are several examples of prior *in vitro* and *in vivo* research, where MNPs with appropriate coating material have been well-tolerated at concentrations suitable for drug delivery ([25], [26]). However, some groups such as Pinkernelle and colleagues [12] have indicated that although MNPs are internalized by various primary neural cell cultures, they are primarily taken up by

microglia, which may be challenging for *in vivo* application of MNPs in the CNS, because of the possibility of immune system uptake.
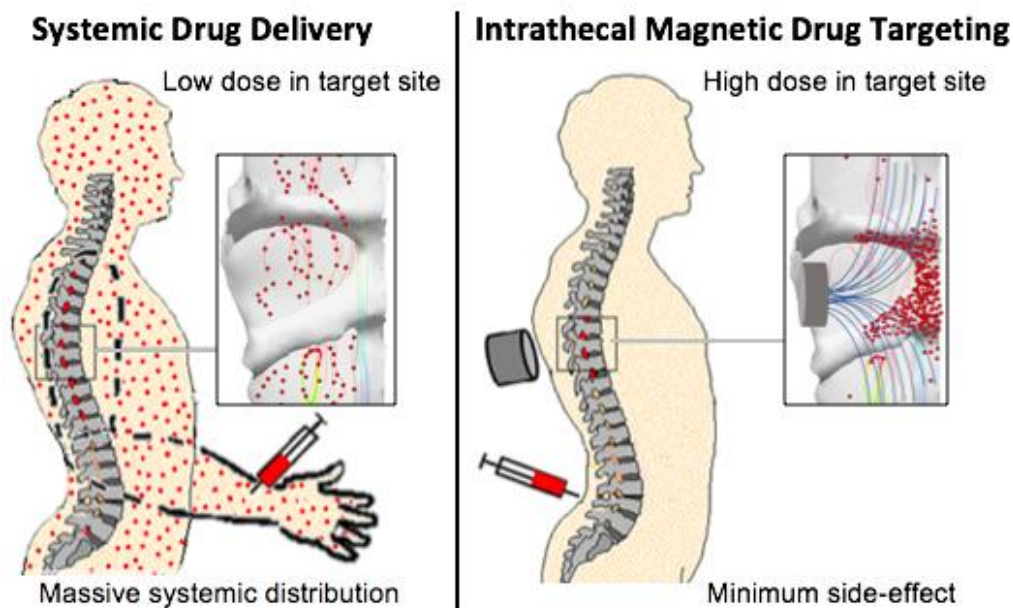


Figure 2. Systemic drug delivery (e.g. IV administration), leads to drug distribution throughout the body leading to high risk toxicity.  IT-MDT can target drugs to specific regions of the CNS, producing a highly concentrated effect.

Regarding MDT applications in the spine, the Linninger Research Group introduced a novel MDT technique for drug administration in the CNS, and specifically the spine, via drug-loaded MNP administration using the intrathecal route as shown in Figure 2. This technique will be explained in detail in the following chapters (Chapters 2 and 5). The feasibility of this technique was proved using *in vitro* and *in vivo* methods. The *in vitro* results have been published in the journal *Nanomedicine: Future Medicine*.

While MDT may be useful for targeting MNPs at diseased sites close to the body's surface, it may not be effective for deep tissue targeting. This is because magnetic field strength rapidly decreases with distance from the source (permanent magnets or electromagnets), making it hard to induce high magnetic gradients deep inside the body.

Researchers have proposed ways around this problem by using magnets and magnetizable implants near the target site within the body. For example, Fernández-Pacheco and colleagues [27] implanted permanent magnets into the kidney by a laparoscopic technique, and successfully localized intravenously administered magnetic FeC nanoparticles at required sites in the kidney.

Implant assisted-MDT has been explored by the Linninger Research Group for spinal applications with intrathecal delivery. Magnetizable implants in the spinal cord facilitated more efficient targeting of MNPs to desired locations when compared to MDT without the use of implants. We have shown that ferrous implants can result in large local magnetic field gradients at targeted regions along the spine, even at distances as large as 5 cm away from the externally applied magnetic field generated by rare earth magnets. Collection efficiency of MNPs at specific sites almost doubled with the use of appropriate implants in the spine. These results, which have been published by our group in the *Journal of Biomedical Nanotechnology* and *Nanomedicine: Future Medicine*, have been detailed in Chapter 2.

### 1.2.2. MNP-based electromagnetic field stimulation applications

Besides MDT, research efforts have been made towards using MNPs for electromagnetic field (EMF) stimulation applications. Jain [28] used iron oxide MNPs to enhance EMF stimulation in the spine for encouraging nerve cell regeneration. In their experiment, iron oxide nanoparticles embedded in a 3% agarose gel were implanted at the site of a spinal cord transection in rats, which were then stimulated. Significant improvements were achieved in locomotor assessment studies, with greater sprouting from mature neurons and axons near the lesion site. Similar results were also deduced by

Pal [29] who showed reduction in lesion volume and behavioral deficits after stimulating iron-oxide nanoparticles embedded in agarose gels to treat transected spinal cords of rats. *In vitro* experiments conducted by the group showed that EMF stimulation of MNPs helped decrease $H_2O_2$ mediated oxidative stress in primary human glioblastoma cells.

### 1.2.3. Magnetic nanoparticle- based hyperthermia treatment

In hyperthermia-based tumor treatment, MNPs are selectively heated by applying a high frequency alternating magnetic field. As the magnetic moments of the nanoparticles align and realign with the applied field, heat is generated and the tumor tissue is ablated. Hyperthermia is a minimally invasive treatment option for tumors, because the application of the high frequency field occurs outside the body. Magnetic hyperthermia is currently being used for tumor treatment in humans in the European Union. The company MagForce AG has received European Union wide regulatory approval for using hyperthermia to treat brain tumors.

Hyperthermia has been applied by few groups for treatment of metastatic spine tumors. Zadnik [30] determined that hyperthermia treatment of tumors in the vertebral body of rats did not damage their spinal cords. Similarly, Groves [31] used ferromagnetic nanoparticles to investigate MNP-based tumor thermoablation for metastatic spine disease. Their study showed no immediate neurologic deficit and minimal change in core temperature in the rats, showing potential for hyperthermia treatment for spine tumors.

### 1.2.4 Magnetic nanoparticles for tracking and imaging applications in the spine

Superparamagnetic iron oxides nanoparticles (SPIONs) have been actively investigated as MR imaging contrast agents for over two decades [32]. MNPs act as contrast agents for medical imaging, especially MRI because MNPs enhance proton relaxation of

specific tissues, making them visible during MRI.  With applications, such as bowel contrast agents (i.e., Lumiren® and Gastromark®) and liver/spleen imaging (i.e., Endorem® and Feridex IV®) [33] [34] already on the market, SPIONs have led way for MNPs into the clinic.

More recently, researchers have focused on MNPs for imaging and tracking in the spinal cord. Jendelova and colleagues [35] used iron-oxide nanoparticles for tracking transplanted cells in rat brain and spinal cord via MRI. They labelled rat bone marrow stromal cells and mouse embryonic cells with SPIONs to observe their migration to the injured spinal cord injury (SCI) site. Wang [36] labelled neural stem cells using gold-coated SPIONs to enhance their contrast under MRI. The cells were tracked for as long as a month after their administration into the spinal cord of rats. Hu [37] labelled human umbilical cord mesenchymal stem cells with SPIONs to visualize them via MRI, as these cell types have greater proliferation rates and better tolerance following transplantation as compared to bone marrow derived stem cells. Transplanted cells also showed potential for regeneration and recovery from SCI [38] - cells transplanted into focal areas of the spinal cord were visualized using T2-weighted MRI. The commercial MNP based imaging agent, Endorem ®, has also been used for imaging cells in the CNS, i.e., Sykova [39] labeled embryonic and mesenchymal stem cells with Endorem, and human CD34+ cells with magnetic microbeads, and intravenously administered them to rats with a cortical lesion or spinal cord lesion, which aided functional recovery in SCI induced rats.

Tracking magnetically labelled cells has also been performed in human patients with SCI. In the clinical trial performed by Callera and colleagues [40], autologous bone marrow CD34+ cells obtained from each patient were labelled with MNPs coated with a monoclonal antibody specific for the CD34 cell membrane antigen. Successful migration of

the cells to the lesion site following lumbar administration, was confirmed by T2-weighted MRI. No signal was observed in any other region of the CNS, showing movement of the cells only to the specific lesion site. Results from all the MNP-based cell tracking experiments clearly indicate that transplanted cells would preferentially migrate towards the lesion site even without any external coercion.

Another application of nanoparticles for imaging in the CNS, utilized fluorescence based imaging for detecting novel structures in the spine. Jia and colleagues [41] synthesized cobalt-ferrite MNPs loaded with a fluorescent dye, rhodamine B isothiocyanate, for observing the primo vascular system along the rat sciatic nerve. These subcutaneously administered fluorescent particles revealed a structure in the epineurium via confocal microscopy that otherwise difficult to observe.

## 1.3. Specific Aims

For treatment of debilitating diseases of the CNS, specifically the spine, current treatment protocols which utilize systemic drug delivery are ineffective due to the impermeability of the BBB and BCB. Therefore, we want to improve the methods of targeted drug delivery by increasing efficacy and specificity while diminishing side effects.

The main outcome of this dissertation is development of a novel technique called intrathecal magnetic drug targeting (IT-MDT) for treatment of CNS diseases. The accomplishment of this dissertation is proving the feasibility of using external magnetic forces to localize drug-loaded MNPs in the CNS at any desired location. The high efficiency of the magnet to localize drugs reduces its distribution to unwanted areas. The feasibility of this technique was demonstrated using extensive bench-work involving synthesis of MNPs and building an *in vitro* model to test the feasibility of localization. We loaded tumor drug

molecules on the MNP surface to create a functional drug vehicle, whose efficacy and cellular uptake was tested *in vitro* using glioma cells. Finally, we translated the *in vitro* results systematically to *in vivo* work using small animals.

In addition to the *in vitro* and *in vivo* work, we also developed the theory to guide the experiments and to quantify at each point the relationship between magnetic fields and collection of MNPs.

| | Application | Tests | NP platform | Ref |
|---|---|---|---|---|
| **Magnetic Drug Targeting** | Intrathecal magnetic drug targeting | *In vitro* models, computational simulations | Gold coated iron oxide nanoparticles | [42] |
| | Implant-Assisted Intrathecal magnetic drug targeting | *In vitro* models, computational simulations | Gold coated iron oxide nanoparticles | [43] |
| | Uptake of intravenously administered MNPs at SCI lesion site | *In vivo* study | Iron-oxide nanoparticles | [44] |
| **Electromagnetic field stimulation** | Nerve cell regeneration | *In vivo* study | Iron-oxide nanoparticles | [28] |
| | Treatment of transected spinal cords of rats, decrease in oxidative stress | *In vitro* and *in vivo* studies | Iron-oxide nanoparticles | [29] |
| **Hyperthermia treatment** | Palliative treatment of mammary adenocarcinoma tumor sites in the spine | *In vivo* study | Magnetic starch-coated iron oxide nanoparticles | [30] |
| | Treatment of metastatic spine disease (vertebral body) | *In vivo* study | Ferromagnetic nanoparticles | [31] |
| **Tracking/ Imaging** | Tracking movement of SPION labelled rat bone marrow stromal cells and mouse embryonic cells to SCI site | *In vivo* study | Iron-oxide nanoparticles | [35] |
| | Tracking iron-oxide nanoparticle labelled neural stem cells | | Superparamagnetic gold-coated iron-oxide nanoparticles | [36] |
| | Visualization of SPION labelled human umbilical cord mesenchymal stem cells via MRI and treatment of SCI | *In vitro* and *In vivo* studies | Superparamagnetic iron-oxide nanoparticles | [37], [38] |
| | Endorem labelled embryonic and mesenchymal stem cells for SCI treatment | *In vivo* studies | Dextran-coated superparamagnetic iron oxide nanoparticles (Endorem®) | [39] |
| | SCI treatment in humans using MNP labelled human autologous bone marrow cells (CD34+) | *In vivo* studies in humans | MNPs coated with a monoclonal antibody specific for the CD34 cell membrane antigen | [40] |
| Table 1. Applications of MNPs in the spine | | | | |

In this dissertation, emphasis has been laid on proving this technique for applications in the spine. Future work will focus on extending IT-MDT for applications throughout the CNS. The specific aims for this dissertation are as follows:

### 1.3.1. Modeling of Magnetic Fields and MNP Flux for Intrathecal Magnetic Drug Targeting (Chapter 2)

The dissertation begins with this chapter which aims at (1) modeling magnetic fields from permanent magnets and (2) developing a mathematical model for understanding the flux of MNPs during intrathecal magnetic drug targeting. Prediction of nanoparticle delivery to target tissue requires unification of magnetic field theory, fluid dynamics, and pharmacokinetics. The results and insights from this chapter are essential for computational modeling of the intrathecal magnetic drug targeting phenomenon, and for optimizing parameters in the *in vitro* and *in vivo* work of this dissertation.

### 1.3.2. Quantum dot conjugated magnetic nanoparticles for targeted drug delivery and imaging (Chapter 3)

Having proved that IT-MDT is feasible in an *in vitro* benchtop model (refer Appendix; section A), this chapter aimed at proving feasibility of IT-MDT *in vivo* in an animal model using a novel fluorescent magnetic delivery vehicle developed by loading quantum dots on the surface of our MNPs. This vehicle could be imaged during the drug delivery process using fluorescence molecular tomography. Detailed results from these experiments led to a journal publication [45].

### 1.3.3. Magnetic field-enhanced cellular uptake of doxorubicin loaded magnetic nanoparticles for tumor treatment (Chapter 4)

This part of the dissertation was focused on synthesizing a tumor-drug delivery vehicle for IT-MDT purposes, and understanding the effects of magnetic fields on the cellular uptake of this drug-loaded vehicle. The MNPs were loaded with the tumor drug doxorubicin, also commercially known as Adriamycin®, using a biocompatible polymer, and were characterized using several methods. Confocal microscopy, flow cytometry and MTT (3-(4,5-dimethylthiazol-2-yl)-2,5-diphenyltetrazolium bromide) assays were used to verify cellular uptake and cytotoxicity of these particles. Results from these experiments led to a journal publication [46].

### 1.3.4. Proving intrathecal magnetic drug targeting for localized delivery of therapeutics in the CNS using *in vivo* techniques (Chapter 5)

In this chapter, feasibility of IT-MDT technique was proved in Sprague Dawley rats using histology and magnetic resonance imaging. The results from these techniques were qualitatively and semi-quantitatively analyzed using *ImageJ* software.

### 1.3.5. Conclusion and Future Work (Chapter 6)

In this final chapter, the main conclusions from all the previous chapters, including the *in vitro* work in the Appendix section A has been enlisted and the future direction of this IT-MDT research has been provided.

## 2. MODELING OF MAGNETIC FIELDS AND MNP FLUX FOR INTRATHECAL MAGNETIC DRUG TARGETING

### 2.1.    Generation of magnetic field from a current source

### 2.1.1.   Introduction

All atoms consist of negatively charged electrons orbiting around positively charged nuclei. A moving electric charge constitutes an electric current, which implies that there is a current associated with every electron in an atom. Electrons fill the atom's orbitals in **pairs**. If one of the electrons in the pair spins upward, the other spins downward. It is impossible for both electrons in the pair to spin in the same direction. This forms the basis for a quantum-mechanical principle known as the **Pauli Exclusion Principle**. Therefore, in most atoms, the currents cancel each other, and the atom carries zero net current.

However, the atoms of ferromagnetic materials have several unpaired electrons with the same spin. Iron, for example, has four unpaired electrons with the same spin. This implies that cancellation of currents is not complete, and these atoms carry a net current. Usually, these atomic currents are all jumbled up as they are not aligned in a single plane, so that they average to zero on a macroscopic scale. However, if a ferromagnetic material is placed in a strong magnetic field then currents circulating in each atom become aligned to flow predominately in the plane perpendicular to the applied field. The currents can combine to form a macroscopic magnetic field reinforcing the alignment field.

Permanent magnets: In some ferromagnetic materials, the atomic currents remain aligned well after the alignment field is switched off, so the macroscopic field generated by these currents also remains. We call such materials permanent magnets. In

conclusion, all magnetic fields encountered in nature are generated by circulating currents. In this chapter, we aim to –

1. Develop a MATLAB program to visualize the generation of a magnetic field from an infinitely long wire carrying current in a single (z) direction.

2. Develop a MATLAB program to visualize the generation of a magnetic field from permanent magnets (2D and 3D visualization of the magnetic field).

3. Calculate force acting on MNPs generated by an external magnetic field.

### 2.1.2. Relevant Background and Methodology

Several groups have previously worked towards developing solutions for electrostatic, magnetostatic and electromagnetic problems using techniques such as finite-difference and finite-element method. A compilation of these studies has been provided in Table 2. Our group has also developed a simple solution for the generating magnetic fields surrounding a current carrying wire, as well as permanent magnets.

| Reference | Description |
|---|---|
| Bossavit (1998) [47] | Focused on derivations of Maxwell's equations, described a simple model problem in magnetostatics (bath cube problem) which was treated with the finite element technique to solve for the magnetic scalar potential. |
| Bartsch et al., 1992 [48] | Provided a robust numerical approach (finite difference Yee lattice method) for solving Maxwell's equations. Each Maxwell equation was transformed into a matrix expression and the algorithm used is a special case of finite difference formalisms. Examples of 2D and 3D electrostatics and magnetostatics problems was also provided in the paper. |
| Popa et al., 2006 [49] | Constructed a full multigrid type algorithm based on a "red-black" Gauss-Seidel multigrid procedure proposed by D. Braess (1981) for fast numerical solution of 2D Poisson equation, and applied the algorithm to a magnetostatic field problem in a plane domain to compute and plot the approximate values of the magnetic vector potential and magnetic field induction for different values of the mesh size and magnetization constant. The paper confirmed the efficiency and robustness of their method. |
| Van de Wiele et al., 2008 [50] | Compared two numerical schemes based on finite-difference and finite-element techniques for computation of Landau–Lifshitz equation for analyzing switching phenomena in magnetic thin films. Both approaches gave accurate results. FD method intrinsically preserved amplitude of magnetic dipoles. Finite element method was better at handling complex geometrical structures. |
| Van de Wiele et al., 2009 [51] | Compared two numerical schemes based on finite-difference and finite-element techniques for computation of Landau–Lifshitz equation for simulating magnetization dynamics in 3D particles. Concluded that both techniques were in accordance with each other. Finite element technique was better at handling curved boundaries in magnetostatics problems. |

| | |
|---|---|
| Bondeson et al., 2005 [52] | Introduced computational electromagnetics focusing on solving Maxwell's equations using finite difference method, finite element method, and the method of moments. The book provides solutions to several static, dynamic and quasi-static problems. A collection of MATLAB programs was also included for demonstrating the implementation and performance of the numerical methods. |
| Miltat et al., 2007 [53] | Provided a review of finite difference methods applied to micromagnetics (evaluating magnetic fields in small size magnetic bodies). Different approximations were discussed for exchange interactions and boundary conditions. Finite difference methods proved extremely efficient in terms of computation time due to extensive use of Fast Fourier Transforms. However, they displayed excessive discretization artifacts when dealing with curved geometries. |
| Humphries (1997) [54] | Provided detailed explanations on the basics of electrostatics, magnetostatics, electromagnetics as well as numerical techniques such as finite-element and finite difference methods for obtaining solutions for electromagnetics. The book lays special emphasis on the physical properties of electric and magnetic fields and how they can be translated to a numerical representation. |
| Wolfgang et al., 2006 [55] | Utilized integral equation method (IEM) for solving magnetostatic field problems. Matrix compression, fast multipole method, and other approaches were used to make IEM efficient, along with a superconvergent patch recovery method to improve post-processing results by increasing stability of the non-linear iterative solver. Non-linear problems with complex geometries were presented. |
| Lipnikov et al., 2010 [56] | Utilized mimetic finite difference (MFD) method for numerical treatment of magnetostatic field problems. Linear algebraic form of the MFD scheme, its implementation, and uniqueness were also discussed. The accuracy of the method was demonstrated by solving numerically a few academic problems and a realistic engineering problem. |
| Sch¨oberl (2009) [57] | Provides formulations for all the Maxwell equations, and solves them using the finite element method. The chapter discussed partial differential equations, variational formulations, edge elements, high order elements, preconditioning, a posteriori error estimates. |
| Sarma (1976) [58] | Presented finite-element formulation for 3D numerical solutions of magnetostatic field problems. The approach utilized the vector potential concept in which the energy function is minimized over the entire region by means of the finite-element method and the resultant set of nonlinear algebraic equations were solved through iterative schemes. End-zone fields of aerospace homopolar alternators and solid-rotor induction motors were analyzed as examples. |
| Trowbridge (1972) [59] | Reviewed partial differential and integral equation formulations for solving non-linear magnetostatic field problems. Also, provided a brief survey of the literature of computer programs developed in various countries. Presented results of 2D and 3D problems analyzed by programs like GFUN and TRIM. |
| Friedman (1984) [60] | Presented a new finite element method for obtaining numerical solutions of a general magnetostatic problem. The method was formulated using an integral formulation, and calculates the magnetic flux density both inside and outside the ferromagnetic material kept in a magnetic field. |
| Burfine et al., 1966 [61] | Provided a method for solving variable permeability 2D and axially symmetric magnetostatic problems using a computer code called NUTCRACKER written in ALGOL 60 programming language. |
| Table 2: Compilation of studies on magnetostatics | |

In the next section, a brief derivation of the magnetostatics is given. This theory is used in the case studies at the end of the chapter.

<u>Maxwell's equations</u>: The classical problem of magnetostatic field theory starts with the Maxwell's equations:

$$\vec{\nabla} \times \vec{H} = \vec{J} \qquad (1)$$

$$\vec{B} = \mu\vec{H} \qquad (2)$$

$$\vec{\nabla} \cdot \vec{B} = 0 \qquad (3)$$

where $\vec{H}$ is the magnetic field strength, $\vec{B}$ is the magnetic flux density, $\vec{J}$ is the current density that generates the magnetic field and **μ** is the magnetic permeability which is a function of the magnetizing material under consideration. Eq (1) states that the curl of the magnetic field strength gives us the current generated in the system due to the presence of the magnetic field. Eq (2) states that the magnetic flux density is the product of the magnetic field strength and magnetic permeability. Eq (3) states that the magnetic flux density is always divergence free (currents in the system do not share this property).

For a magnetic phenomenon induced by electrical currents, it is not convenient to solve for the magnetic flux density, $\vec{B}$, directly. Instead, it is customary to introduce an auxiliary field $\vec{A}$, known as a magnetic vector potential, which makes it easier to solve for the $\vec{B}$ field. We will later show that without a current, e.g. in a permanent magnet, this approach can be further simplified using a simple scalar potential field, $\phi$. The introduction of the simple vector potential field will prove to be very convenient for obtaining solution of magnetic fields induced by currents.

<u>Relationship of the magnetic flux density ($\vec{B}$) to the magnetic vector potential ($\vec{A}$)</u>: In the classical vector potential approach, the system of the three equations (1-3) can be

further simplified by the introduction of an auxiliary variable vector $\vec{A}$ (representing the magnetic vector potential) which is related to the magnetic flux density by the equation:

$$\vec{\nabla} \times \vec{A} = \vec{B} \qquad (4)$$

The curl of $\vec{A}$ results in $\vec{B}$ that points along the axis of the rotation of $\vec{A}$ and whose length corresponds to the speed of the rotation of $\vec{A}$. Suppose the $\vec{A}$ field has three components in x, y and z directions given by Ax, Ay and Az respectively, then

$$\vec{\nabla} \times \vec{A} = \vec{B} = \left(\frac{dAz}{dy} - \frac{dAy}{dz}\right)\hat{\imath} + \left(\frac{dAx}{dz} + \frac{dAz}{dx}\right)\hat{\jmath} + \left(\frac{dAy}{dx} + \frac{dAx}{dy}\right)\hat{k}$$

Eq (3) is now automatically satisfied by the identity

$$\vec{\nabla}.\left(\vec{\nabla} \times \vec{A}\right) = 0 \qquad (5)$$

On eliminating $\vec{B}$ and $\vec{H}$ from eqs (1) and (2) we have the governing vector potential equation in terms of only the magnetic vector potential:

$$\vec{\nabla} \times \frac{1}{\mu}\left(\vec{\nabla} \times \vec{A}\right) = \vec{J} \qquad (6)$$

Eq (6) gives the relationship between the source current $(\vec{J})$ and the magnetic vector potential $(\vec{A})$

---

**Proof that $\vec{\nabla} \cdot \vec{B} = 0$ for any $\vec{B} = (\vec{\nabla} \times \vec{A})$**

Let $\vec{B} = (b_1 \ b_2 \ b_3)$ ; $\vec{\nabla} \cdot \vec{B} = \frac{db_1}{dz} + \frac{db_2}{dz} + \frac{db_3}{dz}$

$(b_1 \ b_2 \ b_3) = (b_{21}z - b_{31}y \qquad b_{31}x - b_{11}z \qquad b_{11}y - b_{21}x)$

$\vec{\nabla} \cdot \vec{B} = (b_{21}z - b_{31}y) + (b_{31}x - b_{11}z) + (b_{11}y - b_{21}x) = 0$

---

Relationship between source current ($\vec{J}$) in one direction (z) and magnetic field ($\vec{B}$):

   In this case, we consider the current density vector $\vec{J}$ as an infinitely long wire in the z-direction ($J_z$). This implies that the x and y components of the current density vector $\vec{J}$ is zero ($J_X = J_Y = 0$). The resulting magnetic field $\vec{B}$ must therefore, be symmetric along the z-direction (Figure 3).

 Let,

Figure 3. A uniform current density vector ($\vec{J}$) in the z-direction generates a magnetic field ($\vec{B}$) in the x-y plane which is symmetric along the z-axis.

$$\vec{B}^T = (b_1 \quad b_2 \quad b_3)$$

Therefore,

$$\frac{db_1}{dz} = \frac{db_2}{dz} = \frac{db_3}{dz} = 0 \qquad (7)$$

$$\vec{J} = (\vec{\nabla} \times \vec{B}) = (0 \quad 0 \quad J_z) \qquad (8)$$

This implies that

$$\frac{db_3}{dx} = \frac{db_3}{dy} = 0 \qquad (9)$$

Eq (8) and (9) imply that

$$b_3 = 0 \qquad (10)$$

This implies that $\vec{B}$ lies in a planar x-y field

$$(\vec{\nabla} \times \vec{B}) = (0 \quad 0 \quad J_z)$$

This can be reduced to

19

$$b_{11}x + b_{21}y = 0 \qquad (11)$$

$$b_{11}x + b_{21}y = J_z \qquad (12)$$

We now introduce a scalar field which makes eqs (11) and (12) much easier to solve

Let $\phi$ be a scalar field with $\vec{\nabla}\phi = (\phi_X \quad \phi_Y)$ such that

$$b_1 = \phi_Y \quad \text{and} \quad b_2 = -\phi_x$$

$$b_{1x} = \phi_{yx} \quad b_{1y} = \phi_{yy} \quad b_{2y} = -\phi_{xy} \quad b_{2x} = -\phi_{xx}$$

Substituting in eqs 1i and 1j, we get

$$\phi_{yx} - \phi_{xy} = 0 \qquad (13)$$

$$\phi_{yy} + \phi_{xx} = J_z \qquad (14)$$

Eq (14) is a simple diffusion equation that we have attempted to solve via MATLAB

### 2.1.3. Generation of a magnetic field from a current source: Parameters and Method

A 2D Cartesian mesh of 21 elements was used to generate the vacuum space in which the computations were performed. A constant current density source ($J_z$) of 10000 A/m$^2$ was applied at the center of this mesh in the z direction. This acted as a source term. This generates the scalar field $\phi$, as determined by eq (14).

Initialization conditions: The initial value of the $\phi$ field in all the elements was set to 0.

The initial current density ($J_z$) was applied in a single element at the center of the mesh, which acted as a source term.

Boundary conditions: The boundary values of the $\phi$ field was set to 0.

Assumptions:

1. The boundary region represents an infinite distance at which $\phi$ field value is zero.

2. The magnetic permeability of vacuum ($\mu_0$) is 1.25 x 10$^{-6}$ N·A$^{-2}$.

3. Each element has a uniform dimension of 1mm x 1mm.

### 2.1.4. Results

### ϕ-field

As seen in Figure 4, magnitude of ϕ field value is highest at center of the mesh (closest to the current source). The resulting ϕ field is also not a dirac delta function. We have also verified this by reducing the mesh size by half, 1/10th and 1/100th times, and the ϕ field does not tend to become a dirac function (Figure 5). This is expected as the ϕ field is obtained from a diffusion equation from current source at the center of the mesh.
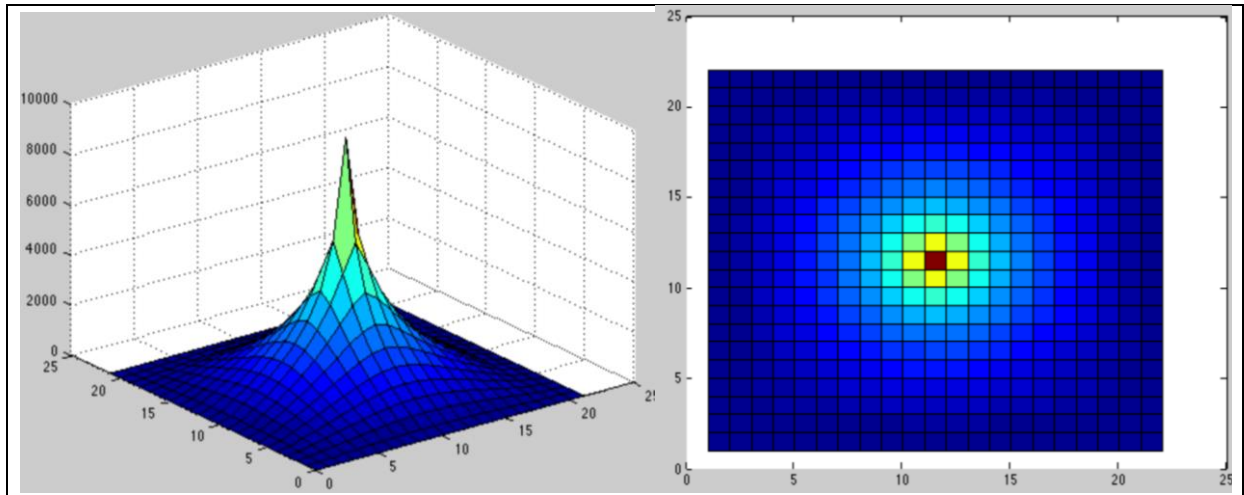


Figure 4. The magnitude of the ϕ field (highest at center and decreases towards the border)
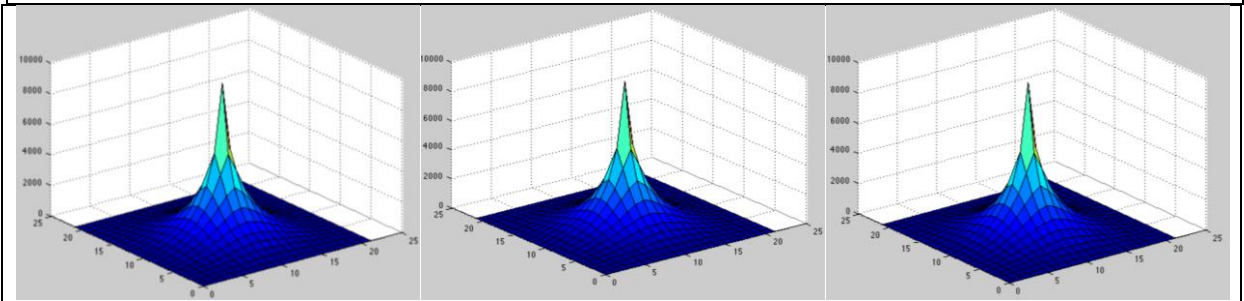


Figure 5. Plot showing the magnitude of the ϕ field with mesh sizes of 0.5 mm, 0.1 mm and 0.01 mm (left to right) respectively

**Gradient of scalar field ($\vec{\nabla}\phi$)**
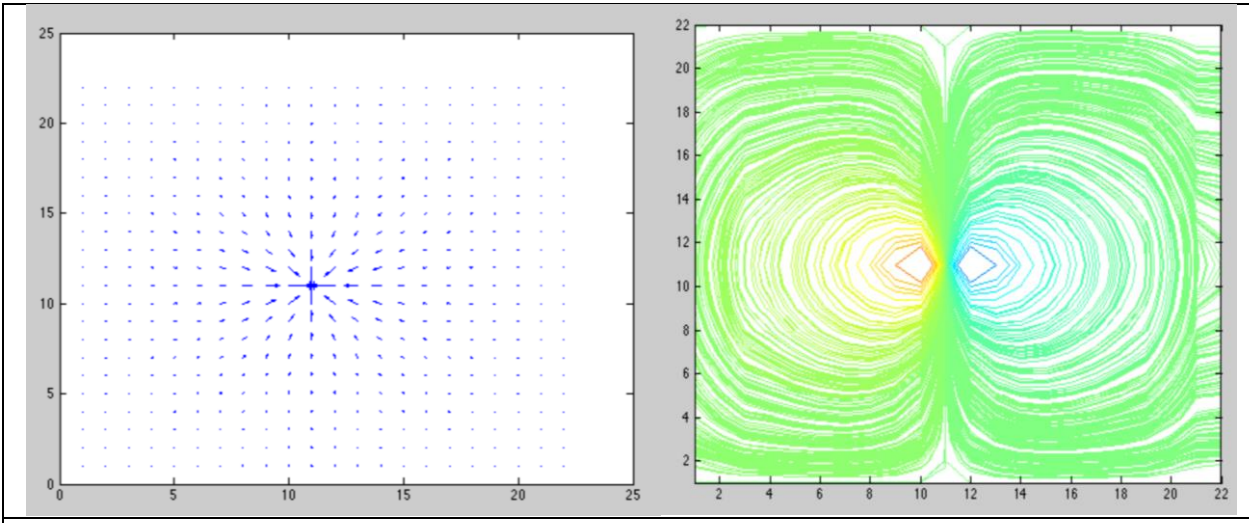


Figure 6. Vector plot of the $\vec{\nabla}\phi$ field and contour plot of the magnitude of the $\vec{\nabla}\phi$ field

**Magnetic flux density field ($\vec{B}$ field)**
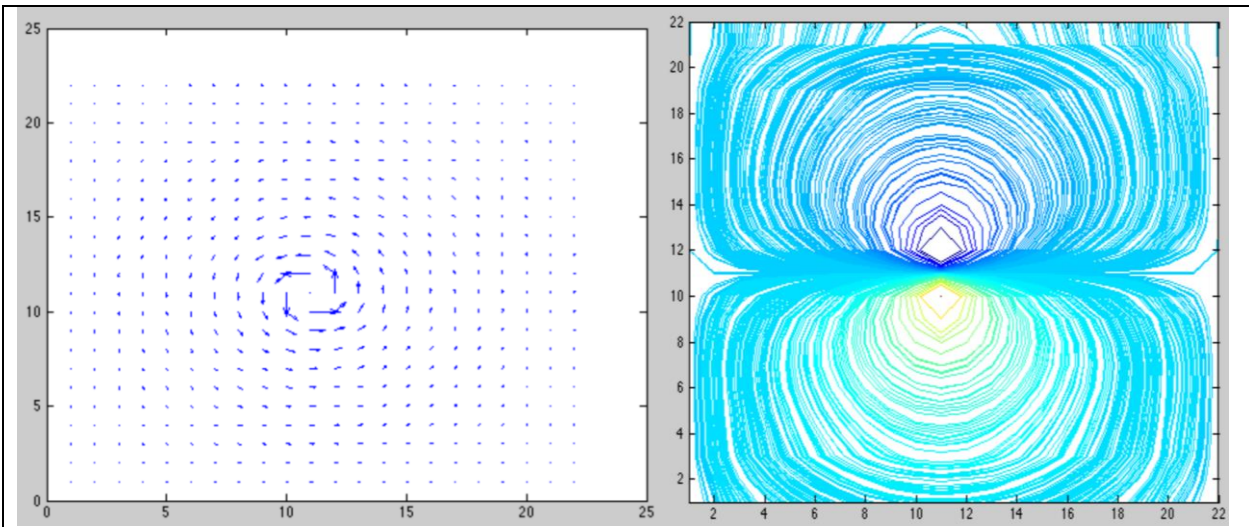


Figure 7. Vector plot of the $\vec{B}$ field and contour plot of the magnitude of the $\vec{B}$ field

Magnetic field lines (streamlines) can be obtained by following the $\vec{B}$ vector field from the beginning of the surface to the end.

**Obtaining the $\vec{A}$ field**

$$\vec{\nabla} \times \vec{A} = \vec{B}$$

Therefore,

$$\left(\frac{dA_z}{dy}\right) - \left(\frac{dA_y}{dz}\right) = B_x = \frac{d\phi}{dy}$$

$$\left(\frac{dA_x}{dz}\right) - \left(\frac{dA_z}{dx}\right) = B_y = -\frac{d\phi}{dx}$$

We know that our $\vec{B}$ field lies in the x-y plane. Therefore, the $\vec{A}$ field needs to lie in z plane.

$$\vec{A}.\vec{B} = 0$$

$$A_x B_x + A_y B_y + A_z B_z = 0$$

We know that $\qquad\qquad B_z = 0 \quad \text{and} \quad B_x \text{ \& } B_y \neq 0$

$$A_x B_x + A_y B_y = 0$$

One solution for this is $A_x = A_y = 0$, which corroborates our understanding of the $\vec{A}$ field

This implies that the terms $\left(\frac{dA_y}{dz}\right)$ and $\left(\frac{dA_x}{dz}\right)$ are zero. Therefore, $\vec{A} = (0 \quad 0 \quad A_z) = (0 \quad 0 \quad \phi)$

Therefore, plot of $\vec{A}$ field would be the same as plot of gradient of the $\phi$ field.

**Magnetic vector potential field ($\vec{A}$ field)**
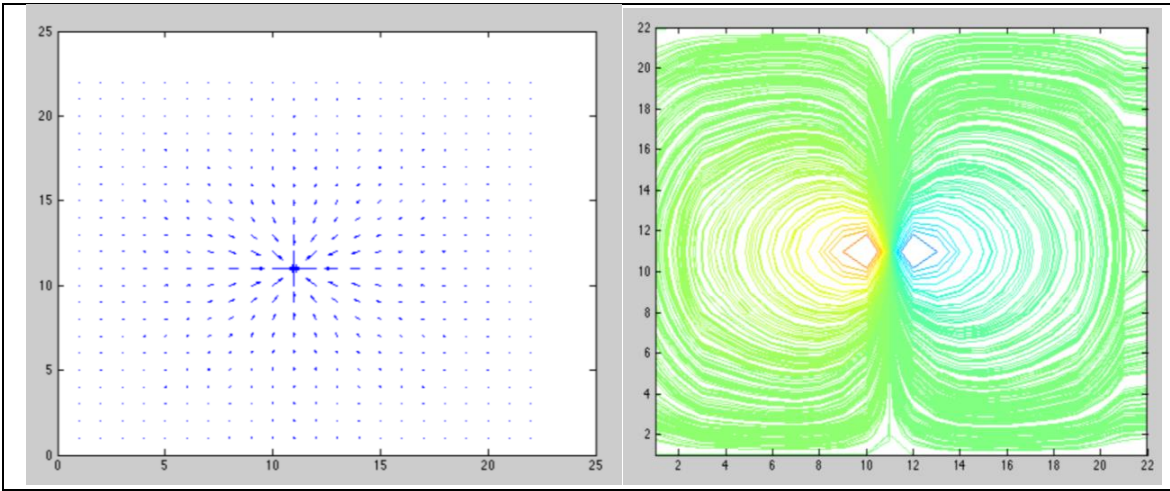


Figure 8. Vector plot of the $\vec{A}$ field and contour plot of the magnitude of the $\vec{A}$ field

## 2.2.    Generation of magnetic field surrounding a permanent magnet

### 2.2.1.  Introduction

Relationship between magnetic field $\overrightarrow{H_m}$ and scalar magnetic potential $V_m$ in current free regions

The region surrounding a permanent magnet is a current free region. Therefore, in this region,

$$\overrightarrow{\nabla} \times \overrightarrow{H_m} = \vec{J} = 0 \tag{15}$$

Therefore, it is possible to define a scalar magnetic potential such that $V_m$, such that

$$\overrightarrow{H_m} = -\overrightarrow{\nabla} V_m \tag{16}$$

Where, $V_m$ is the magnetic scalar potential

This is due to the known relationship that if the curl of a vector is equal to zero, then it can always be represented as the gradient of a scalar potential.

---

**PROOF THAT AN IRROTATIONAL VECTOR FIELD IMPLIES EXISTENCE OF POTENTIAL FUNCTION**

Let $S(x,y,z)$ be a scalar function. Then its gradient can be written as –

$$\nabla S(x, y, z) = \frac{dS(x,y,z)}{dx}\hat{\imath} + \frac{dS(x,y,z)}{dy}\hat{\jmath} + \frac{dS(x,y,z)}{dz}\hat{k}$$

By assumption, let V be a vector such that –

$$\vec{V} = \nabla S$$

Now,

$$\mathbf{curl}\,\vec{V} = \vec{\nabla} \times \vec{V} = \left(\frac{dVz}{dy} - \frac{dVy}{dz}\right)\hat{\imath} + \left(\frac{dVx}{dz} - \frac{dVz}{dx}\right)\hat{\jmath} + \left(\frac{dVy}{dx} - \frac{dVx}{dy}\right)\hat{k}$$

Due to our assumption-

$$Vx = \nabla Sx = \frac{dS(x,y,z)}{dx} \quad \text{and } Vy = \nabla Sy = \frac{dS(x,y,z)}{dy} \text{ and } Vz = \nabla Sz = \frac{dS(x,y,z)}{dz}$$

Substituting these in the curl V equation,

$$\mathbf{curl}\,\vec{V} = \vec{\nabla} \times \nabla S = \left(\frac{d^2S}{dydz} - \frac{d^2S}{dydz}\right)\hat{\imath} + \left(\frac{d^2S}{dzdx} - \frac{d^2S}{dxdz}\right)\hat{\jmath} + \left(\frac{d^2S}{dxdy} - \frac{d^2S}{dydx}\right)\hat{k} = 0$$

Therefore, if curl $\vec{V}$ = 0, our assumption that $\vec{V} = \nabla S$ is correct. This proves that an irrotational vector field (curl =0) can be described as gradient of a scalar field

---

Constitutive relationship between applied magnetic field and magnetic flux density is as follows

$$\vec{B} = \mu(\overrightarrow{H_m} + \vec{M}) \qquad (17)$$

where, $\vec{B}$ is magnetic flux density, $\overrightarrow{H_m}$ = magnetic field generated outside the permanent magnet, $\vec{M}$ = magnetization value of any magnetizable material (like iron/magnetic nanoparticles) present near the permanent magnet and $\mu = \mu_0 * \mu_r$ (Absolute magnetic permeability of vacuum *Relative magnetic permeability of the medium under consideration- constant values)

By substituting eq (16) in eq (17), we get:

$$\vec{B} = \mu(-\overrightarrow{\nabla} V_m + \vec{M}) \qquad (18)$$

By substituting the eq (18) in eq (3), we get:

$$-\vec{\nabla} \cdot (\mu\overrightarrow{\nabla} V_m - \mu\vec{M}) = 0 \qquad (19)$$

As no magnetizable material is being considered near the magnet, $\vec{M}$ =0, and the eq (19) reduces to:

$$\vec{\nabla} \cdot \left(\mu\overrightarrow{\nabla} V_m\right) = 0 \qquad (20)$$

This is in a scalar form for which solutions are readily obtainable.

<u>Generation of magnetic field both inside and surrounding a neodymium- iron-boron permanent magnet</u>

In this case, the magnetic field is not coming from a current source, but from a permanent magnet which acts as a source of magnetic activity which is typically introduced into the domain by a proper choice of boundary fluxes (like a neumann boundary condition). If we were to model the magnetic field within the permanent magnet

along with the surrounding region using scalar magnetic potentials, the following

theory/equations can be used:

The permanent magnet can be considered as a current carrying wire that generates

a magnetic field $\overrightarrow{H_c}$ that can be determined by using the Biot-Savart law:

$$\overrightarrow{H_c} = \frac{1}{4\pi} \int \frac{J \times (r - r')}{(r - r')3} \, dv \qquad (21)$$

In this case, the magnetic field $\vec{H}$ must incorporate both $\overrightarrow{H_c}$ (generated due to the permanent
magnet) as well as $\overrightarrow{H_m}$

$$\vec{H} = \overrightarrow{H_c} + \overrightarrow{H_m} \qquad (22)$$

Also, the magnetic flux density represented earlier by eq (2c) now becomes

$$\vec{B} = \mu(\overrightarrow{H_m} + \overrightarrow{H_c} + M) \qquad (23)$$

Using this equation and performing the same substitutions as shown earlier, eq (19) now

becomes:

$$\vec{\nabla} \cdot \left( \mu \vec{\nabla} V_m - \mu \overrightarrow{H_c} - \mu \overrightarrow{M} \right) = 0 \qquad (24)$$

This equation can be used to generate magnetic field within the permanent magnet,

in the surrounding regions, as well as inside a magnetizable object in the permanent

magnet's vicinity.

### 2.2.2. Simulation of a 2D permanent magnetic field: Parameters and Method

A 2D Cartesian mesh of 21 elements was used to generate the vacuum space in

which the computations were performed. A permanent magnet of $1.3 \times 10^{-5}$ T was

considered at the center of the mesh. This generates a magnetic scalar potential field $V_m$

from which the magnetic field $\vec{H}$ and magnetic flux density field $\vec{B}$ can be generated.

Initialization conditions:

Internal vacuum area: The initial value of the $V_m$ in all the elements was set to 0.

The permanent magnet conditions were applied at 4 elements at the center of the mesh.

Boundary conditions:

- The value of $V_m$ was set to zero at the boundaries of the mesh, which represented the magnetic scalar potential value at infinity.

- Neumann boundary condition was applied at the boundary of the permanent magnet. As we know the B value ($1.3 \times 10^{-5}$ T) and the $\mu$ value of the magnet ($1.05 * 1.25 * 10^{-6}$), we can determine the value of the magnetic field H at the surface of the magnet (which is equal to the negative gradient of $V_m$ at the surface) by using equation:

$$\vec{B} = \mu(\vec{H}) = \mu(-\vec{\nabla} V_m)$$

This value was of $(-\vec{\nabla} V_m)$ determined to be 10 A/m. As we know that the magnetic field lines are generated only from the top and bottom surfaces of the magnet and not from the sides,



Figure 9. Magnetic field values $\vec{H}$ (flux generated by the magnetic scalar potential Vm) at the boundaries of the permanent magnet

$\vec{B}|_{y=0}$ = 10 A/m (north face of the magnet)

$\vec{B}|_{y=1}$ = -10 A/m (south face of the magnet)

$\vec{B}|_{x=0,1}$ = 0 A/m (sides of the magnet)

Assumptions

1. The boundaries of the mesh represents an infinite distance at which $V_m$ field = 0.

2. The magnetic permeability of vacuum ($\mu_0$) is $1.25 \times 10^{-6}$ N·A$^{-2}$.

3. The magnetic permeability of the magnet ($\mu$) is $1.05 \times 1.25 \times 10^{-6}$ N·A$^{-2}$.

4. Each element has a uniform dimension of 1mm x 1mm.

## 2.2.3. Results

### Magnetic Scalar potential ($V_m$)
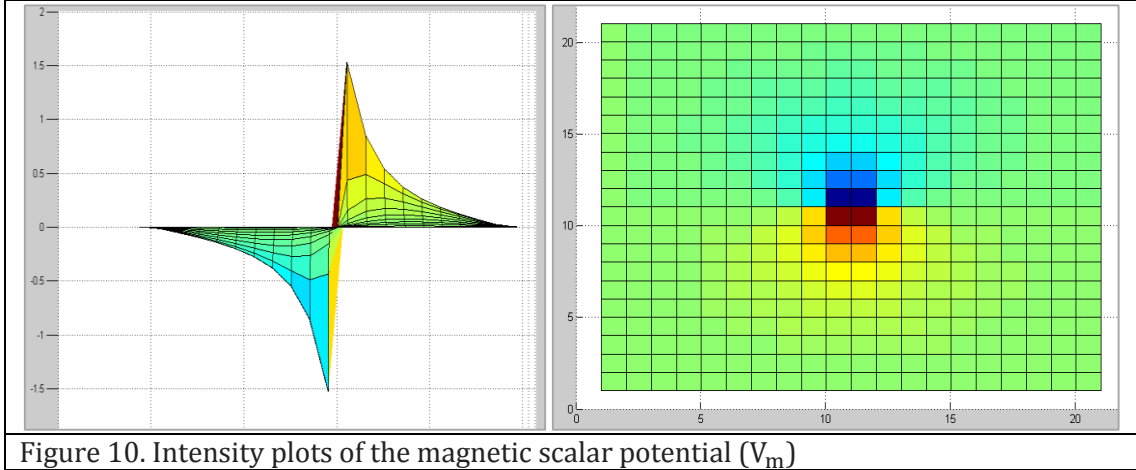


Figure 10. Intensity plots of the magnetic scalar potential ($V_m$)

### Magnetic field ($\vec{H}$)
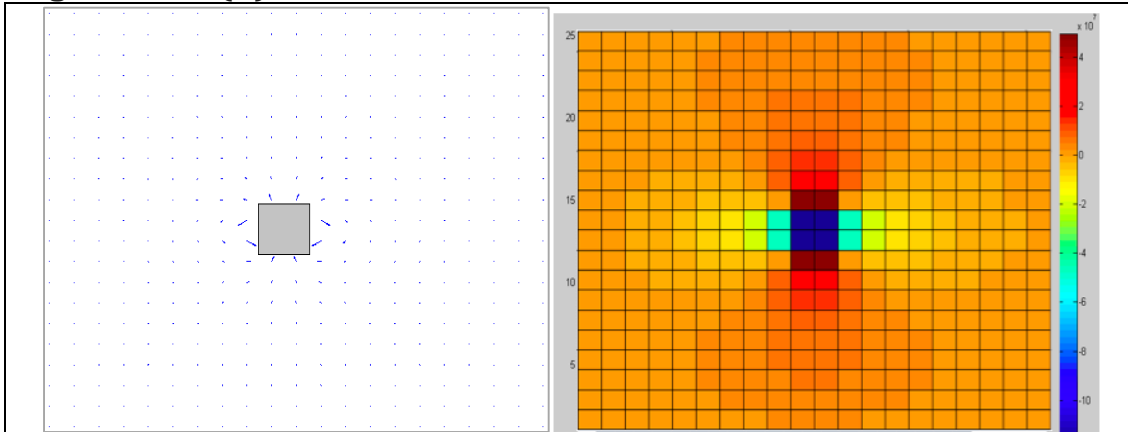


Figure 11. Vector and intensity plots of the magnetic field ($\vec{H}$)

### Magnetic flux field ($\vec{B}$)
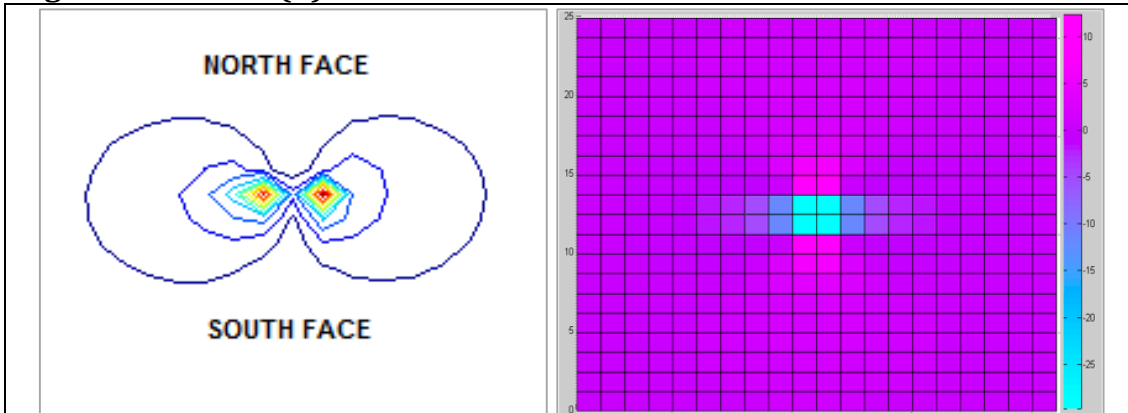


Figure 12. Contour (left) and intensity (right) plots of the magnetic flux density ($\vec{B}$)

28

## 2.2.4. Simulations of magnets used in the Linninger group for the IT-MDT experiments

Detailed description of the experiments can be found in the paper –

*Lueshen, Eric, et al. "Intrathecal magnetic drug targeting using gold-coated magnetite nanoparticles in a human spine model." Nanomedicine 9.8 (2014): 1155-1169.*

**Targeting magnet 1 of strength 0.396 T**
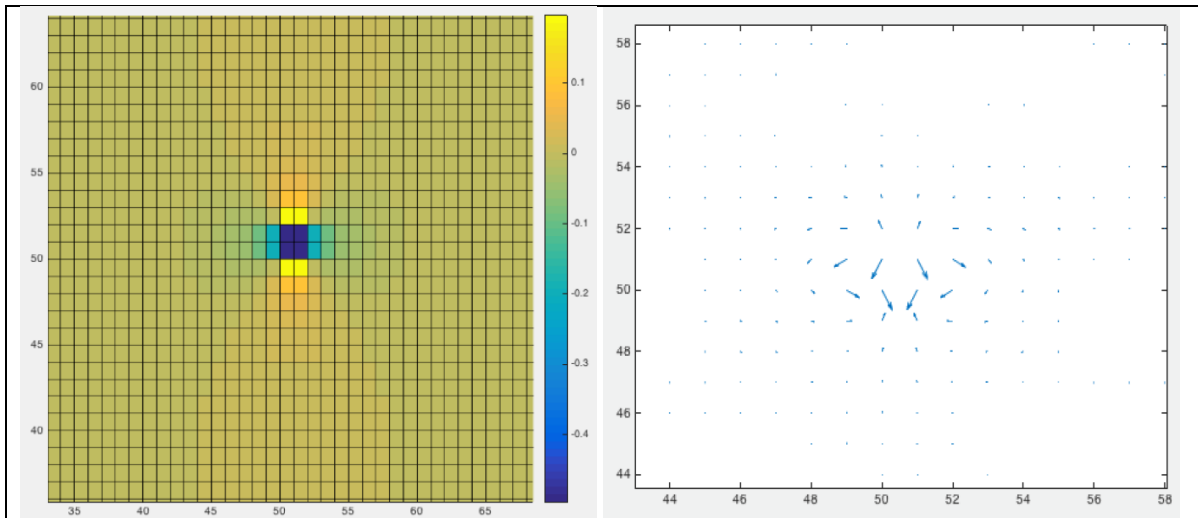


Figure 13. Intensity and vector plots of magnetic field ($\vec{B}$) of targeting magnet 1

**Targeting magnet 2 of strength 0.507 T**
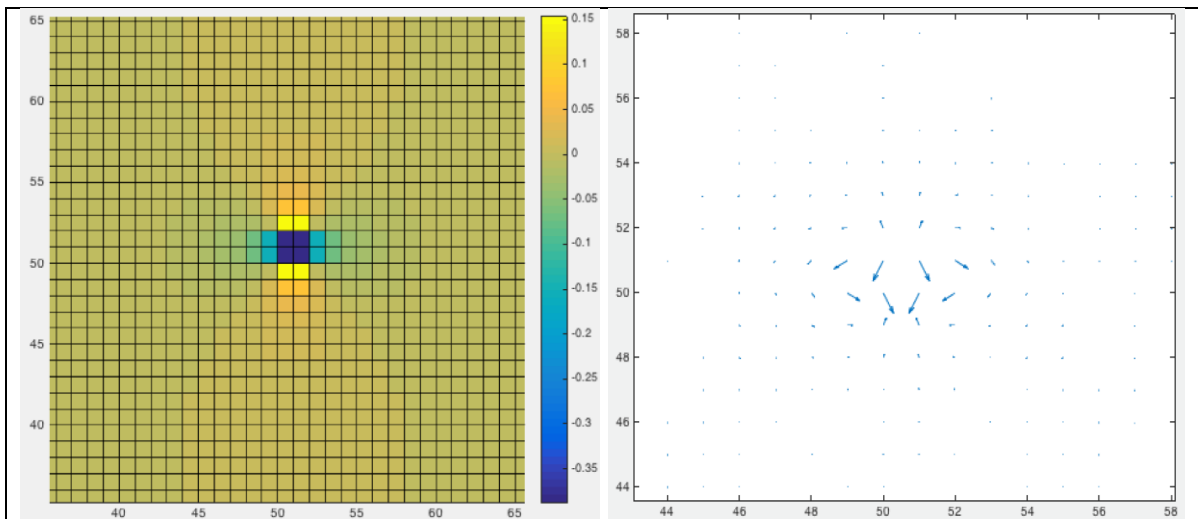


Figure 14. Intensity and vector plots of the magnetic field ($\vec{B}$) of targeting magnet 2

**Barrier magnet of strength 0.528 T**
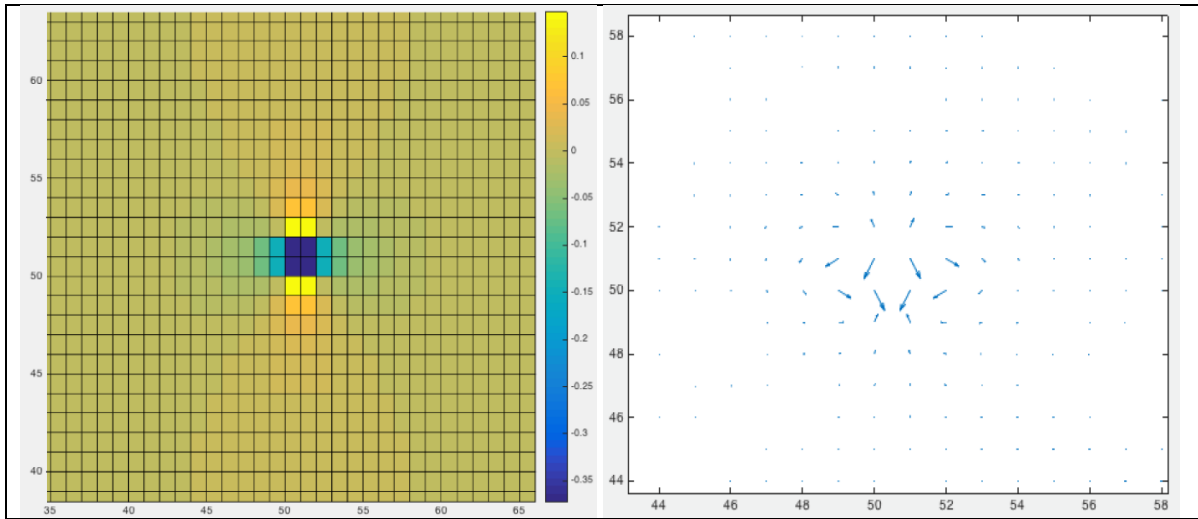


Figure 15. Intensity and vector plots of the magnetic field ($\vec{B}$) of barrier magnet

**ANSYS- fluent 3D simulations of the targeting and barrier magnets**

To verify the accuracy of our simulations, we determined value of the magnetic ($\vec{B}$) field 1cm above the magnets shown in Figure 18. The values obtained corresponded to the known $\vec{B}$ field values of the magnets.
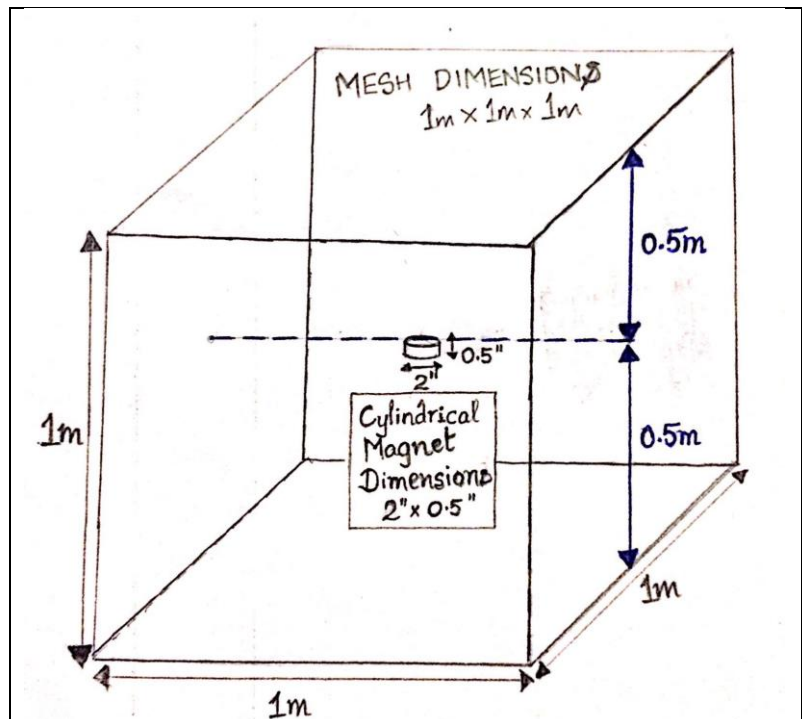


Figure 16: Figure showing mesh and magnet dimensions, along with the setup of the 3D problem in ANSYS fluent. The $\vec{B}$ field value was measured along the blue dashed line, which has been shown in Figure 18.
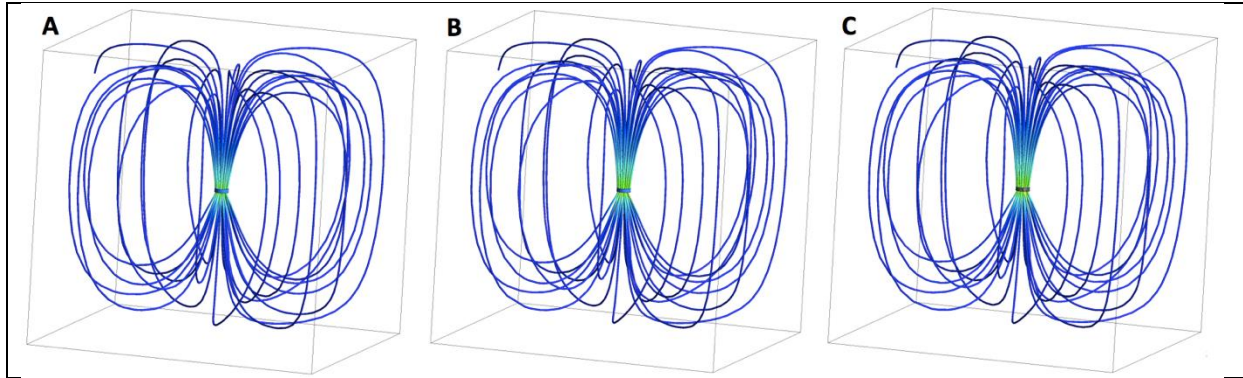
Figure 17. Magnetic field ($\vec{B}$) streamlines of targeting and barrier magnets. (A) 0.396 T targeting magnet (B) 0.507 T targeting magnet and (C) 0.528 T barrier magnet
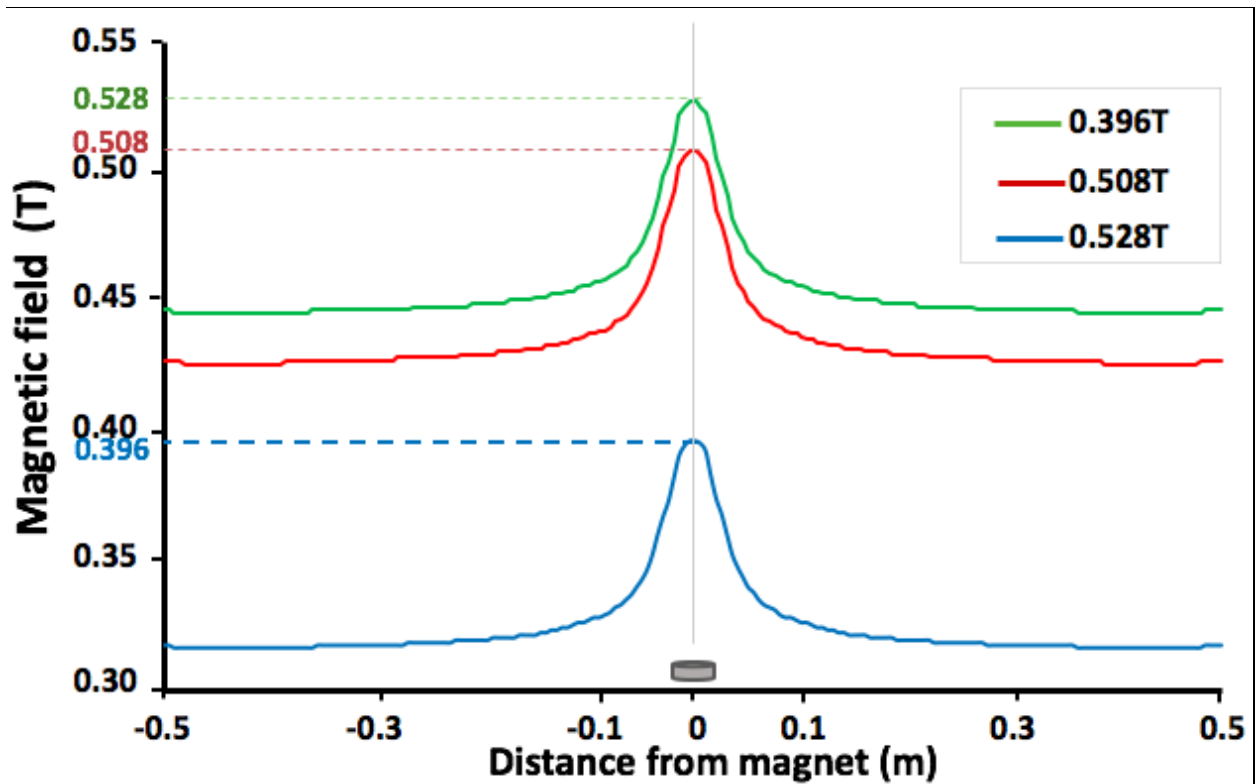


Figure 18. Plot of values of magnetic field ($\vec{B}$) at the surface of the 0.396T, 0.508T and 0.528T magnets along the blue dashed line in Figure 16. The graph clearly shows that the peak plot values correspond to the known field strength of the magnet.

Name of ANSYS fluent file in SHARE drive- *Magnet_1_V396_steady_sim.cas*
*Magnet_1_V508_steady_sim.cas*
*Magnet_1_V528_steady_sim.cas*

## 2.3. Determining force acting on a magnetic nanoparticle during magnetic drug targeting

### 2.3.1. Introduction

The effect of magnetic fields on transport of paramagnetic species has been investigated theoretically [62] and experimentally ([21], [42]). Many groups around the world have attempted to develop an accurate model for the force exerted by an external magnetic field, such as permanent magnet, on a magnetizable object, such as a magnetic nanoparticle. The most popular expressions for this force has been developed by Prof. Edward Furlani [63] and Prof. MEG Lyons [63], which have been used in several other publications (Sharma et. al, 2015 [64], Tran et al., 2011 [65], Uthra et al., 2015 [66] & Cregg et al., 2008 [67]). A list of the commonly-used expressions for this force, which we term $\vec{F}_{mag}$, has been enlisted in Table 3.

The flux of a population of paramagnetic species such as MNPs due to external magnetic body forces have been modeled using mainly two different approaches- (1) the magnetic forces are included as the external body forces in the Navier-Stokes equation and the resulting velocity is added to the convective term of the flux expression (Hinds et al., 2001 [68]; Uthra et al., 2015 [66]; Lunnoo et al., 2015 [69]; Waskaas and Kharkats, 1999, 2001 [70], [71]) and (2) the velocity of paramagnetic particles is approximated as a product of mobility and a net magnetic force, which is then included in the convective term of the flux expression (Furlani and Ng, 2006 [72]; Furlani and Xue, 2012 [73]).

| Reference | Expression for $\vec{F}_{mag}$ | Description |
|---|---|---|
| Furlani et al., 2006 | $\vec{F}mag = \mu_f (m_p.\vec{\nabla})\vec{H}_a$ <br><br> $m_p = V_p f(\vec{H}_a)\vec{H}_a$ <br><br> $f(\vec{H}_a) = \begin{cases} \dfrac{3(\chi_p - \chi_f)}{(\chi_p - \chi_f)+3} & \text{when } \vec{H}_a < \left(\dfrac{(\chi_p - \chi_f)+3}{3\chi_p}\right)M_{sp} \\ \dfrac{M_{sp}}{\vec{H}_a} & \text{when } \vec{H}_a \geq \left(\dfrac{(\chi_p - \chi_f)+3}{3\chi_p}\right)M_{sp} \end{cases}$ | • Most popular equation for $\vec{F}$mag by Edward Furlani <br> • Gives two possibilities for $\vec{F}$mag, depending on the strength of the applied magnetic field $(\vec{H}_a)$ <br> • Considers magnetizable nature of both MNPs as well as solution <br> • $\vec{F}$mag is included as the external body forces in the Navier-Stokes equation and the resulting velocity is added to the convective term of the flux expression |
| Sharma et al., 2015 [64] | $\vec{F}mag = \mu_o N_{mnp} V_{mnp} \dfrac{3\chi_{mnp}}{(\chi_{mnp}+3)}(\vec{H}_a.\vec{\nabla})\vec{H}_a$ | • $\vec{F}$mag equation like Furlani's equation for smaller applied magnetic fields <br> • Considers magnetizable nature of MNPs, not solution <br> • Accounts for force acting on larger number of MNPs by multiplying Furlani equation with total number of MNPs in the system |
| Lyons et al., 2001 [68] | $E_{mag} = -\dfrac{1}{2\mu_o}\chi_m c B^2/\mu_o$ <br><br> $\vec{F}mag = -\nabla E_{mag}$ <br><br> $\vec{F}mag = \dfrac{\chi_m \vec{B}^2 \nabla c}{2\mu_o} + \dfrac{\chi_m c \vec{B}\,\vec{\nabla}\vec{B}}{\mu_o}$ | • Lyons considers magnetizable nature of both MNPs as well as solution <br> • Can be used for a concentrated solution of MNPs <br> • Can be used for small and large external magnetic fields |
| Waskaas et al., 1999 [71] <br><br> Waskaas et al., 2001 [70] | $E_{mag} = \dfrac{1}{2\mu_o}(1+\kappa)H^2$ where, $\vec{B} = (1+\kappa)\mu_o\vec{H}$ <br><br> $\vec{F}mag = -\nabla E_{mag}$ <br><br> $\vec{F}mag = \dfrac{\vec{B}^2}{2\mu_o(1+\kappa)^2}\nabla\kappa$ | • Similar to approach in Lyons <br> • Can be used for small and large external magnetic fields <br> • Can be used for a single MNP problem |
| Pankhurst et al., 2003 [74] | $\vec{F}mag = \dfrac{V_p \Delta\chi}{\mu_o}(\vec{B}.\nabla)\vec{B}$ | • Pankurst considers only force on a single MNP <br> • Magnetizable nature of both MNPs as well as solution are considered <br> • Can be used for small and large external magnetic fields |

Table 3: Most commonly-used expressions for $\vec{F}$mag obtained from previous scientific literature search

### 2.3.2. MNP transport equations for intrathecal magnetic drug targeting developed by the Linninger Research Group

Combining these two popular approaches, the Linninger Research Group has developed a set of equations to quantify the force acting on a single MNP due to the presence of an external magnetic field, and to incorporate it into the Navier-Stokes equation for computational modeling of intrathecal magnetic drug targeting. Our approach is given below.

We represent the magnetic influence on the particles by using Newton's law:

$$m_p \frac{d\vec{v}}{dt} = \vec{F}_{mag} + \vec{F}_s \qquad (25)$$

The particle drag force exercised by the fluid in which the MNPs are dispersed, such as the blood or CSF in the human body, on a moving MNP is denoted by $\vec{F}_s$. MNP mass and velocity are indicated by the terms $m_p$ and $\vec{v}$ respectively. The magnetic force acting on a single MNP, $\vec{F}_{mag}$, can be computed as a function of the external magnetic flux density, $\vec{B}$, by using the equation from Pankhurst et al., 2003 [74]:

$$\vec{F}_{mag} = \frac{V_p \left( \chi_p - \chi_{medium} \right) \vec{B} \cdot \vec{\nabla} \vec{B}}{\mu_o} \qquad (26)$$

In equation (26), $V_p$ is the volume of the MNP and $\vec{B}$ is the magnetic flux density generated by an external magnet. The magnetic susceptibilities of MNPs and the medium are given by $\chi_p$ and $\chi_{medium}$, respectively. To predict MNP localization due to a magnet, we propose a modified particle velocity term $\vec{v_p}$, which accounts for the velocities due to both the natural CSF pulsations, $\vec{u}_{CSF}$, as well as magnetic forces, $\vec{u}_m$. The modified particle

velocity accounting for the combined effects of magnetic and CSF induced motion enters the convection–diffusion equation in eq (28).

$$\vec{v_p} = \vec{u}_{CSF} + \vec{u}_m = \vec{u}_{CSF} + \frac{\vec{F_m}}{6\pi\eta r_p} \qquad (27)$$

Solution of eq (28) together with the Navier Stokes equation, allows predicting distribution and localization of MNPs in any suspension under magnetic guidance. If the MNPs are loaded with drug molecules, suitably adjusted equations can determine drug localization, release and transfer into the tissues of the human body [75].

$$\frac{\partial c}{\partial t} + \vec{\nabla} \cdot \left(\vec{v_p}\, C\right) = \vec{\nabla} \cdot \left(D\, \vec{\nabla} C\right) \qquad (28)$$

During intrathecal magnetic drug targeting experiments, we apply an external magnet over the thoracic region of the spine. To understand the influence of such a magnet on MNPs within the intrathecal space, we calculate values of $\vec{u}_m$ along the length of the spine (Figure 19B) and compared it to values of $\vec{u}_{CSF}$ at various regions along the human spine (Figure 19A). The $\vec{u}_{CSF}$ values have already been previously computed in the Linninger lab ([76][75]).

Figure 19. Comparison of $\vec{u}_{CSF}$ and $\vec{u}_m$ values acting on a single MNP within the intrathecal space (A) Values of $\vec{u}_{CSF}$ and $\vec{u}_m$ at various levels along the spine. $\vec{u}_m$ values are the highest close to the magnet, and decrease exponentially in either direction away from the magnet. (B) Plot of $\vec{u}_m$ values along the whole length of the spine.
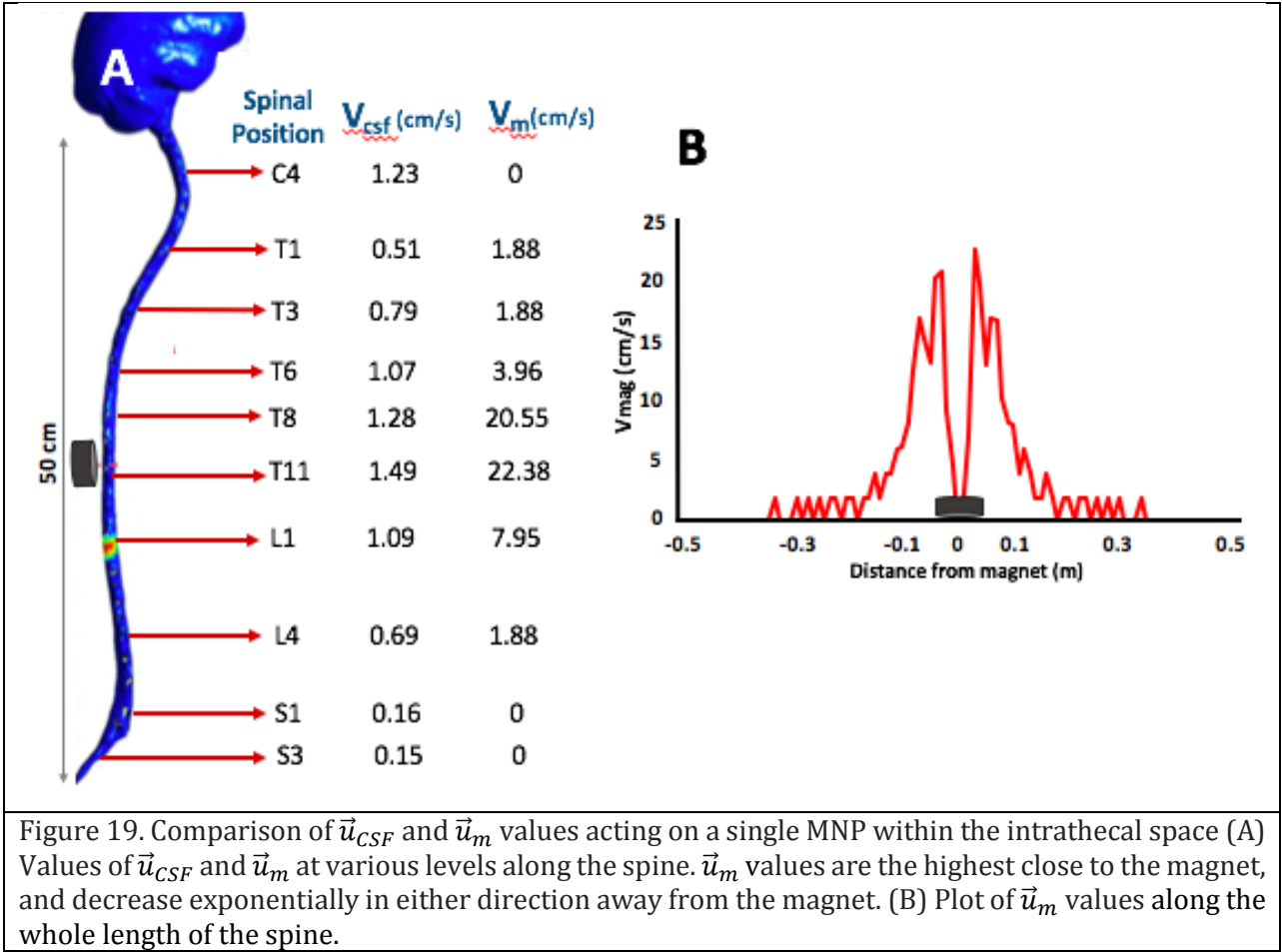
### 2.3.3. MNP flux equations for intrathecal magnetic drug targeting for concentrated MNP solutions

Currently, all approaches to determine the flux of MNPs due to external magnetic body forces, suffer from some common limitations: (1) They can only be applied for dilute MNP suspensions and (2) They do not account for paramagnetic interaction, also called magnetic dipole interaction, between MNPs. An accurate set of equations for modeling $\vec{F}_{mag}$ and its subsequent incorporation into the Navier-Stokes equation for predicting MNP distribution and localization should consider the following factors:

- It should be valid for both dilute and concentrated MNP solutions.

- It should take the magnetic properties of both MNPs and suspension solution/electrolyte into consideration.

- It should account for paramagnetic interaction between MNPs, which leads to agglomeration. This is a commonly observed in MNP-based experimental work.

- It should account for effects of both magnetic field gradients as well as Lorentz force.

To accurately model magnetic drug targeting, considering all the above-mentioned factors, Prof. Maneesh Singh and Prof. Andreas Linninger have developed the following theory for flux of paramagnetic species:

In the presence of an applied magnetic field, MNPs experience three kinds of body forces:

(a) Paramagnetic gradient force due to concentration gradient

(b) Magnetic field gradient force due to external magnetic field gradient

(c) Lorentz force due to interaction of moving MNPs with the external magnetic field

Theory of Magnetic Particle Transport

Consider a solution of charged paramagnetic nanoparticles exposed to a magnetic field. The energy density of the solution in the presence of a magnetic field is:

$$E_{mag} = \vec{\mathbf{M}} \cdot \vec{\mathbf{B}}/2 = -\chi_m\, c\, \vec{\mathbf{B}} \cdot \vec{\mathbf{B}}/2\mu_0 \tag{29}$$

where $\vec{\mathbf{M}}$ is the magnetization induced by the magnetic field $\vec{\mathbf{B}}$. $\mu_0$ is the magnetic permeability of vacuum, $\chi_m$ is the molar susceptibility, and $c$ is the concentration of paramagnetic species. The magnetic force, obtained from the gradient of energy density, can be expressed as follows

$$\vec{\mathbf{F}}_{mag} = -\vec{\nabla}E_{mag} = \frac{\chi_m(\vec{\mathbf{B}} \cdot \vec{\mathbf{B}})}{2\mu_0}\vec{\nabla}c + \frac{\chi_m c}{\mu_0}\left(\vec{\nabla}\,\vec{\mathbf{B}}\right) \cdot \vec{\mathbf{B}} \tag{30}$$

The first term is the paramagnetic gradient force, $\vec{\mathbf{F}}_P$, due the variation in paramagnetic susceptibility in the diffusion layer and the second term is the field gradient force, $\vec{\mathbf{F}}_B$, due to the field gradient in the solution. $\vec{\mathbf{F}}_{mag}$ can be included as external body force in the Navier-Stokes equation, whose solution provides the velocity field corresponding to the magnetohydrodynamics (MHD) effect. The relative contribution from the magnetic forces in the Navier-Stokes equation is negligible for a dilute solution of paramagnetic nanoparticles. The MHD effect is also coupled with the mass transport equations for the paramagnetic particles. Generalized flux expressions can be obtained from the conservation of momentum between the paramagnetic particles and the solution. The primary forces acting on the paramagnetic particles are:

i)    Force due to gradient of electrochemical potential, $-\vec{\nabla}\mu_i = -RT\vec{\nabla}\ln(\gamma_i c_i) - z_i F\vec{\nabla}\phi$, where $\gamma_i$ is the activity coefficient which depends on the specific interaction between magnetized particles, $\phi$ is the electric potential, $z_i$ is the charge number and $F$ is the Faraday's constant

ii)    Paramagnetic gradient force $\vec{\mathbf{F}}_P$

iii)    Magnetic field gradient force $\vec{\mathbf{F}}_B$,

iv)    Lorentz force $\vec{\mathbf{F}}_L = z_i\vec{\mathbf{v}}_i \times \vec{\mathbf{B}}$

The force balance in eq (31) specifies that the sum of driving forces acting on a species is balanced by drag forces due to interactions with other species (Newman and Thomas-Alyea, 2012).

$$c_i\vec{\nabla}\mu_i - \frac{\chi_m(\vec{\mathbf{B}}\cdot\vec{\mathbb{Z}})}{2\mu_0}\vec{\nabla}c_i - \frac{\chi_m c_i}{\mu_0}(\vec{\nabla}\,\vec{\mathbf{B}})\cdot\vec{\mathbf{B}} - c_i z_i\vec{\mathbf{v}}_i \times \vec{\mathbf{B}} = \sum_j \frac{RTc_ic_j}{c_T D_{i,j}}(\vec{\mathbf{v}}_j - \vec{\mathbf{v}}_i) \qquad (31)$$

Here $\vec{v_i}$ is the average velocity of ith species, $D_{i,j}$ is the binary diffusion coefficient and $c_T$ is the total concentration of all species. The expression for flux of paramagnetic particles can be derived from eq (2) using an average diffusion coefficient $D_{e,i}$ and average velocity $\vec{v}_{e,i}$

$$\vec{N_i} = -D_{e,i}\left(\vec{\nabla}c_i - c_i\vec{\nabla}\ln\gamma_i - \frac{z_iFc_i}{RT}\vec{\nabla}\phi - \frac{\chi_m(\mathbf{B\cdot B})}{2RT\mu_0}\vec{\nabla}c_i - \frac{\chi_m c_i}{RT\mu_0}(\nabla\,\mathbf{B})\cdot\mathbf{B} - \frac{z_i\vec{N_i}\times\vec{B}}{RT}\right) + c_i\vec{v}_{e,i} \qquad (32)$$

The flux-expression eq (32) gives an implicit relationship that can describe the flux of a concentrated solution of interacting MNPs. The inter-particle interaction can be modeled using a suitable activity coefficient. If the electrical potential gradient $\vec{\nabla}\phi$ is negligible and that the MNP activity does not significantly depart from unity, we can simplify eq (32) for a monodisperse MNP suspension.

$$\vec{N} = \underbrace{-D\vec{\nabla}c}_{\text{Diffusion}} + \underbrace{\frac{D\chi_m(\mathbf{B\cdot B})}{2RT\mu_0}\vec{\nabla}c}_{\text{Magnetic diffusion}} + \underbrace{\frac{D\chi_m c}{RT\mu_0}(\nabla\,\mathbf{B})\cdot\mathbf{B}}_{\text{Magnetic convection}} + \underbrace{\frac{\square\,z\,\vec{N}\times\vec{B}}{RT}}_{\text{Electromagnetic convection}} +$$

$$\underbrace{c\,\vec{v}}_{\text{Convection}} \qquad\qquad\qquad\qquad (33)$$

The flux expression (33) can be written using the magnetic diffusion coefficient $D_m = D\chi_m\vec{B}\cdot\vec{B}/2RT\mu_0$ and magnetic velocity $\vec{v}_m = D\chi_{\square}(\nabla\,\mathbf{B})\cdot\vec{B}/RT\mu_0$ as:

$$\vec{N} = -(D - D_m)\vec{\nabla}c + c\,(\vec{v}_m + \vec{v}) + z\,u\,\vec{N}\times\vec{B} \qquad (34)$$

The conservation of mass requires:

$$\frac{\partial c}{\partial t} + \vec{\nabla}\cdot\vec{N} = 0 \qquad (35)$$

Eqs (34) and (35) can be solved to obtain biodistribution of MNPs suspended in pulsatile CSF. Our formulation is also valid for dense particle agglomeration close to the collection magnet. Additional expressions may be added to eq (35) as needed to account for reaction kinetics of nanoparticle uptake, enzymatic destruction, or dissociation of conjugated therapeutics.

## 3. QUANTUM DOT CONJUGATED MAGNETIC NANOPARTICLES FOR TARGETED DRUG DELIVERY AND IMAGING

(Previously published as Venugopal, I., Pernal, S., Fusinatto, T., Ashkenaz, D., and Linninger, A. (2016) Quantum Dot Conjugated Magnetic Nanoparticles for Targeted Drug Delivery and Imaging, Nano Biomedicine & Engineering 8, no 1)

### 3.1. Summary

In this chapter, a new fluorescent MNP delivery vehicle for MDT & IT-MDT has been described. MNPs act as contrast agents for MRI. However, it cannot be visualized via this technique during drug delivery due to interference between magnetic fields used for MRI imaging and delivery. The Linninger Research Group has synthesized a drug delivery MNP vehicle conjugated with quantum dots that can be imaged during the IT-MDT process with *in vivo* imaging techniques such as fluorescence molecular tomography. These quantum dot loaded MNPs, also referred to as nanocomposites in this dissertation, can be used as drug delivery vehicles for the CNS. In addition, these nanocomposites were also used to prove the feasibility of the IT-MDT technique, by localizing the fluorescent nanocomposites at a specific site along the spine, which could be clearly visualized using fluorescence molecular tomography.

### 3.2. Introduction

Drug delivery to specific organs or tissues, especially to the CNS, poses significant challenges such as achieving high efficacy while evading side effects ([77], [78]). Currently, the lack of specificity towards the target site generates the need for using high drug dosages to attain required therapeutic effect. However, this elevates the risk of toxicity in non-targeted regions, leading to unwanted side effects. For example, high doses of chemotherapeutic drugs are known to cause unacceptable systemic toxicity ([79]–[82]).

The small size of the nanoparticles allows them to circumvent some of the most impenetrable barriers of the human body. As mentioned in the previous chapters, the BBB which is formed by a continuous layer of endothelial cells joined together by tight junctions surrounding blood vessels ([83], [84]), severely restricts access of large therapeutic molecules to the brain and spinal cord tissue. Previously, nanoparticles have been utilized to by-pass the BBB for treatment of CNS diseases like gliomas ([85]–[87]). Nanoparticle based drug delivery systems also offer other benefits such as increased drug bioavailability ([88]–[90]), higher stability for treatments involving controlled release of drugs ([91]–[93]), effective delivery of poorly water soluble drugs and co-delivery of two or more agents rendering multi-functionality ([94]–[96]).

MNPs have drawn interest for their intrinsic magnetic property, which is advantageous for targeted drug delivery and biomedical imaging. MNPs lesser than 30 nm in diameter are *superparamagnetic*; a property that enables them to get temporarily magnetized in presence of a magnetic field and lose all magnetization once the field is removed. This property prevents unwanted agglomeration which is important for targeted delivery [97]. MNPs are also used as a contrast agent for MRI due to its ability to reduce the T2 relaxation time of water molecules([98], [99]). Several research groups have developed MNPs for exploiting their properties as MRI contrast agents ([100]–[104]). Despite these achievements, imaging MNPs via MRI during MDT or IT-MDT remains difficult, because the magnetic fields used to generate images interfere with the magnetic fields needed for MDT. Therefore, there is a need for an MDT delivery vehicle that can be imaged in real time *in vivo* without resorting to MRI. This vehicle was also used to prove the feasibility of IT-MDT *in vivo*.

In this chapter, we present a nanovehicle that can be specifically targeted via MDT and have its distribution tracked during *in vivo* delivery. This vehicle comprises of a gold-coated magnetite ($Fe_3O_4$@Au) nanoparticle conjugated to cadmium telluride quantum dots (CdTe QDs). It offers three major benefits:

(i)   The vehicle can be targeted, localized and concentrated at specific sites within tissues or organs; magnetite ($Fe_3O_4$) core of these nanoparticles allows steering under the influence of externally placed magnets.

(ii)  The outer gold shell of the vehicle can be loaded with therapeutic molecules. Drugs that have sulfur-containing functional groups show a strong affinity to bind to gold surfaces [105], [106], which enables conjugation of many active agents with relative ease.

(iii) The cadmium telluride quantum dots (CdTe QDs) can be imaged *in vivo* during delivery due to strong fluorescence emission.

Commercially available imaging modalities utilizing fluorescence molecular tomography (FMT) can image this nanocomposite *in vivo*, due to the strong fluorescence emission by the quantum dots (QDs). QDs are nanometer sized highly fluorescent particles made of semiconductor materials, which do not photobleach easily. QDs retain strong fluorescence even after conjugation to the MNPs, when compared to organic molecules such as rhodamine and fluorescein ([107], [108]). QDs also have broader excitation spectra (high absorption) and a narrow, sharp emission peak [109, p. 1], which results in a brighter emission and a higher signal to noise ratio.

This chapter presents the synthesis and characterization details of a novel QD-MNP drug delivery vehicle, which was also used for proving the feasibility (localization and

targeting capability) of IT-MDT *in vivo* within a Sprague Dawley rat. Details of the experimental procedures and results are provided in the following sections.

## 3.3.    Materials and Methods

The synthesis method of each of the individual components –gold coated magnetite nanoparticles ($Fe_3O_4$@Au MNPs), cadmium telluride quantum dots, and conjugation into a single nanocomposite has been described separately.

This section starts with a detailed description for the synthesis of the magnetic nanocomposites. Then cell-based experiments for proving biocompatibility and applicability of the nanocomposites in the CNS are described. An *in vivo* imaging experiment illustrates imaging ability of the vehicle. Finally, an MDT and IT-MDT experiment demonstrated the magnetic targeting capability of our nanocomposites. These experiments were used to prove the feasibility of the IT-MDT technique to localize MNPs within the intrathecal space of a Sprague Dawley rat.

### 3.3.1.  Synthesis of Gold-Coated Magnetite Nanoparticles

The $Fe_3O_4$ cores were synthesized by a coprecipitation technique, well described by Mandal [110], and various other articles, using ferrous and ferric salts to form $Fe_3O_4$ ([111]–[113]). This has also been described in our previous published papers, as well as in the *in vitro* work described in the Appendix Section A.

### 3.3.2.  Synthesis of CdTe Quantum Dots

The microwave based synthesis procedure was similar to Duan's paper [114] with modifications made to the microwaving procedure. The procedure yielded QDs in the 2-6 nm size range.   Briefly, cadmium chloride stock solution was prepared as follows - 0.4 mL of 0.04 M of cadmium chloride solution was diluted with 42 mL of water to produce the

stock solution. The Cd-MPA-Te solution was prepared as follows - 100 mg of trisodium citrate dihydrate, 4 mL of 0.01 M sodium tellurite solution, 119 mg of 3-mercaptopropionic acid and 50 mg of sodium borohydride were added to the cadmium chloride stock solution under magnetic stirring. The molar ratio of Cd:MPA:Te in the solution was 1:7:0.25. The pH of the solution was maintained at 8. The synthesis of the QDs by using microwaving technique was performed as follows - 10 mL of the solution was placed in a 60 mL teflon digestion vessel (Savillex corporation, MN, USA). The QDs were synthesized with varying temperatures and microwaving time durations (89 ℃-130 ℃ and 1-5 min) to produce QDs of different colors. The power of the microwave device (Samsung, 1.05 Kw Micro Wave) was set at 900W. The QD samples were cooled to room temperature prior to further examination.

### 3.3.3. Synthesis of quantum dot conjugated gold coated magnetite nanocomposites (QD-$Fe_3O_4$@Au MNPs)

1 mL of both the $Fe_3O_4$@Au MNPs and CdTe QD solutions (0.17 mg/mL) was added to 20 mL of ethanol in a glass container. The glass container was kept in the dark for 48 hours under constant slow stirring. This allowed for conjugation of the QDs to the gold coating of the $Fe_3O_4$@Au MNPs to form the fluorescent nanocomposites.  The excess ethanol was removed by magnetic decantation. The solution was washed with water to remove the free-floating water soluble QDs, followed by magnetic decantation to separate the nanocomposites. This process was repeated several times to remove all the free QDs from the solution, which can be confirmed by absence of fluorescence emission from the supernatant obtained from magnetic decantation. The washed nanocomposites are resuspended in pure water to obtain the desired concentration.

### 3.3.4.  Cell transfection experiment using C6 glioma cells

To produce a cytotoxic effect in diseased target cells, nanocomposites need to be internalized. Therefore, the uptake of fluorescent nanocomposites into rat tumor cells (C6 glioma cells) was studied in a transfection experiment. Cells were maintained in medium containing Dubelcco's Modified Eagle Medium and 10% fetal bovine serum with 1% antibiotics. Various concentrations of the nanocomposites were prepared using the cell growth medium as diluent. 1mL of this nanocomposite solution was applied to cells cultured in a 12-well plate. After incubation for 5 hours, cells were fixed with a 4% paraformaldehyde solution, while protecting it from light exposure to avoid unwanted loss of fluorescence. Phalloidin-CruzFlour488 conjugate (Santa Cruz Biotechnology, 1:1000 solution in phosphate buffer solution (PBS)) was applied onto the fixed sample for 60 min to stain the cells' actin cytoskeleton. After rinsing phalloidin completely, DAPI (Biotium, 1:4000 solution in PBS) was applied for 5 min to stain chromatin in the nuclei of the cells. Cells were imaged using a normal Zeiss Axioskope fluorescence microscope.

The cellular uptake of the nanocomposites was quantified using *Image J* software[115]. The quantification was performed by compiling three fluorescence images corresponding to the DAPI, nanocomposite and phalliodin stains (Figure 25 A1,A2,A3). Phalloidin stains the actin cytoskeleton, marking the cell boundaries, and appears green; DAPI stains the nucleus, assisting in cell counting, and appears blue; and the nanocomposites appear red due to the QDs. Using the compiled image, only the portion of the image containing cells is selected, and *Image J* was used to quantify the average amount of red intensity per pixel. The average red intensity per pixel in the background of the

45

composite image is subtracted from the average within the cell boundary.  This final value

provides a relative estimate of the nanocomposite uptake.

### 3.3.5. Delivery of the nanocomposites into the intrathecal space of a rat

12-week old Sprague Dawley rats were used for this procedure. All animal

experiments were approved by the Animal Care and Use Committee at UIC. The animals

were anesthetized by inhalation of isoflurane. The surgical table was equipped with

stereotaxis equipment and a nose cone to allow for administration of gaseous isoflurane

during surgery. Once anesthetized, the hair on the back of the animal was shaved using hair

trimmers. This allowed for obtain better signal acquisition during the FMT procedure. An

L3 laminectomy was performed and the bone was thinned down till it could be penetrated

using a 30G needle. A small volume of 0.17 mg/mL nanocomposite solution was injected

into the spinal SAS using a syringe pump.  The imaging procedure described below was

performed, after which rats were euthanized.

### 3.3.6. *In vivo* imaging procedure

FMT was performed using a Xenogen (Caliper Life Sciences) IVIS System equipped

with anesthetic isoflurane system. The nanocomposites have an excitation wavelength of

550 nm and emission wavelength filter was set to 590 nm. Other settings used for image

acquisition were: binning level = medium, fvalue = f/2 and acquisition time = 10 seconds.

### 3.3.7. Intrathecal magnetic drug targeting procedure

To test the magnetic targeting capability of the nanocomposites, we developed a

simple *in vitro* infusion system, in which amplitude and frequency of fluid pulsations can

easily be adjusted. The model, as shown in Figure 27, consists of a cylindrical polystyrene

tube (49.0 cm length; 0.75 cm inner diameter) which encloses the fluid, which could be

artificial CSF or water. A latex deformable membrane was tightly fixed to the mouth of the distal neck which expands and contracts to permit pulsatile motion of the fluid.

Nanoparticle distribution inside the fluid varies depending on different patient specific parameters such as the frequency and magnitude of the pulsations, the velocity and stroke volume of fluid, and heart rate. In our lab, we are interested in the intrathecal delivery of the nanocomposites for treatment of CNS diseases. We therefore, imposed a fluid velocity of 1.5 cm/s and a stroke volume of 2 mL, which are within the average ranges for CSF movement, as cited in prior literature ([116], [117]). Initially, we used water as the fluid in our system, because it has similar density to CSF [118].

To produce pulsatile fluid motion equal in amplitude and frequency to that of a typical resting human's CSF pulsations, the proximal end of the model was connected to a masterflex peristaltic pump and two of the three metal cylinders that drive the pump were removed to create a ramping pulse function. Since CSF pulsates at a frequency of the heart beats, the pump was set at 70 bpm which, according to the American Heart Association, is within the 60-80 bpm range of normal resting heart rate in humans.

A predetermined volume of the nanocomposite solution (0.17 g/mL) was injected into the model. A targeting magnet of 35 lb pull force strength was placed at a distance of 10 cm from the injection site to collect the injected nanocomposites. This region represents the targeting region. The experiment lasted for 10 min during which the accumulation at the target magnet site was imaged. No observable increase in the CE of nanocomposites at the targeting magnet site was observed beyond 10 min.

## 3.4. Results

### 3.4.1. Synthesis and Characterization results

Gold-Coated Magnetite Nanoparticles: The $Fe_3O_4$@Au MNPs were characterized using TEM, EDS, selected area electron diffraction (SAED) and SQUID magnetometry (Figure 43,12). The $Fe_3O_4$@Au MNPs used in our experiments had a $Fe_3O_4$ core with diameter between 8-12 nm with a uniform gold shell thickness of 12 nm, making the total diameter of the particle to be around 20-25 nm. $Fe_3O_4$ cores of this size exhibit superparamagnetic property retaining no net magnetization when removed from an external magnetic field [119]. They can be dispersed without agglomeration until an external magnetic field attracts the MNPs, allowing for magnetic guidance and localization at the target site.

The gold coating on the $Fe_3O_4$ core serves two purposes: (i) It prevents the oxidation of the $Fe_3O_4$ core into maghemite ($Fe_2O_3$) by forming a protective coating layer. $Fe_2O_3$ has weaker magnetic susceptibility than $Fe_3O_4$ ([120], [121]) (ii) It also forms a convenient platform for loading drugs to the MNP surface, since gold has a natural affinity for sulfur-containing functional groups and thiol bonds.
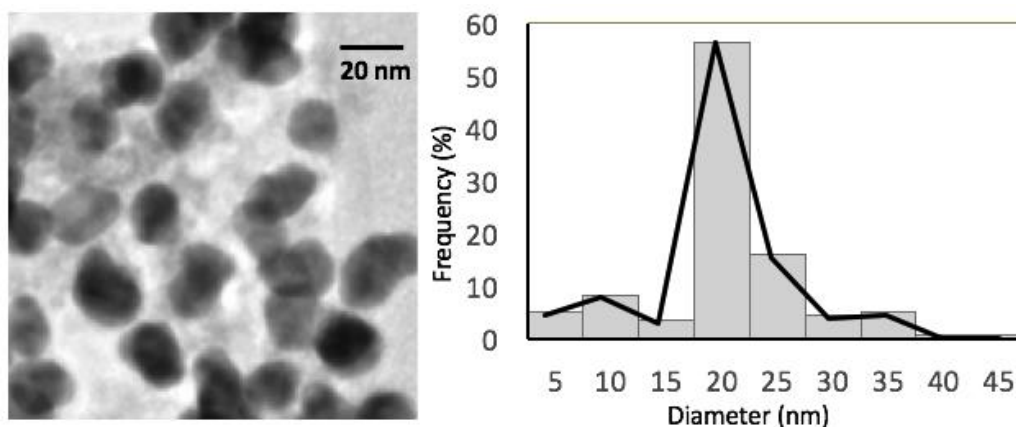


Figure 20. TEM image showing multiple $Fe_3O_4$@Au MNPs along with a histogram of their size distribution

EDS was used to confirm the chemical composition of the nanoparticles (Figure 43D). The spectra obtained indicated the presence of the elements gold (Au) and iron (Fe). The SAED patterns shown in Figure 21 A, B of the $Fe_3O_4$ cores and $Fe_3O_4$@Au MNPs indicate ring patterns confirming the face centered cubic structure of both $Fe_3O_4$ and Au respectively. In Figure 21A, the spacings measured in the diffraction patterns of 0.30 nm, 0.265 nm, 0.218 nm and 0.150 nm agree with the following standard reflections for $Fe_3O_4$: 0.297 nm (220); 0.253 (311); 0.210 nm (400); 0.148 nm (440). From the diffraction pattern shown in Figure 21B, the d-spacing is 0.236 nm. This is close to the closed packed Au (111) spacing of 0.2355 nm. These diffraction patterns confirm the $Fe_3O_4$ core and Au surface of our MNPs. The magnetic properties of these MNPs has also been described in detail elsewhere (section 2.4.1).
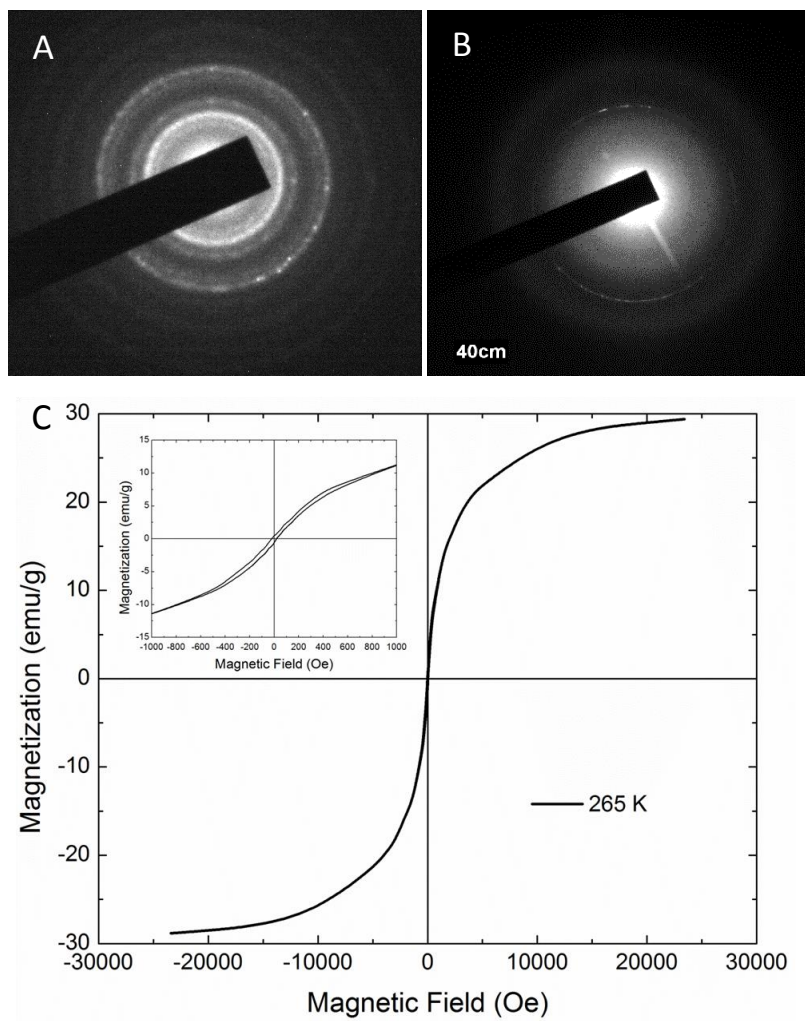


Figure 21. Characterization of $Fe_3O_4$@Au MNPs (A) SAED pattern of the $Fe_3O_4$ core (B) SAED pattern of the $Fe_3O_4$@Au MNPs (C) M-H loop (magnetization versus applied magnetic field) obtained by SQUID magnetometry at 265 K.

CdTe Quantum Dots: A microwave irradiation procedure produced fluorescent, stable, water soluble CdTe QDs. Red QDs (2-3 nm) were synthesized using the procedure described in the methods section. QDs of varying colors can by synthesized by this technique. The colors arise from the quantum confinement effect since different QD radii produce different emission wavelengths ([109], [122], [123]). Size tunability was observed and confirmed through TEM analysis (Figure 22 A,B).
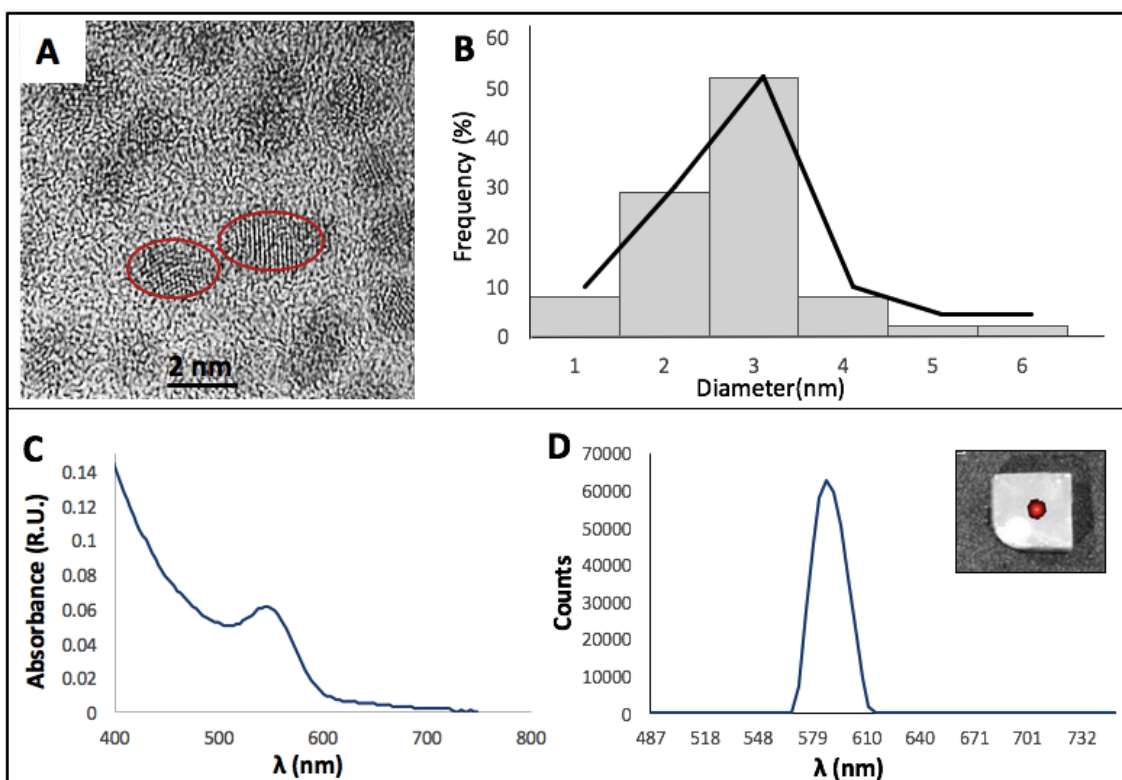


Figure 22. Characterization of CdTe QDs (A) TEM image of red QDs measuring about 2-3 nm. Some of the QDs have been circled for better visibility (B) Histogram showing the size distribution of the red QDs (C) Absorption spectra of the CdTe QDs with a peak at 550 nm (D) Emission spectra of the CdTe QDs showing a peak at 590 nm. An inset has been included which shows FMT image of QDs injected into a 6% agarose gel.

Fluorescence emission of the red QDs was confirmed using a fluorescence spectroscopy (NanoDrop 3300 fluorimeter). The absorption and fluorescence emission spectra of the QDs, shown in Figure 22 C,D indicate that the QDs have absorption and

emission maxima peaks at 550 nm and 590 nm respectively. Red CdTe QDs were chosen for

the synthesis of the nanocomposites because they have an emission peak of 590 nm, which

is better-suited for *in vivo* imaging.

QD-Fe$_3$O$_4$@Au fluorescent nanocomposites: The nanocomposites had a total

diameter of around 30-45 nm, which consisted of a Fe$_3$O$_4$@Au nanoparticle core

conjugated to QDs on its surface (Figure 23A). These nanocomposites are

superparamagnetic, because the

Fe$_3$O$_4$@Au nanoparticle s that

form the core are

superparamagnetic. This

property prevents

agglomeration during delivery.

The stability of QDs after

loading on the surface of the

nanocomposites was studied

with fluorescence and UV-Vis

spectroscopy. When red QDs

were loaded onto the MNP

surface, the nanocomposites

showed similar absorption and

emission peaks as the plain



Figure 23. Characterization of QD-Fe$_3$O$_4$@Au nanocomposites (A) Schematic of QD-Fe$_3$O$_4$@Au nanocomposite (B) TEM image of the nanocomposite that shows both the nanocomposite core (white circle) as well as the conjugated QDs (smaller pink circles) (C) Enlarged view of the nanocomposite surface showing the individual QDs (pink circles) (D) FMT images of the QD-Fe$_3$O$_4$@Au nanocomposites injected in a 6% agarose gel (E) Normal and FMT images of the nanocomposite solution

red CdTe QDs, with the emission peak at 590 nm. No change in the fluorescence spectral

profile of the QD-Fe$_3$O$_4$@Au nanocomposites was observed when compared to the plain

QDs (Figure 16A). FMT was also used to confirm the fluorescence emission of the conjugated structure in several environments, as shown in Table 4 and Figure 23D,E.

To determine the fluorescence emission stability of the nanocomposites over an extended period, the nanocomposite solution was kept in the dark at room temperature and small samples were withdrawn at regular intervals to examine the fluorescence emission. A negligible loss of fluorescence was observed over a period of three weeks. After that time, fluorescence decayed exponentially (Figure 24B), due to gradual oxidation of the CdTe QDs. Complete loss of fluorescence was observed after two months.
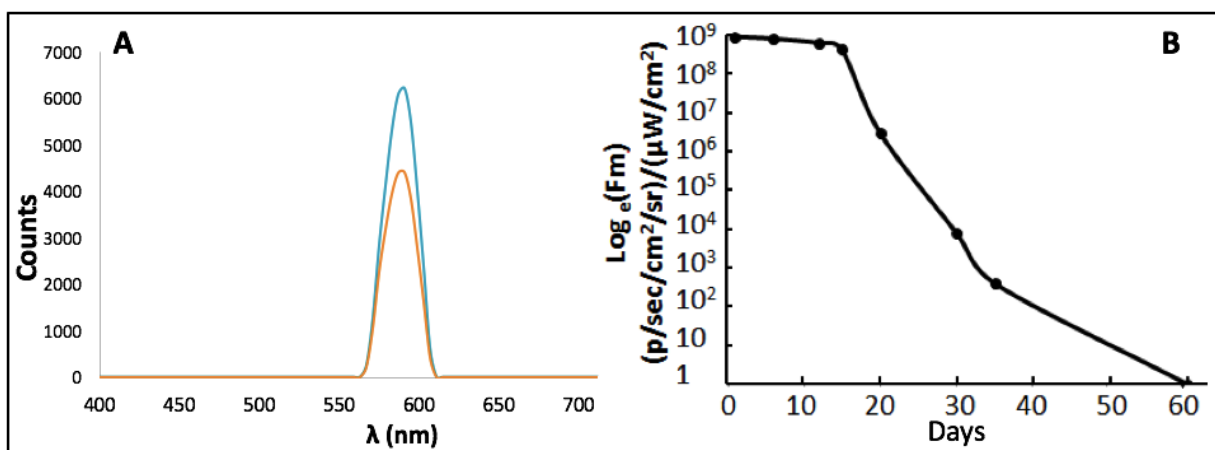


Figure 24. Fluorescence characterization of QD-Fe$_3$O$_4$@Au nanocomposites (A) Emission spectra of the QD-Fe$_3$O$_4$@Au nanocomposites (orange) and plain CdTe QDs (blue). Maximum emission wavelengths for both were determined to be 590 nm (B) Graph showing the loss of fluorescence of the QD-Fe$_3$O$_4$@Au nanocomposites over time.

### 3.4.2. Cellular Uptake Experiment

Confocal microscopy images (Figure 25B) indicate the presence of the QD-Fe$_3$O$_4$@Au nanocomposites inside a C6 glioma cell. Insets B1 and B2 show z-stack images (x-z and y-z respectively) of the cell confirming the presence of the nanocomposites inside

it. Figure 25A shows fluorescence images of the nanocomposites transfected into rat astrocyte cells.
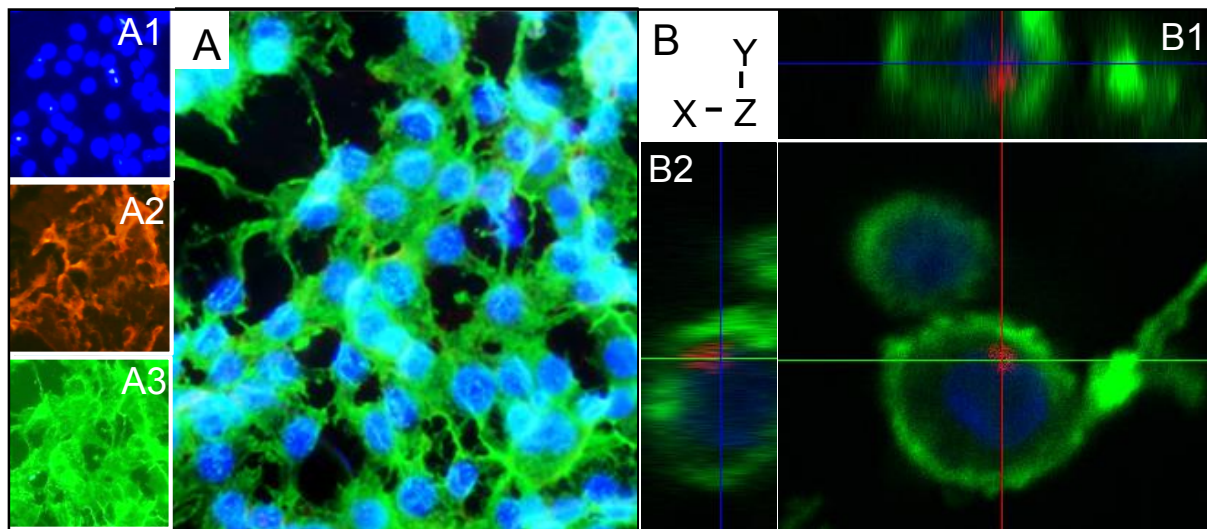


Figure 25. Fluorescence microscopy results showing uptake by rat cortical astrocytes and C6 glioma cells on incubation in a 0.034 mg/mL nanocomposite solution for 30 min. All cells have been stained labeled using DAPI, which stains the nucleus blue, and phalloidin, which stains the actin cytoskeleton green. The nanocomposites appear red corresponding to the emission wavelength of 590 nm. (A) Image showing nanocomposite localization within rat astrocyte cells. Insets contain images of separate stains: DAPI, QD-$Fe_3O_4$@Au MNPs and phalloidin (B) Confocal microscopy images of QD-$Fe_3O_4$@Au MNPs transfected into C6 glioma cells. Insets B1 and B2 show the z-stack images (x-z and y-z) indicating the presence of nanocomposites inside the cell.
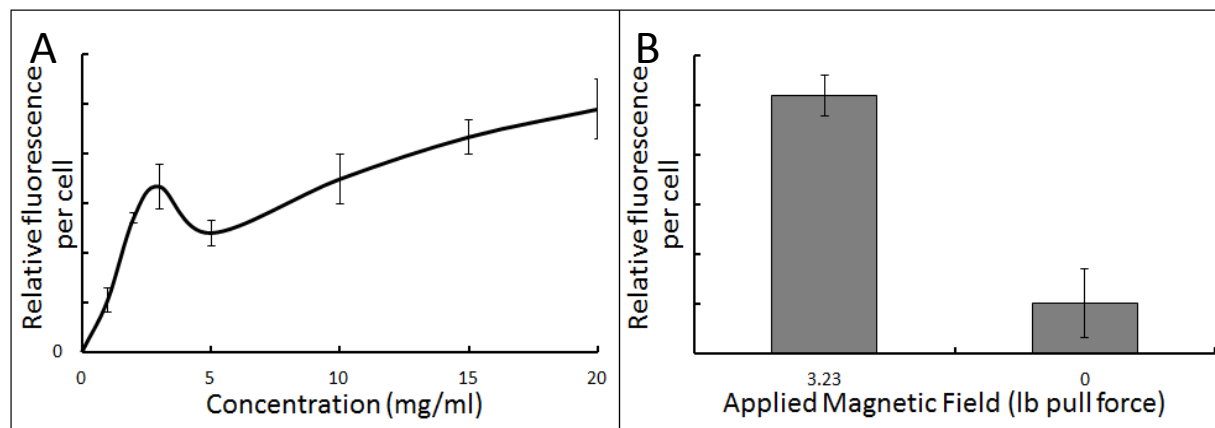


Figure 26. Results of cell uptake and cytotoxicity studies using C6 glioma and rat cortical astrocyte cells (A) Fluorescence quantification of nanocomposite uptake in C6 glioma cells. A spike in nanocomposite uptake is observed at a lower concentration of nanocomposite solution (2.5 mg/mL). (B) Uptake of nanocomposites (0.3125 mg/mL) in C6 glioma cells under the influence of a magnetic field. Increased transfection occurs under the influence of a 3.23 lb pull force magnetic field.

The cell uptake experiment results (Figure 26A) show that these nanocomposites are readily taken up by the cells. The C6 glioma cell uptake was quantified by using fluorescence measurements to understand the transfection of nanocomposites into the cells. A trend of increasing cellular uptake was observed as the incubation concentration of nanocomposites was increased (Figure 26A).

Enhancement of cellular uptake using magnetic fields: Cell uptake of the nanocomposites in the presence of magnetic fields was studied. C6 glioma cells were incubated with a 0.3125 mg/mL solution of nanocomposites for 1 hour in the presence of a magnetic field generated by a 3.23 lb pull force permanent magnet. Figure 26B shows a 5-fold increase in the nanocomposite uptake by the cells in presence of magnetic field (N=5). Similarly, a 300-400% increase in transfection was observed when solutions of 0.625 mg/mL, 1.25 mg/mL, and 2.5 mg/mL concentrations were used in the presence of magnetic fields.

### 3.4.3. Magnetic drug targeting

MDT of our nanocomposites can be achieved by administration via the blood or CSF, both fluids move in a pulsatile manner in the body. To prove magnetic localization, an MDT experiment was conducted to demonstrate magnetic targeting of our nanocomposites. It was repeated twice, with injection volumes of 1mL and 0.5 mL of 0.17 g/mL nanocomposite solution, as shown in Figures 27B and 27C respectively. Digital images were acquired every 2 min to observe the nanocomposite localization at the targeting magnet site. The nanocomposite solution can be observed with normal light due to its dark brown color.

Both experiments indicate an increase in the accumulation of the nanocomposites with time, despite the mixing effect of the pulsatile motion of the fluid. The experiment was stopped at the 10 min time point, because no further increase in nanocomposite CE was observed. Maximum accumulation occurred at the edges of the magnet, as the field strength is the greatest at this region. Almost no nanocomposites were found to cross the magnet and move towards the peristaltic pump, as can be seen in frame 6 of Figure 27B.
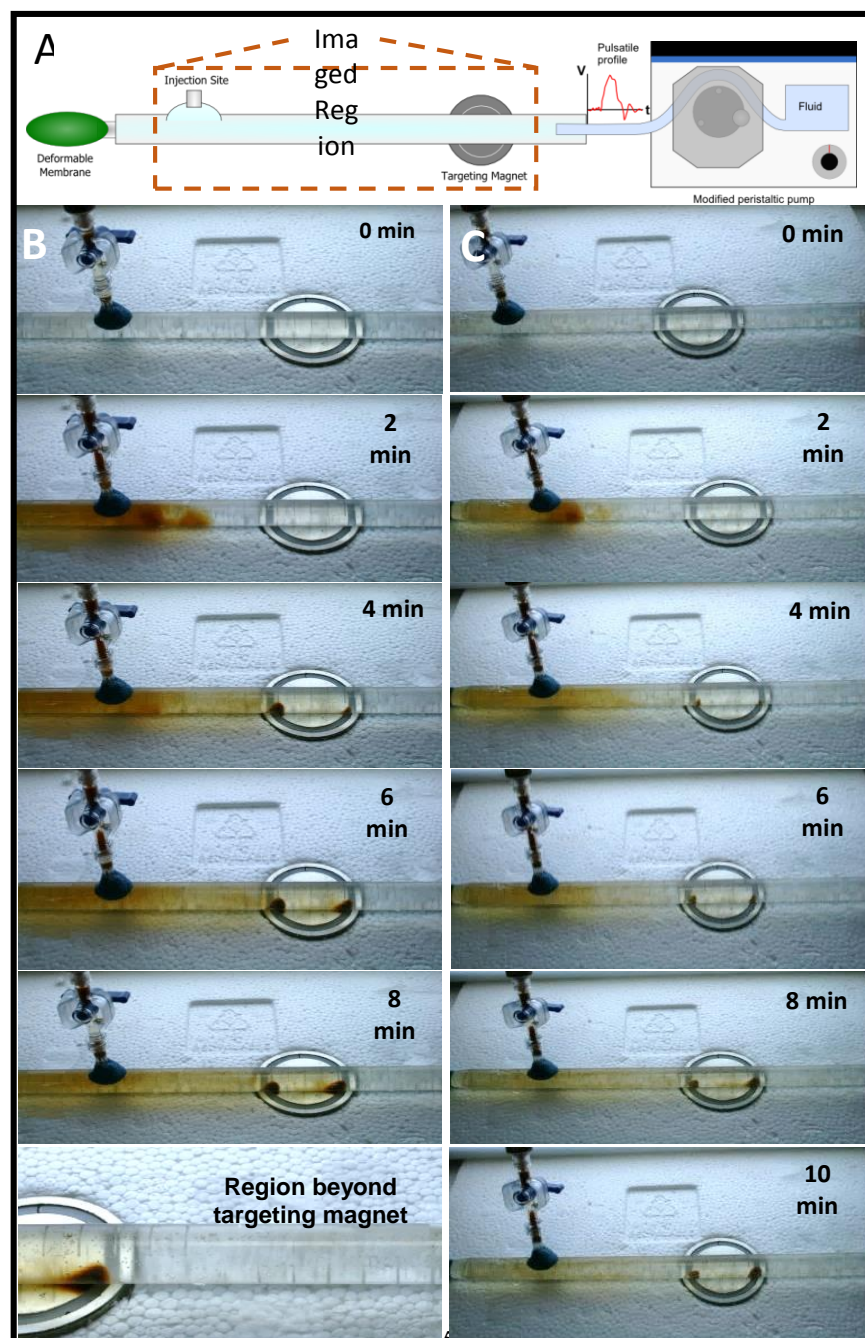
Figure 27. *In vitro* magnetic drug targeting experiment (A) Schematic of the experimental setup containing the injection site, targeting magnet and peristaltic pump to create the pulsatile motion of the fluid (B-C) Images of the MDT experiment showing localization of the nanocomposites at the target site for an injection volume of (B) 1 mL and (C) 0.5 mL.

Such a barrier created by the magnetic field is very useful for drug delivery treatments where a cytotoxic drug should be confined to a target zone, such as a spinal tumor, without spreading to other regions. During both experiments, at least 80% of the nanocomposites were collected at the target magnet site, with larger accumulation observed for the smaller injection volume. Magnet size, shape and field strength can be modulated depending on required drug dosage for therapeutic efficacy.

### 3.4.4. *In vivo* imaging results to prove feasibility of IT-MDT technique

To demonstrate live imaging capability, the fluorescence emission of these nanocomposites was measured through both rat muscle and bone tissue. 200 μL of the nanocomposite solution (2.5 mg/mL) was injected into the abdominal muscle of a Sprague Dawley rat at a depth of 1 cm from the skin surface. FMT images were generated using the IVIS® system. Figure 28 A,B shows that the nanocomposites are clearly visible, demonstrating that deep tissue imaging is feasible using this drug delivery vehicle.

Proving feasibility of IT-MDT technique: We also conducted IT-MDT experiments using these nanocomposites to show the targeting and localization capability of the IT-MDT technique. The nanocomposites intrathecally injected at the lumbar region of the Sprague Dawley rat were localized at the targeting site along the spine corresponding to the placement of the external magnetic field within 20 minutes (Figure 29).  The confinement

of the nanocomposites at a specific site along the spine can be observed in these IVIS

images, which proves IT-MDT's feasibility.
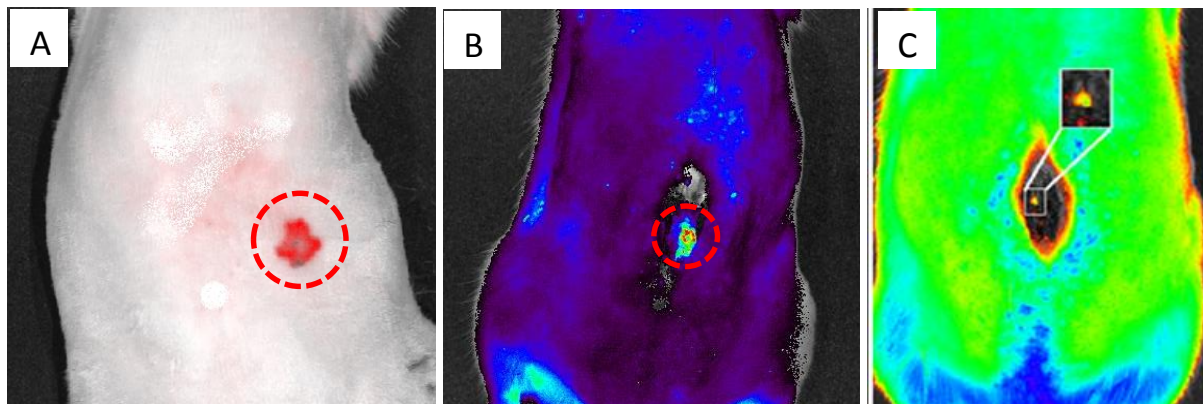


Figure 28. *In vivo* imaging of our nanocomposites using IVIS® system in a Sprague Dawley rat. (A) FMT image of the QD-Fe$_3$O$_4$@Au nanocomposites (200 µL) injected into the abdominal muscle of a rat at a depth of 1 cm; FMT image of the nanocomposites injected into the intrathecal space of a Sprague Dawley rat (B) Injection volume= 200 µL (C) Injection volume= 50 µL.
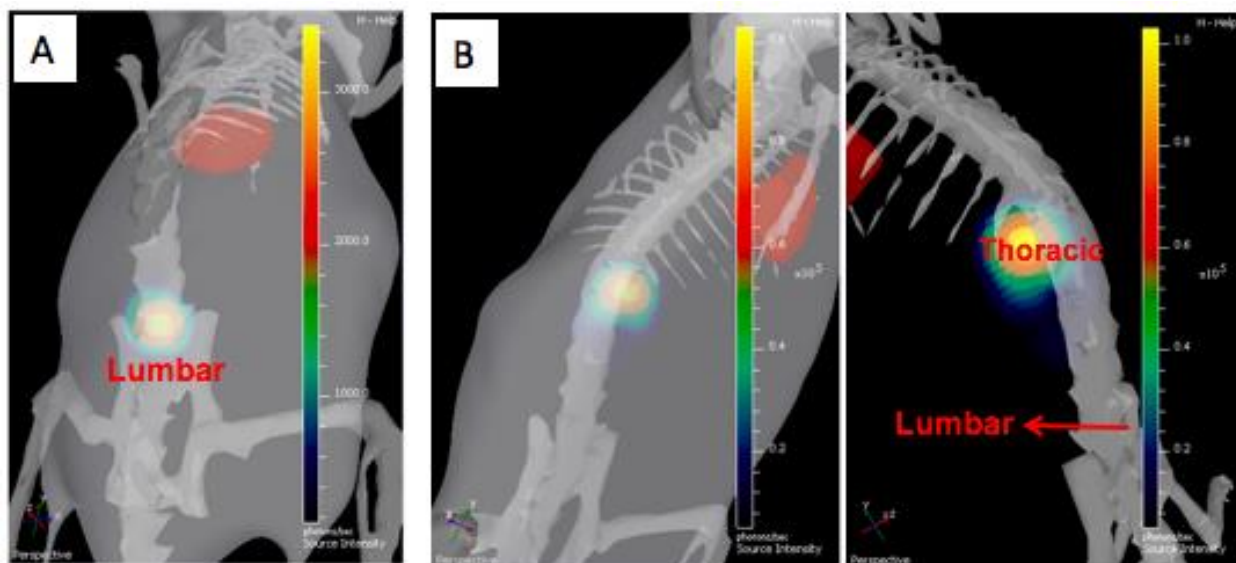


Figure 29. FMT imaging of nanocomposites to prove feasibility of IT-MDT in a Sprague Dawley rat. 20µl of QD-Fe$_3$O$_4$@Au nanocomposites was intrathecally injected in Sprague Dawley rat. (A) FMT image taken immediately after IT injection at L5/L6 region (B) FMT image taken 20 minutes post IT injection showing movement of the nanocomposites to the thoracic region under influence of an external magnet over the spine of the animal.

The fluorescence maps shown in Figures 28 and 29 indicate that visualization is possible through bone and tissue of the spine. The fluorescence emission of the nanocomposites in all environments, especially in *in vivo* environments is significant, indicating its applicability for *in vivo* drug delivery purposes, as shown in Table 4.

| Sample Environment (QD-Fe$_3$O$_4$@Au nanocomposites at a concentration of 2.5 mg mL$^{-1}$ used) | Epifluorescence generated (p sec$^{-1}$cm$^{-2}$sr$^{-1}$)/($\mu$W cm$^{-2}$) |
|---|---|
| 6% agarose gel (depth= 0.25 cm) | 7.68 x10$^8$ |
| 6% agarose gel (depth= 0.5 cm) | 6.02 x10$^8$ |
| *In vivo* (depth = 1 cm): rat flesh | 5.82 x10$^8$ |
| *In vivo* (depth = 0.3 cm): intrathecal space | 2.5 x10$^7$ |
| Table 4: Epifluorescence measurements made from nanocomposites in different environments | |

## 3.5.  Discussion

Our results show the successful synthesis and characterization of a novel drug delivery vehicle for MDT that can be visualized *in vivo* during delivery to the targeted disease site. The magnetic core of the nanocomposite is superparamagnetic, therefore, targeting drugs using this vehicle via MDT is possible. External magnetic fields can arrest the nanocomposites within any targeted region, despite the convective transport and mixing effect caused by the pulsatile motion of CSF as shown by the *in vitro* MDT experiment. Moreover, the cellular uptake experiments demonstrated internalization of nanocomposites in tumor cells. The vehicle was successfully visualized various environments (cellular, *in vitro* and *in vivo*) using FMT techniques, offered by commercial imaging equipment such as the IVIS® system (Caliper Life Sciences).

All the necessary attributes for an MDT drug delivery vehicle have been attained in our nanocomposites, such as magnetic guidability and *in vivo* imageability. Drug functionalization can also be achieved due to the affinity that gold has for sulfur-containing

functional groups and bonds (e.g. thiol and mercapto bonds), which are found in many proteins, pharmaceutical and biopharmaceutical drugs. Unlike previous studies which suffered fluorescence quenching after gold surfaces conjugation ([124], [125]), our QD conjugation retained strong fluorescence emission even after conjugation to the gold-coated MNP. Fluorescence emission from our nanocomposite structure was stable over a three-week period, demonstrating its suitability for longer term experiments. The gold and $Fe_3O_4$ of our nanocomposites are biocompatible. $Fe_3O_4$ degrades into its components and can be integrated in normal iron homeostasis, without posing a threat ([126], [127]).

A disadvantage of our system is that the CdTe QDs are not biocompatible. It was observed that concentrations of upto 20 mg/mL of our nanocomposites containing CdTe QDs were taken up by cells over a period of 5 hours. However, higher concentrations would lead to toxic effects. One of the key steps in our future work will be to synthesize CdTe QDs with a shell of another compound such as ZnS to prevent release of $Cd^{2+}$ ions, which has a detrimental effect on cells [128]. Our CdTe QDs capped with thiol bonds are synthesized using 3 mercaptopropionic acid. Another possibility would be to use a different stabilizer during the synthesis process, such as tripeptide glutathione (GSH) instead of the 3 mercaptopropionic acid. This would result in biocompatible CdTe QDs capped with GSH group [129]. The GSH group contains a sulfur atom, and QDs capped with GSH can be loaded on the gold surface of our nanocomposite using a similar technique as mentioned in the methods section of this chapter. GSH can be used to detoxify $Cd^{2+}$ ions in medicine due to its chelating capability [130].

We believe that for IT-MDT, the drug dosages used would be much lower compared to systemic delivery, as the therapeutic molecules can be specifically delivered at target

sites. Therefore, a very high concentration of our nanocomposites would not be used for drug delivery. Also, *in vivo* studies suggest that, regardless of the nature of the QDs, vertebrate systems tend to recognize them as foreign, with rapid elimination of the materials through the primary excretory-organs/systems: the liver, spleen, and lymphatic systems[131]. Once inside the target cell, gold-thiol bonds are rapidly broken due to the reducing environment of the cell cytoplasm, and the QDs will be released from the $Fe_3O_4$@Au nanoparticle core. QDs of sizes similar to the ones that we use can be easily and efficiently cleared from the body[131]. Specific biocompatibility studies would be needed for the definite concentration ranges that are safe for therapeutic application.

A possible future work relating to these experiments would be to understand the effect of size and shape of the QD-gold nanocomposites on their cellular uptake. Several papers, such as Chitrani (2006) [132] mention that rod shaped gold nanoparticles are taken up more easily when compared to the spherical particles. The same paper also demonstrated that gold nanoparticles of a specific diameter range (50 nm) showed significant increase in cellular uptake. Based on such observations, we can optimize the parameters of our synthesis process to generate nanocomposites of a specific size range for better cell internalization.

# 4.MAGNETIC FIELD-ENHANCED CELLULAR UPTAKE OF DOXORUBICIN LOADED MAGNETIC NANOPARTICLES FOR TUMOR TREATMENT

## 4.1. Summary

Cancer remains the second most common cause of death in the US, accounting for nearly 1 out of every 4 deaths. In recent years, several varieties of nanoparticles have been synthesized with the intent of being utilized as tumor drug delivery vehicles. In this chapter, synthesis and characterization of superparamagnetic, gold-coated magnetite nanoparticles and loaded them with the chemotherapeutic drug doxorubicin (DOX) for MDT or IT-MDT of tumors. The synthetic strategy uses the food thickening agent *gellan gum* (Phytagel) as a negatively charged shell around the $Fe_3O_4$@Au nanoparticle onto which the positively charged DOX molecules are loaded via electrostatic attraction. The resulting DOX-loaded magnetic nanoparticles (DOX-MNPs) were characterized using transmission electron microscopy, energy dispersive x-ray spectroscopy, superconducting quantum interference device magnetometry, surface area electron diffraction, zeta potential (ZP) measurements, fourier transform infrared spectroscopy (FTIR) as well as UV/Vis and fluorescence spectroscopy. Cytotoxicity of DOX-MNPs was demonstrated using MTT assay on C6 glioma cells. Cellular uptake of DOX-MNPs was enhanced with magnetic fields, which was quantitatively determined using flow cytometry. This improved uptake also led to greater tumor cell death, which was measured using MTT assay. These results, detailed in this chapter, are promising for a new IT-MDT therapy for cancer.

## 4.2.    Introduction

Cancer research has been successful as in decreasing in overall death rates between 1991 and 2010, by about 20% in both men and women[133].  The cancer treatment protocol for most cancers requires chemotherapy.  Unfortunately, most chemotherapeutic agents exhibit poor specificity in reaching tumor tissue in addition to dose-limiting toxicity. Thus, many patients experience adverse side effects due to the administered chemotherapy treatments.

New drug delivery strategies are being developed to improve efficacy of cancer patient treatments, while minimizing systemic toxicity.  One promising treatment involves using nanoparticles as a means of targeting cytotoxic drugs to specific tumor cells and tissue, thereby limiting systemic exposure. In the use of nanoparticles for drug therapy, the drug is dissolved, entrapped, encapsulated, or attached to the nanoparticles. The major goals in the design of nanoparticles for drug delivery include: (i) control of particle size, (ii) variation of surface properties, and (iii) ability to release of pharmacologically active agents to achieve the site-specification of the drug at the therapeutically optimal rate and dose regimen. Novel nanoparticle -based applications for cancer treatments are being explored because of their ability to (i) decrease toxicity and the occurrence of adverse reactions, (ii) utilize drug more effectively, (iii) control the rate and site of drug release, (iv) provide a more predictable drug delivery system ([87], [134], [135]).

Currently, there are two different types of targeting utilized by scientists studying nanoparticles drug delivery systems for cancer.  *Passive targeting* exploits the enhanced permeability and retention effect that is defined by leaky vasculature around tumors caused by tumor-induced angiogenesis with incomplete endothelial cell junctions, resulting

in the accumulation of the nanoparticles at the tumor site [136].  This passive targeting

strategy has been shown to be an efficient method to reduce the toxic side effects and

increase the therapeutic index of drug molecules ([137], [138]). *Active targeting* usually

involves attaching ligands on the surface of nanoparticles, which bind to over-expressed

receptors on tumor cells. Targeting specific surface receptor causes selective uptake of

nanoparticles by the cancer cells [139].  Active targeting may also involve utilizing physical

stimuli for actively localizing nanoparticles to the target site, including temperature, pH,

electric charge, light, sound and magnetism ([140], [141]). The IT-MDT method, is an active

targeting technique, which aims at utilizing magnetism as a physical stimulus, for efficient

targeting of specific cells.

Synthesis of magnetic microparticles and MNPs for the delivery of

chemotherapeutics has evolved since the 1970s. Zimmerman and Pilwat in 1976 studied

the delivery of cytotoxic drugs using magnetic erythrocytes [142].  The targeting of

magnetic albumin microspheres encapsulating the anticancer drug DOX in animals was

studied by Widder [143].  Engelhard and Petruska studied the movement of magnetic

microparticles in rat CSF and brain in 1992 [144]. Hafeli synthesized biodegradable

polylactide microspheres that incorporated magnetite and the beta radiation-emitter Y-90

for radiotherapy targeting in 1994 [145], and successfully applied it to subcutaneous

tumors [146].  However, these studies employed micrometer-sized magnetic particles.  Use

of MNPs was described for the first time by Lubbe and colleagues  in 1999 [147].  MNPs

loaded with epirubicin were administered intra-arterially in a phase-1 clinical trial for

patients with advanced cancers. Several groups and start-up companies have synthesized

magnetic vectors and shown potential applications of MNPs.  These include MNPs used in

MRI [98], magnetic fluid hyperthermia ([97], [148]), cell sorting and targeting ([149], [150]), bioseparation [151], enzyme immobilization [152], immunoassays ([153], [154]), and gene transfection and detection systems ([155], [156]).

Different varieties of MNPs have been coated with a "shell" of either organic or inorganic nature [157] to exploit specific properties. Nanoparticle coatings often regulate the solubility, hydrophilic or hydrophobic properties, stability, and the targeting ability of the particles.  For example, Yang synthesized a poly [N-(1-one-butyric acid]) aniline shells around $Fe_3O_4$ cores that have been further conjugated with 1,3-bis(2-chloroethyl)-1-nitrosourea [158].  Ito and colleagues have synthesized antibody-conjugated magnetoliposomes which can used as carriers to introduce magnetite nanoparticles into target cells, since the negatively-charged cell surface interacts with the positively-charged surface of the nanoparticles [112]. Inorganic shells have also been incorporated in MNP synthesis, most notably silver, gold or titanium ([110], [159], [160]).

DOX is a chemotherapeutic drug, and its mechanism of action involves intercalating into the DNA of cancer cells and preventing cell replication.  It is widely used to treat various cancers including leukemias, Hodgkin's lymphoma, and cancers of the bladder, breast, stomach, lung, ovaries, thyroid, soft tissue sarcoma, multiple myeloma, and others. It is an FDA approved drug, currently being marketed under the names Adriamycin, RUBEX and DOXIL. Various research groups have loaded DOX on organic or inorganic nanoparticle shells for better drug delivery ([161]–[166]).

In this chapter, we demonstrate (i) a new technique of loading DOX on SPIONs and (ii) enhancement of their uptake into tumor cells in the presence of magnetic fields. The resulting DOX-MNP particles is a promising vehicle for tumor treatment applications via

MDT. The magnetite core of the DOX-MNP, which was synthesized via a co-precipitation method (as described in previous chapters), was coated with a gold shell to form the $Fe_3O_4$@Au nanoparticles. The polymer gellan gum was coated on the surface of the $Fe_3O_4$@Au nanoparticle which resulted in a negatively charged nanoparticle ($Fe_3O_4$@Au-GG) due to the carboxylate groups of the gellan gum ([167], [168]).  The positively-charged amine groups of DOX molecules are electrostatically attracted to the negatively-charged gellan gum surface, which resulted in the final DOX-MNPs.

The efficacy of DOX-MNPs to kill glioma cells has also been described, as well as the enhancement in their cellular uptake in the presence of a static magnetic field. Increased endocytosis of plain MNPs via magnetic fields has been previously observed, especially to overcome the hurdle of gene delivery across cell membranes ([169]–[173]). In this paper, we show an elevated level of cellular uptake of the tumor drug loaded MNPs and consequently, increased drug efficacy and cell death caused by the presence of magnetic fields. This enhancement makes our drug vehicle an ideal candidate for IT-MDT. The targeting and augmented cellular uptake using magnetic fields via our DOX-MNPs can be used to target DOX to specific tumor sites, and thus improve efficacy *in vivo.*

### 4.3.   **Materials and Methods**

Equipment utilized for synthesis and characterization include a 40 Watt DC Motor with variable electric stirrer, IEC Centra MP4R Centrifuge, Fisher Vortex Genie 2, TH20 Sonicator, Axioskop Fluorescent Microscope with Axiocam (Zeiss), Zetasizer (Malvern), Fourier Transform Infrared spectrophotometer (Bruker Tensor 27 FT-IR & OPUS Data Collection Program), Transmission electron microscope (JEOL JEM-1220), Confocal microscope (Zeiss LSM 510 META), NanoDrop 1000 UV-Vis spectrophotometer and

NanoDrop 3300 Fluorimeter. All chemicals were purchased from Sigma-Aldrich® except for DOX (LC Laboratories®) and hydrogen tetrachloroaurate (III) hydrate (Alfa Aesar ®).

### 4.3.1. Synthesis of Gold-Coated Magnetite Nanoparticles (Fe$_3$O$_4$@Au nanoparticle)

The Fe$_3$O$_4$@Au nanoparticles were synthesized by a coprecipitation technique, described in various articles ([42], [110]) using ferrous and ferric salts to form Fe$_3$O$_4$. These Fe$_3$O$_4$ cores were then coated with a layer of gold by a surface adsorption technique. The detailed procedure is described in the previous publications as well as in the Appendix Section A.

### 4.3.2. Conjugation of DOX to Fe$_3$O$_4$@Au nanoparticle via Gellan Gum

An aqueous solution of gellan gum (Phytagel™) was prepared by slow addition of 5 mg of Phytagel™ to 90 mL of water while heating using a magnetic stirring hotplate. Water was added till the solution volume reached 100 mL. The pH of the solution was adjusted to 10 by dropwise addition of 0.16 M NaOH solution. The solution was heated to 70$^o$C while being stirred. After removing from heat, 1.6 mL of 40 mg/mL Fe$_3$O$_4$@Au nanoparticle solution was added dropwise to the gellan gum solution while it was being non-magnetically stirred. The solution was cooled to room temperature and stirred for 1 hour. The Fe$_3$O$_4$@Au nanoparticles were recovered using magnetic decantation and washed 3-4 times with distilled water. In a dark room, 3.0 mg of DOX was dissolved in 1 mL of nanopure water, which was then added dropwise to the solution, while it was being stirred slowly. The solution was stirred non-magnetically for 24 hours. The resulting DOX-MNPs were magnetically decanted and washed several times with water. The DOX-MNPs were then resuspended in water to a concentration of 40 mg/mL.

<u>Estimation of loading of DOX on the $Fe_3O_4$@Au-GG nanoparticles:</u> A known weight of DOX was added to an aqueous dispersion of $Fe_3O_4$@Au-GG nanoparticles of known volume and concentration. This was then stirred for 24 hours in the dark. The DOX-MNPs formed were magnetically decanted and the supernatant was collected. Weight of DOX in the supernatant was determined by both UV-Vis and well as drying/weighing it.

The % loading of DOX was calculated by using the formula shown in equation:

$$\% \text{ loading} = \frac{(\text{Total weight of Dox} - \text{ Weight of Dox in supernatant})}{\text{Total weight of Dox}} * 100$$

### 4.3.3. Confocal Microscopy and Flow Cytometry

DOX-MNPs of various concentrations were incubated with C6 glioma cells grown on (i) confocal dishes with coverglass bottoms for the confocal microscopy experiment and (ii) cell culture multiwall plates for the flow cytometry experiment. After treatment with DOX-MNPs, the cells were thoroughly washed with PBS and fixed by incubation in a 4% paraformaldehyde solution for 20 minutes at 37°C. 0.25mL of a 1:2000 concentration solution of phalloidin (Santa Cruz Biotechnology Phalloidin CruzFluor™ 488 Conjugate) was then added to each well and incubated for 2 hours at 4°C. After the phalloidin was removed, 0.25 mL of 2.5 µg/mL concentration of DAPI solution was added to each well for 5 minutes at 4°C. After washing with PBS to remove the DAPI, the cells were analyzed using a confocal microscope. For the flow cytometry experiment, the cells were removed from the multiwall plates using trypsin and suspended in PBS, before analysis.

### 4.3.4. Cell TEM

DOX-MNP treated cells were scraped from the culture flask and centrifuged at 2000 rpm for 20 min, then fixed with 2.5% glutaraldehyde. The cell samples were dehydrated by an ethanol series, and embedded in epon. Ultra-thin sections of 83 nm were double

contrasted with Reynolds lead citrate and 2% uranyl acetate, and imaged in a JEOL JEM-1220 (fitted with a Gatan digital camera) at an accelerating voltage of 80 kV.

### 4.3.5. MTT assay

DOX-MNPs of various concentrations were incubated with C6 glioma cells grown on a 96 well plates. For the cellular uptake experiment involving magnetic fields, a small circular permanent magnet of 0.33 T was placed directly below specific well during the incubation period. The cells were thoroughly washed with PBS to remove DOX-MNPs that were not taken up by the cells. 50μL of MTT stock solution (10% v/v solution of MTT and cell growth media) was added to each well. After incubation for one hour, the MTT solution was removed and 200μL of DMSO was added to each well. The plate was then incubated for 20 minutes before measuring the absorbance from each well using an optical plate reader, at a wavelength of 570 nm.

### 4.4. Results

### 4.4.1. Synthesis and Characterization

TEM, EDS and SQUID magnetometry results of $Fe_3O_4$@Au nanoparticles: The characterization results of the $Fe_3O_4$@Au nanoparticles have been described in detail previously in Chapters 2&3 (please refer Figures 43, 7, 12 and 13). Figure 30A shows a TEM image of DOX-MNPs, in which the gellan gum polymer coating on the $Fe_3O_4$@Au nanoparticles can be seen clearly. A histogram showing the size distribution of the DOX-MNPs is given in Figure 30B, which indicates that most nanoparticles have a diameter of 95-105 nm (Figure 30). The sizes of the DOX-MNPs varied between 75 nm and 150 nm. Due to the variability in the size of the DOX-MNPs, there is a possibility that they are multi-core particles rather than single core particles, or a mixture of both types. Encapsulation of

magnetic cores using a polymer matrix can result in multi-core particles [174], which is

similar to our synthesis procedure.
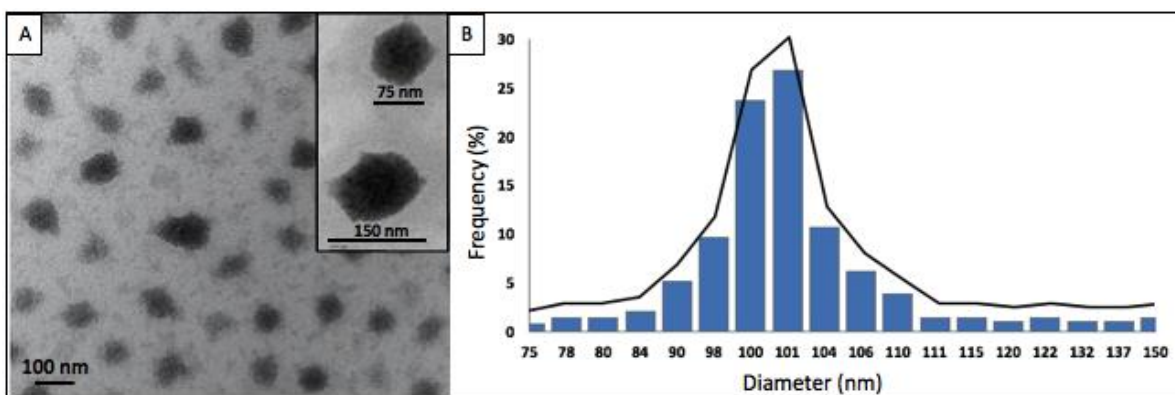


Figure 30. (A) TEM image showing multiple DOX-MNPs. Inset shows HRTEM images of
DOX-MNPs; (B) Histogram of the size distribution of DOX-MNPs.

Zeta potential measurements: Measurement of ZP was one of the techniques used to

confirm loading of DOX molecules on the surface of the $Fe_3O_4$@Au MNPs. These MNPs were

coated with the biocompatible polymer *gellan gum*, a food thickening agent. The

carboxylate groups of the gellan gum lend a negative charge to the MNP surface, which

electrostatically attracts DOX's positively charged amine groups. The positive ZP of the

$Fe_3O_4$@Au MNPs, +11.6, decreases to -27.3 after coating with the negatively charged gellan gum. After loading the positively charged DOX molecules, the
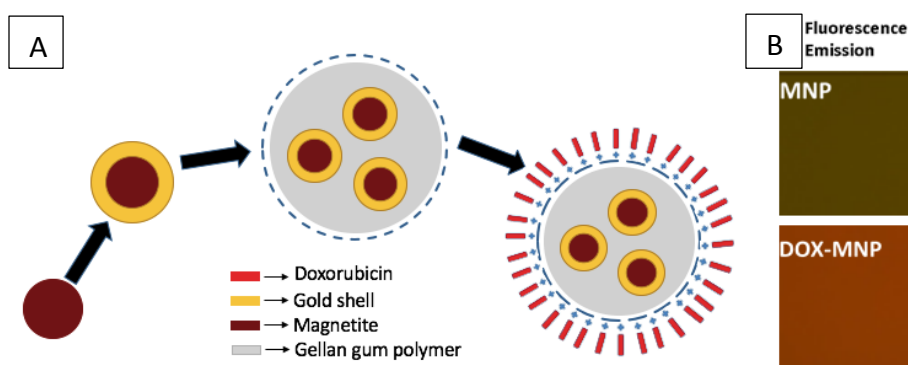


Figure 31. Characterization of DOX-MNPs (A) Schematic of the synthesis
of DOX-MNPs; (B) Fluorescence microscope images of $Fe_3O_4$@Au
nanoparticles and the fluorescent DOX-MNPs.

ZP increases to -15.4, confirming DOX loading. The conjugation of DOX to MNP was also

confirmed by using fluorescence microscopy. As DOX is fluorescent, DOX-MNPs fluoresce, emitting a red color (at 590 nm) when compared to $Fe_3O_4$@Au nanoparticles (Figure 31B).

Fourier Transform Infrared Spectroscopy results: Loading of the DOX molecules to the MNP was also confirmed using FTIR spectroscopy. Figure 32A shows the FTIR spectra of the $Fe_3O_4$@Au-GG nanoparticles. The presence of the gellan gum polymer on its surface is indicated by the presence of a broad O-H peak at 3400 $cm^{-1}$, glycosidic bonds are indicated by the peak at 1640 $cm^{-1}$, C-H bending peak at 1409 $cm^{-1}$ and C=C bond at 1500 $cm^{-1}$. Figure 32B shows the FTIR spectra of the DOX-MNPs (blue) superimposed on the free DOX solution spectra (red). Both spectra were found to have regions with similar peaks, circled in pink in Figure 32B, with the same x-axis ($cm^{-1}$) values. This confirms the presence of DOX on the DOX-MNP surface.
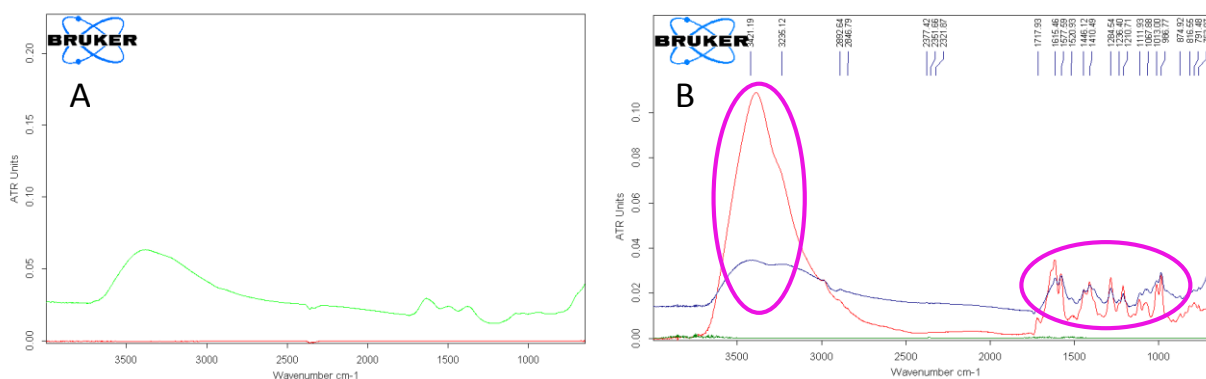


Figure 32. FTIR spectra of (A) $Fe_3O_4$@Au-GG nanoparticles; (B) Free DOX (red) and DOX-MNPs (blue). The pink circles indicate the common peaks present in both FTIR spectra, which confirms the presence of the DOX molecules on the DOX-MNP surface.

Absorption and Fluorescence Emission Spectra: The stability of DOX molecules after loading on $Fe_3O_4$@Au-GG nanoparticles were studied by using fluorescence and UV-Vis spectroscopy. The absorption/excitation spectra of free DOX and DOX-MNPs (green and brown lines respectively in Figure 33A) indicate that both have an absorption maximum at 480 nm.  The emission spectra of DOX in solution and DOX-MNPs were recorded from 500

70

to 700 nm at a fixed excitation wavelength of 480 nm; the spectra recorded are shown in Figure 33B. There was no change in the spectral profile of DOX-MNPs when compared to DOX molecules, and the emission peak at 597 nm was retained.
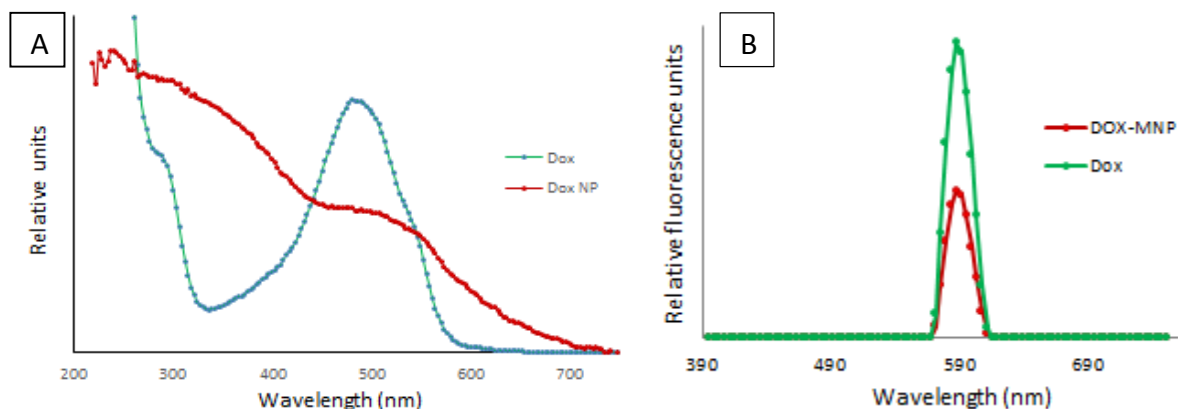


Figure 33. Spectral characterization of DOX-MNPs (A) Excitation spectra of free DOX and DOX-MNPs showing a peak at 480 nm; (B) Fluorescence emission spectra of free DOX and DOX-MNPs showing a peak at 590 nm. Similar emission spectra indicate that the DOX structure has been retained after being loaded on the $Fe_3O_4$@Au-GG nanoparticle surface.

DOX loading efficiency: The DOX loading efficiency on the $Fe_3O_4$@Au-GG nanoparticles was determined to be 70% using the procedure mentioned in the methods section of this chapter. Our measurements showed that 1mg of $Fe_3O_4$@Au-GG nanoparticles contain 0.31 mg of DOX loaded on its surface.

### 4.4.2. Confocal microscopy results

Confocal microscopy was used to observe the cellular uptake of DOX-MNPs in C6 glioma cells. The actin cytoskeleton and nuclei of the cells were stained using
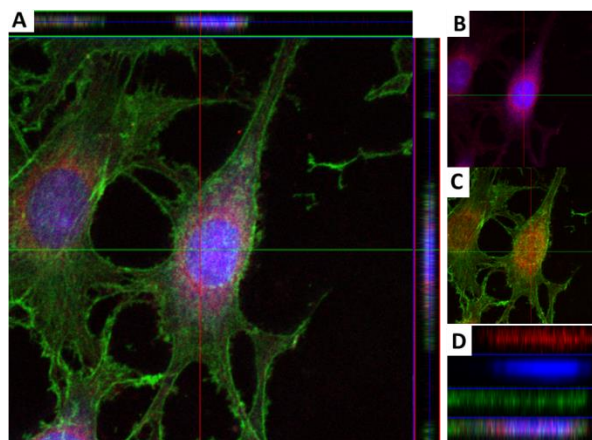


Figure 34. Confocal microscopy image of C6 glioma cells that have endocytosed DOX-MNPs (red). Actin stained by phalloidin is green, and the nucleus stained by DAPI is blue. (A) Z-stack images are acquired to visualize the depth of the cell and confirm MNP uptake. The orthogonal plane borders the main image (B) DOX-MNPs localize into the nucleus (C) Phalloidin highlights the cell boundary showing the drug is present only inside cells (D) From top to bottom all three fluorescent markers are shown to confirm colocalization with the cell.

phalloidin (green) and DAPI (blue) respectively; the DOX-MNPs are naturally fluorescent. Peak emission wavelengths for phalloidin, DAPI, and DOX-MNPs are 460 nm, 518 nm, and 597 nm respectively. Figure 34 shows the confocal microscopy images that confirm DOX-MNPs were taken up into the cells.

### 4.4.3. DOX-MNP efficacy studies

MTT assay results: Cytotoxicity of DOX-MNPs for killing tumor cells was tested using MTT assay. The assay is dependent on the ability of viable cells to metabolize a water-soluble tetrazolium salt into a water-insoluble purple colored formazan product. The intensity of the purple color obtained from the resulting absorbance spectrum, is a direct indicator of the cell viability [175]. Various concentrations of the DOX-MNPs (4 -0.125 mg/mL) were incubated with C6 glioma cells cultured in 96 well plates. MTT assay was performed to determine the percentage of non-viable cells, which is an indicator of the efficacy of the DOX-MNPs. The experiment was also repeated by placing small permanent magnets of 1.47 lbs pull force strength (0.33 T) beneath the wells of the cell plate during the incubation period with the DOX-MNPs (Figure 36A). Confocal microscopy images (Figure 35) showed that the presence of magnetic field significantly increased the DOX-MNP uptake, as indicated by the higher emission of fluorescence from within the cells.
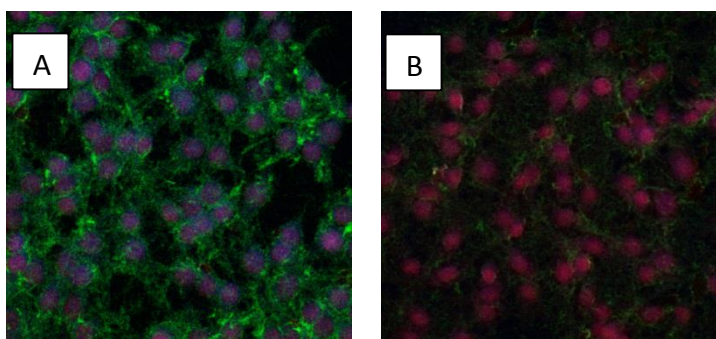


Figure 35: Uptake of 1mg/mL DOX-MNPs by C6 glioma cells in 30 minutes (A) without magnetic field; (B) in the presence of 0.33 T magnetic field. Cellular uptake is increased in the presence of the magnetic field.
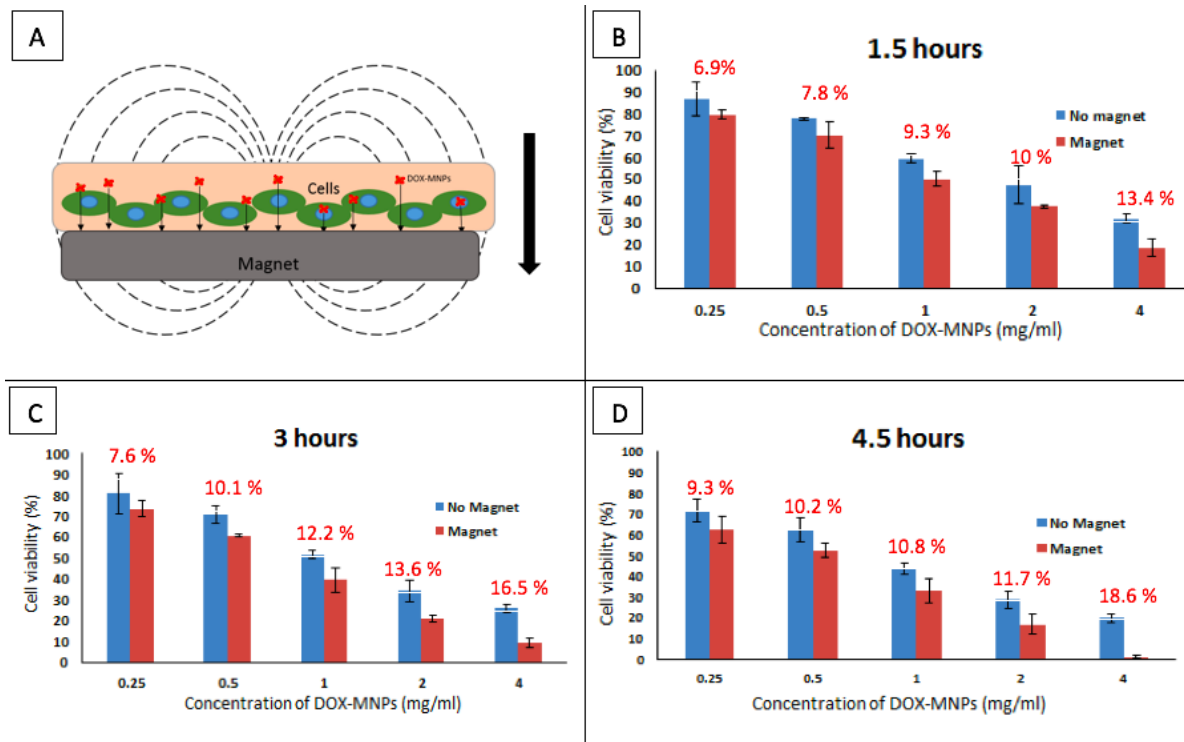
Figure 36. MTT assay results (A) Permanent magnet placed below the cell well enhances DOX-MNP uptake. The arrow indicates the direction of movement of DOX-MNPs towards the magnet; MTT assay results showing the decrease in cell viability in the presence of magnetic field (0.33 T) after incubation periods of (B) 1.5 hours (C) 3 hours and (D) 4.5 hours using various concentrations of DOX-MNPs. The difference in the % reductions of cell viability between the control and the magnet experiment have been given in red, above the bars of the corresponding experiment.

The MTT assay results show a reduction in C6 glioma cell viability with increasing concentration and treatment duration using DOX-MNPs, in both the magnetic and no magnetic field exposure (control) groups. Also, the glioma cell viability was reduced with exposure to the magnetic field when compared to the no magnetic field exposure (control) group, for the same duration of DOX-MNP treatment.

TEM results: TEM images of the C6 glioma cells were taken after incubation with 2 mg/mL DOX-MNP solution for 30 minutes. The first and second row of images in Figure 37 show TEM images of cells that were incubated with and without the influence of a 0.33 T magnetic field respectively.
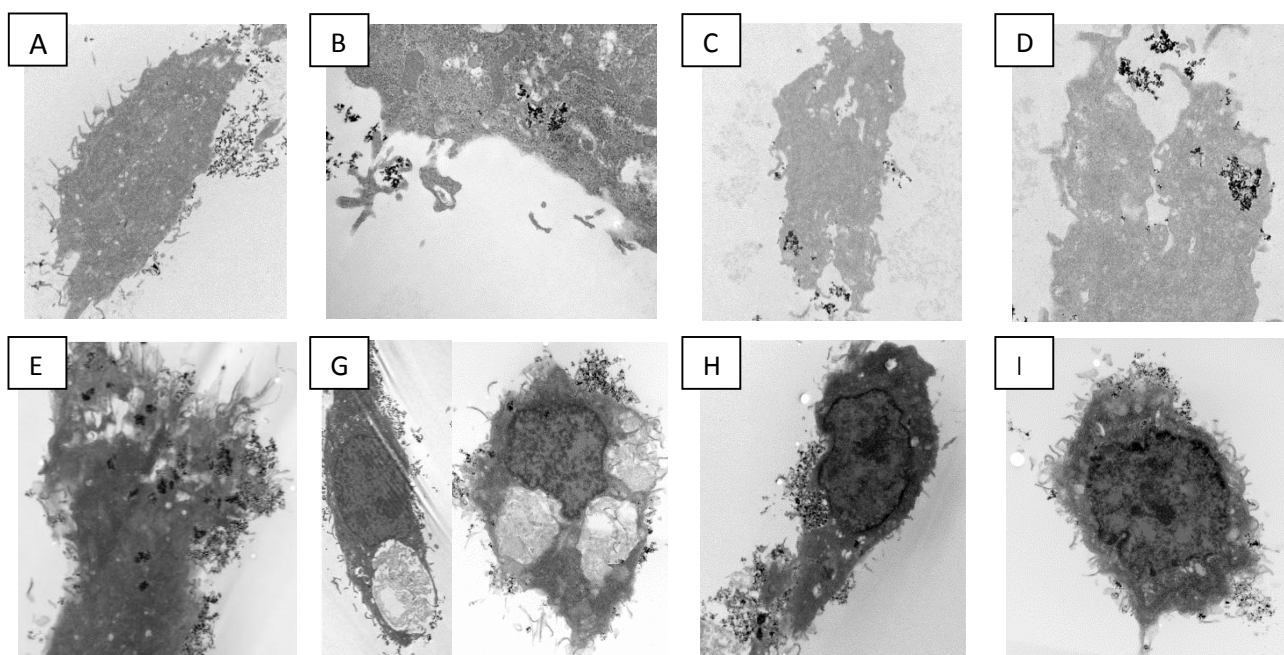
Figure 37. TEM images of cells post incubation with DOX-MNPs (A)(B)(C)(D) Cells were incubated with 2mg/mL of DOX-MNPs for half hour. (E)(F)(G)(H) Cells were incubated with 2mg/mL of DOX-MNPs for half hour under the influence of a 0.33T permanent magnet field.

The images in the first row show relatively intact tumor cells with less DOX-MNPs uptake. The images in the second-row exhibit higher DOX-MNP uptake. These cells also have a reduced cytoplasm volume (Figure 37 H,I) and show more autophagic vacuoles indicative of waste expulsion (Figure 37 G).  Reduced cytoplasm and presence of autophagic vacuoles have been generally taken as indicators of dying cells ([176]–[178]).

Flow cytometry results: Flow cytometry was used to determine the cellular uptake ratio of DOX-MNPs in the absence (M-) and presence (M+) of a magnetic field. Figure 38 shows the relative fluorescence in the C6 glioma cells after incubation with DOX-MNP solutions (concentrations ranging from 0.25 mg/mL to 2 mg/mL). The results shown suggested an enhancement in the cellular uptake of DOX-MNPs in the presence of the magnetic field. Presence of the magnetic field also increased the total number of cells that showed fluorescence at the end of the treatment, when compared to

the control group (M-). For example, when the cells were incubated with a 1 mg/mL DOX-MNP solution, fluorescence was detected in 93% of all M+ treated cells, compared to only 78% in the case of M- treated cells. Similar increase of 10-15% was observed in cell uptake ratio between M+ and M- treated cells for all incubation concentrations of DOX-MNPs.
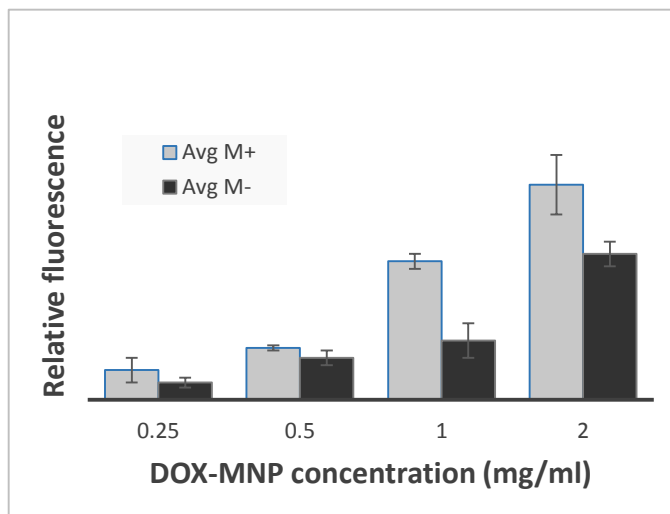


Figure 38. Flow cytometry evaluation of the magnetic enhancement of DOX-MNP uptake. The relative fluorescence in the C6 glioma cells at different DOX-MNP concentrations after incubating for 45 min. For all concentrations, cellular uptake is higher in the presence of magnetic fields (M+), compared to the control group (M-).

## 4.5.    Discussion

In this chapter, we described detailed synthesis of a tumor drug delivery platform for magnetic targeting. The individual components of the delivery vehicle are not toxic: gold, $Fe_3O_4$ and the gellan gum polymer are biocompatible. $Fe_3O_4$ degrades into its components which are integrated in normal iron homeostasis in the body ([126], [127]). Gold is a stable unreactive metal, which has been used in several nanoparticle based drug formulations ([179], [180]). Gellan gum is a bacterial anionic deacetylated sugar polysaccharide secreted by *Pseudomonas elodea* that has been found to be biodegradable and biocompatible [181].

Due to the variability in the size of the DOX-MNPs, there is a possibility that they are multi-core particles rather than single core particles, or a mixture of both types. Both hydrogen bonding and Vanderwall's forces are involved in formation of gellan gum matrix

structure that encapsulates the magnetic core(s) [182]. Due to the superparamagnetic nature of the individual $Fe_3O_4$@Au cores, the multi-core particles are also superparamagnetic, and this does not affect the particle's ability to deliver therapeutic molecules. Similar experiments conducted by other researchers have also concluded no loss of in the fast relaxation time of SPIONs after being entrapped as multi-core particles in a polymer shell [174]. Therefore, these particles can be successfully used for magnetic drug targeting in tumor treatment.

Synthesis parameters such as temperature, reagent concentrations, surfactant concentrations and stirring speed can affect the sizes of multi-core particles. Production of multi-core particles with good control of the number of magnetic cores per particle, and of the degree of polydispersity of the core sizes, remains a difficult task [183]. One of the main factors that we have attempted to optimize is the amount of gellan gum added to the system. Other papers, such as Dhar and colleagues used smaller quantity of gellan gum (0.02% w/v) to reduce and cap their gold nanoparticles ([181], [184]). In our gellan gum coating protocol, we used a 5% w/v solution to accommodate for the larger size of our $Fe_3O_4$@Au nanoparticles. The amount of gellan gum added to the system was adjusted to obtain maximum DOX conjugation on the surface of the nanoparticle, while maintaining an adequate particle size for drug delivery purposes. 81% of our DOX-MNPs have a mean diameter of around 100 nm, which is is suitable for both systemic and intrathecal delivery.

Confocal microscopy was used to confirm cellular uptake and nuclear localization of DOX-MNPs. The DOX-MNPs were successfully endocytosed into the C6 glioma cells, and the z-stack image of the nucleus clearly shows co-localization with the DOX molecules, which is also the site of therapeutic action for DOX.

FTIR spectroscopy was also used to confirm DOX loading. From the emission

spectra, we inferred that the fluorescence signature of DOX is preserved after conjugation

on the $Fe_3O_4$@Au-GG nanoparticle surface. Therefore, the DOX molecular structure is

retained following loading on MNPs, which is important for its biological activity.

The efficacy of DOX-MNPs to kill tumor cells was determined by using MTT assay.

Cell viability graphs showed that DOX-MNPs killed tumor cells, even over short incubation

periods (1.5 hours), when a magnetic field is present. The efficacy to kill cells under the

influence of a magnetic field, was more pronounced in greater DOX-MNP concentration

experiments, which indicates that this effect is due to increased endocytosis of DOX-MNPs

into the C6 glioma cells. Any aggregation of the DOX-MNPs, which might have been caused

by application of the external magnetic field, did not adversely affect its endocytosis and

more importantly, the tumor drug efficacy.

The enhanced DOX-MNP uptake in the presence of magnetic field was also

qualitatively and quantitatively determined using TEM and flow cytometry respectively.

The TEM images indicated increased destruction of C6 glioma cells in the presence of a

magnetic field. Flow cytometry clearly quantified the enhancement in both the cellular

uptake ratio and the DOX-MNP uptake due to the magnetic field.

We believe that the increased transfection in the presence of magnetic fields can be

attributed to the magnetization of the MNPs as well as an additional attractive force

(direction of arrow in Figure 36A) generated by the magnetic field, which enhances their

translocation through the cell membrane. This force augments the transport velocity of

MNPs, in addition to the gravitational force. The velocity of the particle in the magnetic

field ($U_{mag}$) depends on the volume of the magnetic material ($V_{mag}$), the hydrodynamic radius (r), and the magnetic field gradient (dB/dz) as shown in equation below.

$$U_{mag} = \frac{V_{mag}M}{12\pi\eta r} * \frac{dB}{dz}$$

Here, M is the magnetic field strength and $\eta$ is the viscosity of the cell growth medium. It has been shown that larger MNPs are more easily taken up by cells ([185]–[188]).

However, for efficient steering of MNPs in MDT, they need to be superparamagnetic without possessing remnant magnetization on removal of the steering field [189]. This property requires very small MNPs with a magnetic core diameter of around 20 nm [190]. When using smaller MNPs that need to deliver the payload before being cleared from the body, an additional force can be deployed to enhance transfection into the target cells. This work shows that magnetic fields that are used for guidance in the MDT process have the additional beneficial effect of enhancing cellular uptake of drug conjugated SPIONs.

Although we can clearly observe the cell destruction capability of DOX-MNPs (which implies that DOX molecules are being released from the MNP core which then enter the nucleus, intercalate with the cell DNA, and kill the cell), we have yet to understand the exact mechanism of cellular uptake and drug release mechanism of the DOX-MNPs. The future work with regard to this chapter would definitely include understanding these mechanisms, as well as developing better strategies to improve the release kinetics of the DOX molecules from its nanoparticle form.

# 5. *IN VIVO* STUDIES USING MAGNETIC RESONANCE IMAGING AND HISTOLOGY FOR ASSESSING TISSUE UPTAKE OF MAGNETIC NANOPARTICLES DURING INTRATHECAL MAGNETIC DRUG TARGETING

## 5.1. Summary

The greatest challenge for CNS disease treatment via systemic delivery is not insufficient drug potency, but lack of an effective targeting technique along with the high risk of side effects. The presence of the BBB makes delivery of therapeutic molecules to the brain and spinal cord especially difficult. Our proposed drug delivery technique, termed intrathecal magnetic drug targeting can precisely localize drug molecules to specific sites, while drastically reducing side effects compared to existing therapies. Local drug confinement achieved with intrathecal magnetic drug targeting will greatly decrease systemic toxicity, while delivering high drug concentrations to the desired target location within the CNS. In this chapter, feasibility of the intrathecal magnetic drug targeting technique has been proved using *in vivo* studies conducted in Sprague Dawley rats. In our experiments, we successfully localize intrathecally administered MNPs, synthesized of iron-oxide, at specific levels in the spinal column of the rats. Intrathecal magnetic guidance of therapeutics has substantial advantages for treatment of neurological diseases: (1) It offers the critical advantage of strong magnetic forces being able to steer, concentrate and lock therapeutic agents at the target site, and (2) Because our MNP vehicle utilizes the intrathecal delivery route, therapeutic agents need not cross the blood brain barrier. In addition, virtually no toxic agents can leak back into the systemic circulation.

## 5.2.  Introduction

The multicellular architecture of the CNS makes disease treatment challenging due to heterogeneous cellular sensitivity to drug-targeted therapy ([191], [192]). For effective treatments of neurological disorders, it is paramount to target cells only in specific locations. Targeted delivery of drugs to specific areas of the CNS is currently a formidable challenge for effective treatment of diseases such as glioblastomas, spinal cord tumors and SCI. Dr. Begley from Kings College London states, "*Many potential drugs, which are effective at their site of action, have failed and have been discarded during their development for clinical use due to a failure to deliver them in sufficient quantity to the CNS*" [193].

The main obstacle for CNS drug delivery is the BBB, which consists of a cellular sheath that enclose capillaries restricting passage of therapeutics from the bloodstream to the brain and spinal cord tissue ([194], [195]). Currently, the worldwide interest in nanomedicine research underscores the promise of using nanoparticles for more selective delivery of therapeutics across the BBB to precise locations in the CNS. Novel drug-loaded nanoparticles have been employed to penetrate the BBB, for example, unique nanoparticles coated with specific proteins such as transferrin ([196], [197]), and polymers such as PLGA ([198], [199]), have been synthesized especially for this purpose. However, many such nanoparticle formulations require complex chemical modifications to facilitate loading of drugs and targeting ligands, which may affect drug potency and its pharmacokinetics.

Recently, a more robust approach has been developed with the use of MNPs for targeted delivery of therapeutics ([200], [201]). Lübbe pioneered the use of MNPs for delivering drugs in patients with advanced solid tumors. In a phase-1 clinical trials, epirubicin loaded MNPs were administered systemically and successfully directed to target

tumor tissues. However, organ toxicity was observed at higher administered doses [202].

The potency of utilizing MNP vehicles has also been recognized by industry. For example,

Chemicell GmbH commercializes TargetMag-doxorubicin nanoparticles with a multidomain

magnetite core and cross-linked starch matrix with terminal cations that can be reversibly

exchanged with the positively charged chemotherapeutic - doxorubicin [158]. However,

none of the current MNP formulations can successfully pinpoint large therapeutic

molecules to precise locations in the CNS. Therefore, there is an urgent need for an

innovative drug delivery method to confine high drug concentrations at specific target

regions without dispersing them throughout the entire CNS.

Intrathecal drug delivery is a drug administration technique that bypasses the BBB,

and is indicated for conditions such as leptomeningeal metastases ([203], [204]), spasticity

[205], pain management [206] and spinal anesthesia [207]. During intrathecal delivery,

drugs are administered directly into the CSF contained in the SAS of the CNS. CSF flow

pulsations induce micromixing of CSF and intrathecally injected therapeutics, leading to

their rapid dispersion. Intrathecal administration circumvents the blood brain barrier, but

once injected, drugs often disperse indiscriminately away from the target site. To maximize

the therapeutic effect without excessive risk of toxicity in non-targeted zones, intrathecally

injected drugs should be concentrated at specific target locations. For example, precise

targeting of tumor-infiltrated spinal tissue with chemotherapeutic agents could

significantly improve the prognosis of patients with intramedullary spinal cord tumors

without harmful side effects to the spinal cord, brain or other vital organs ([22], [23]). The

spread of cytotoxic drugs such as chemotherapeutics into non-targeted regions can cause

considerable and often intolerable side effects. The lack of focused drug targeting in IT

administration is currently overcome by using very high drug doses to ensure therapeutic concentrations at target regions. Unfortunately, this method to ensure therapeutic effect also causes higher systemic concentrations and toxicity.

Our group has specialized on magnetic guidance of MNPs in the CNS ([42], [43], [45]). To localize drug molecules in specific target sites within the CNS, we propose a novel magnetic nanoparticle-based delivery technique that we term Intrathecal Magnetic Drug Targeting. It combines traditional intrathecal drug administration with magnetic guidance of therapeutics to target tissues. In this technique, MNPs loaded with drug molecules are directly administered into the CSF and pinpointed at a desired target site using an external magnetic field. Drug-loaded MNPs are rapidly transported throughout the CNS via the pulsatile motion of the CSF while externally placed magnets confine them at specific sites. In our formulation, MNP cores are made of iron and iron-oxide, which are biocompatible and biodegradable. The iron ions are absorbed into the body's iron stores during metabolism and are eventually used for hemoglobin synthesis [208]. Previous uses of MNPs deployed systemic distribution via the bloodstream and were therefore limited in crossing the BBB ([147], [157]). MNPs circulating in the bloodstream may also easily be sequestered in fenestrated capillaries of vital organs of the body; this undesirable diversion diminishes therapeutic efficacy at the target site in addition to causing systemic toxicity. The benefits of the proposed technique are illustrated in Figure 2.

We have used Sprague Dawley rats to demonstrate that MNPs delivered intrathecally can be successfully targeted to specific locations in the spinal column via an external magnetic field.

Our group has previously presented *in vitro* experiments on maximizing collection efficiency of MNPs for IT MDT by testing different placement, field strength and orientation of external magnets (Chapter 2). For this purpose, we created a human surrogate spine model in which we reproduced natural CSF pulsations and performed IT injections with clinically-used catheters [42]. The optimal settings obtained from the *in vitro* experiments for magnet placement, field strength and injection dynamics were used for *in vivo* validation of IT-MDT in rats. In this paper, we use techniques such as MRI and histopathological analysis to demonstrate that MNPs injected into the intrathecal space are capable of precisely localizing at a specific spinal level via an external surface magnet. Our data demonstrates that we can effectively deliver a significant portion of the MNPs to any specific level of the spinal cord. In this chapter, we demonstrate that targeted delivery of nanoparticles to a spinal level is possible in an *in vivo* model.

### 5.3. Materials and Methods

### 5.3.1. Synthesis of Gold Coated Magnetite Nanoparticles (Fe$_3$O$_4$@Au nanoparticle)

The drug delivery platform we used was gold coated magnetite nanoparticles which were synthesized by a simple co-precipitation technique as described in Mandal and colleagues in 2005 [110]. Our group has also previously published our modified technique in Lueshen and colleagues (2014) [42], and a description has been provided in Appendix Section A.

### 5.3.2. IT-MDT experiments in Sprague Dawley rats

8-week old Sprague Dawley rats were used for the intrathecal MNP infusion experiments. All animal experiments were approved by the Animal Care and Use Committee at the UIC. Animals were anesthetized by inhalation of isoflurane. The surgical

table was equipped with stereotaxis equipment and a nose cone to allow for administration of gaseous isoflurane during surgery. Once anesthetized, the hair on the back of the animal was shaved using hair trimmers. A 30G needle was advanced between the L4 and L5 vertebrae, and 20 μL of 17 mg/mL solution of the MNPs was injected into the CSF of the spinal SAS. From the initial injection position, the needle is retracted slightly so that the MNP injection does not occur directly into the spinal tissue but within the CSF-filled spaces. The initial pial position from which we retract can be observed by the tail flick. After the IT injection, a small neodymium-iron-boron magnet (0.01 Tesla) was placed externally on the back of the rat in the mid-upper thoracic region (T9-T1). The target magnet served the purpose of arresting the MNPs at the desired spinal level and remained in position on the animal's back for various time intervals – 1 hour, 3 hours and 6 hours. Rats were kept under the influence of anesthesia using a nose cone delivering isoflurane gas for the entire duration of the IT-MDT experiment. At the end of the experiment, the animals were euthanized via perfusion fixation (details given below). Animals were then imaged using a 9.4 Tesla MR scanner available at the Nuclear Magnetic Resonance Laboratory at the UIC. After imaging, spinal cords of the animals were removed for histological analysis.

### 5.3.3. Perfusion fixation of Sprague Dawley rats

Anesthesia was administered via an intraperitoneal (IP) injection of ketamine (100 mg/kg) and xylazine (5 mg/kg). The depth of anesthesia after IP injection of ketamine/xylazine (0.2 mL/100 g body weight) was determined using the toe-pinch method. Animal was placed ventrodorsal in a shallow tray and its fur was swabbed with 70% isopropanol. A skin incision was longitudinally from middle of the abdomen up to the throat. A 5-6 cm lateral incision was then made through the abdominal wall below the

ribcage. The lungs were carefully displaced, and a cut was made on both sides through the

ribcage to the collarbone. The sternum was lifted, turned upwards towards the animal's

head and clamped with a hemostat to keep it in place. A blunt 18G needle connected to a

perfusion apparatus was inserted into the left ventricle, and slowly pushed into the aorta. A

large outlet was made by incision in the right atrium. The animal was first perfused with

200 mL of phosphate buffered saline (pH 7.4, 37ºC) at a pressure of 80mmHg, after which

400 mL of the fixative (4% paraformaldehyde solution) was perfused.

### 5.3.4.  MR imaging of the Sprague Dawley rats

After euthanasia, the animals were immediately taken to the MR scanner for

T2-weighted imaging to assess localization of MNPs in the rat intrathecal space. The

parameters used for imaging were as follows: fast spin echo images were obtained with a

time of echo (TE) of 102 milliseconds, a time of repetition of 5300 milliseconds, echo train

length of 8, receiver bandwidth of 31.25 kHz, image field of view of 12 cm, slice thickness of

5 mm, matrix size 512 by 512, and number of excitation of 2. An MRI fiducial was placed at

the position of external magnet placement for imaging, as the magnet had to be removed

before the animal could go into the MR scanner.

### 5.3.5.  Removal of spinal cord and histological analysis of spinal cord tissue

The spinal cords were excised for histological analysis of the MNPs in the tissue. The

rat spinal cord was removed using a whole-spine laminectomy. The lamina of every

vertebra along the animal spine was removed using a sharp pair of scissors, after which the

bone was thinned down until slight CSF leakage was observed. The dura was removed

using tweezers, and the spine was gently extracted and fixed in paraffin. Regions of the

spinal cord corresponding to the injection site, targeting magnet, cervical spine and brain

parenchyma were selected from which sequential tissue slices (axial sections of thickness = 1mm) were obtained. The slices were stained using prussian blue solution (20% hydrochloric acid and 10% potassium ferrocyanide) for 20 minutes, after which they were washed 3 times using distilled water. The slices were then counter stained using 0.1% nuclear fast red solution for 5 minutes after which they were washed twice in distilled water. After staining, the slices were dehydrated, washed twice with alcohol, and placed in xylene. They were then mounted on a microscope slide in mounting medium dissolved in xylene, for imaging using a light microscope. A coverslip was placed on top of the slice on the microscope slide and evaporation of xylene around the edges of the coverslip dries up the mounting medium, bonding it firmly to the slide.

### 5.3.6. Quantification of MNP localization and tissue penetration

MNP distribution in spinal pia and parenchyma in various regions of the spinal cord were analyzed semi-quantitatively using *ImageJ* software (NIH). Prussian Blue stain delineated areas containing MNPs in the tissue slices, which were effectively measured using *ImageJ* software.

### 5.4. Results

### 5.4.1. Synthesis and Characterization

The gold-coated magnetite nanoparticles were synthesized and characterized as mentioned in the Appendix Section A, as well as in previous chapters of this dissertation.

### 5.4.2. MRI to confirm MNP localization in IT-MDT experiments

We performed intrathecal injection of MNPs under magnetic guidance. MR Imaging was used to visualize MNP distribution in the CSF throughout the spinal cord. Because iron core enhance proton relaxation of specific tissues, regions covered by MNPs are visible in

MR images [74], [209]. Our iron oxide nanoparticles provide a negative contrast in T2-weighted images, decreasing MR signal intensity. They consequently produce hypointense signals, making the affected regions appear darker compared to rest of the image. Therefore, we could detect MNP accumulation at a specific spinal level within the intrathecal space.

A total of 12 animals (N=12) were used for the MRI experiments. 3 animals served as control (intrathecal saline injection), 3 animals each were subjected to 1 hour, 3 hours and 6 hours of IT-MDT experiments. A T2-MR image of a control animal (Rat A) is shown for reference. MR images of Rat B-Rat D demonstrate MNP localization near the magnet as depicted in sagittal views in Figure 39a, and corresponding axial views in Figure 39b. As time progressed, MNPs accumulated in the target site. The amount and progression of the MNP accumulation was determined semi-quantitatively with image analysis.

*ImageJ* software was used to measure pixel intensity in a region of interest (yellow ellipse). The hypointense signal in the target site, X, was compared to the area-integrated pixel intensity in the original control image, Y. MNP localization was quantified by using the following equation –

$$\text{MNP pixel intensity (\%)} = \frac{X - Y}{Y} \times 100$$

where, $X$ = Pixel intensity in target magnet region (1 hour, 3 hours, 6 hours after infusion)

$Y$ = Pixel intensity at target magnet region in control image

The MNP pixel intensity change after 1 hour, 3 hours and 6 hours is shown in the bar graph of Figure 39c.

Figure 3: MNP localization after IT-MDT injection. Control is shown in first column; columns- 2 to 4 depict T2-MR images after 1, 3 and 6 hours with sagittal views in top row (a), corresponding axial views in bottom row (b). Magnet placement is indicated with MRI fiducial marked as red dotted box; the area of MNP localization close to the magnet is delineated by yellow dotted ellipse. (c) Semi-quantitative analysis with *ImageJ* was used to determine amount and progression of MNP localization by quantifying pixel intensity at targeting site (yellow ellipse). The bar chart of pixel intensities indicates that longer magnet placement increases MNP accumulation at the target site.

### 5.4.3. Histological analysis of the rat spinal cord to confirm localization and penetration of MNPs in IT-MDT experiments

We varied the time duration of placement of the external magnet on the back of the animal (1, 3 and 6 hours) before euthanasia, to observe any differences in the spinal tissue MNP uptake. 12 animals were used in total for these experiments - 3 animals were used as control (saline injection), and 3 animals each were used for 1 hour, 3 hours and 6 hours of IT-MDT experiments. As can be seen in Figure 40, localization of MNPs in our IT-MDT experiments can be visually observed in the spinal cords after they have been removed from the rats post-euthanasia. Sequential serial axial sections were
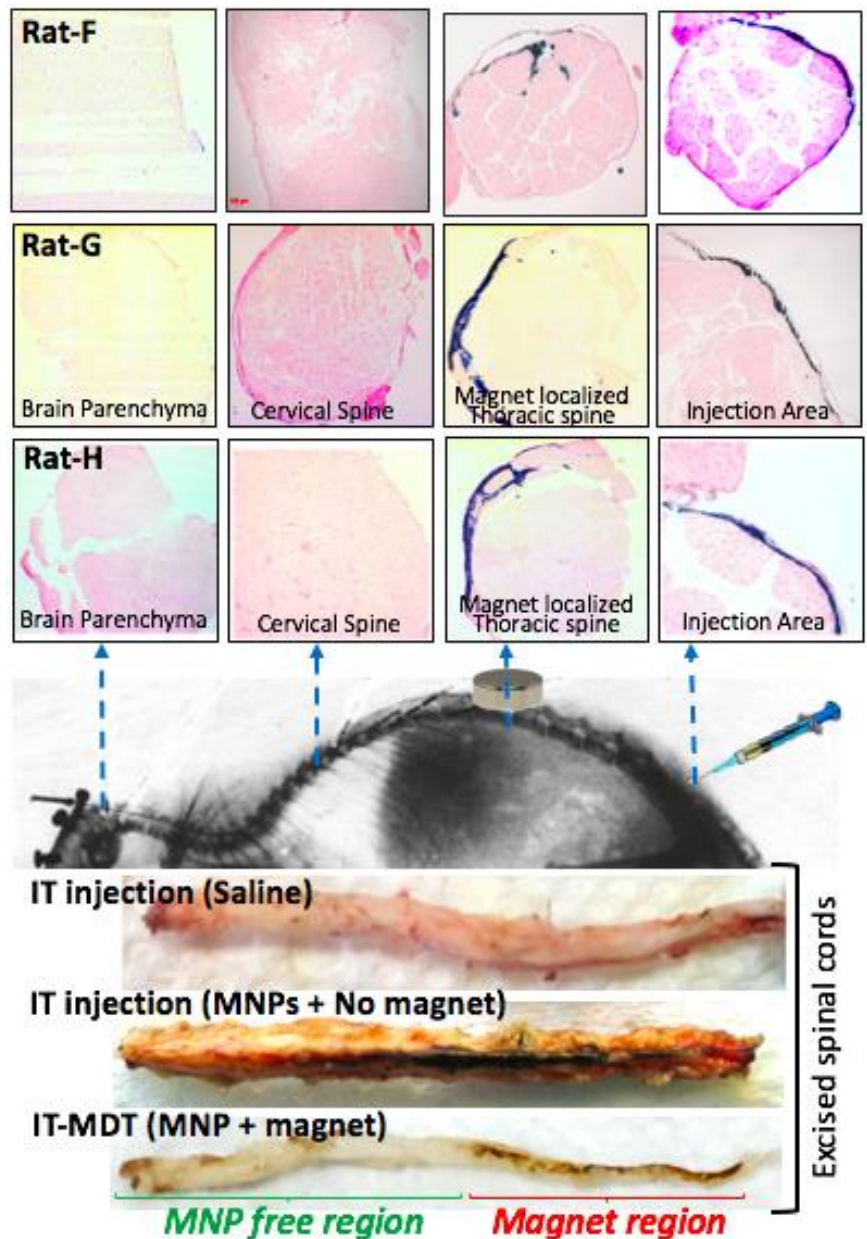


Figure 40. Histological assessment of magnetically guided nanoparticle localization in two rat experiments after IT injection for 6 hours. (top) Tissue sections were obtained from the injection site, thoracic spine (where target magnet was placed), cervical spine, and brain parenchyma. Prussian blue showed MNP localization in the thoracic target site. (bottom) Entire spinal cords excised after IT infusion with saline, and MNPs with and without magnetic guidance, show successful localization only when a magnet is used. IT infusion of MNPs under magnetic guidance localizes them at a desired site.

89

obtained at the sites of the targeting magnet (thoracic spine), cervical spine, brain tissue, and MNP injection site. The sections were then analyzed using histology to confirm localization and penetration of MNPs along the spine.

To quantify the tissue MNP uptake, the prussian blue stained regions in the processed 2D tissue slices were quantified using *ImageJ* as mentioned in the methods section. This quantification helped differentiate between the distribution of MNPs in the spine pia and parenchyma at the injection and targeting sites of the spine (Figure 41c1 and
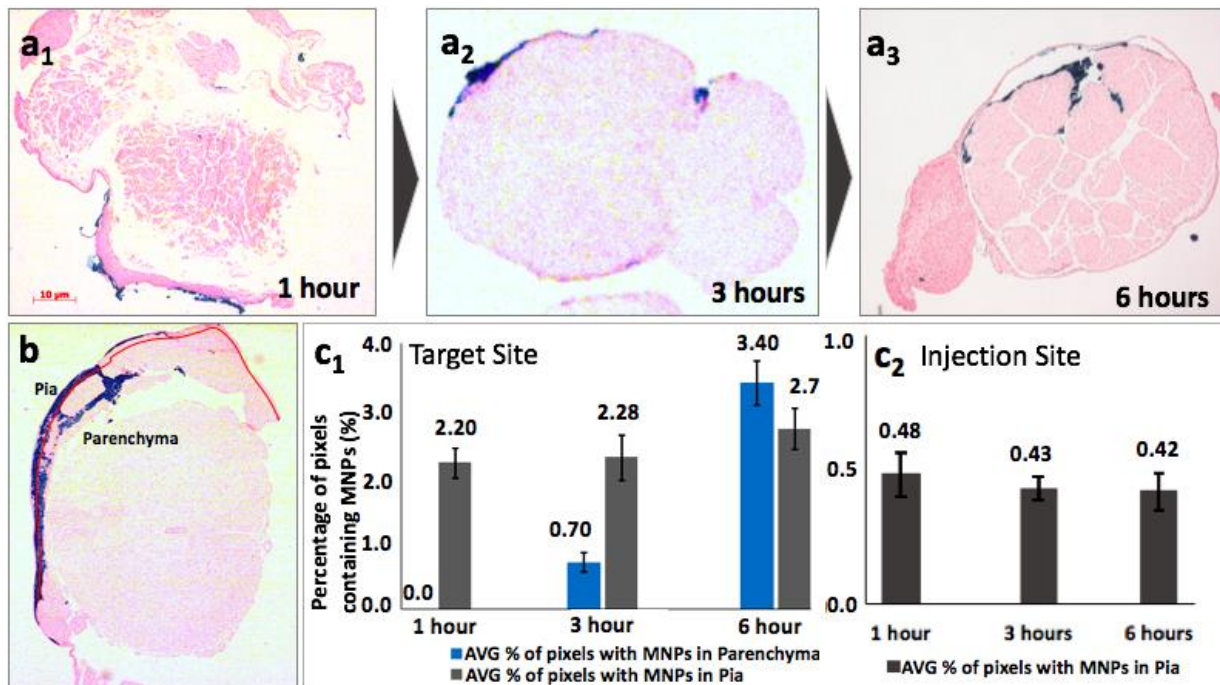


Figure 41. Histological analysis of the spinal cord tissue to assess MNP penetration across the spinal pia and parenchyma (a) Prussian blue staining results of rat spinal cord tissue sections obtained from IT-MDT experiments (duration = 1h, 3h and 6h). The tissue slices were taken at the region corresponding to external magnetic field placement. Deeper MNP tissue penetration was achieved by prolonging magnet application. (b) Image showing how the pia and parenchyma were distinguished (red line) a spinal cord tissue slice. (c) ImageJ analysis quantifies MNP localization in the pia and parenchyma, and confirms almost three-fold increase in tissue uptake after 6h compared to 1h of magnet application. (c1) Tabulated ImageJ analysis indicating % of pixels in the image with MNPs (corresponding to Prussian blue stained regions) in the pia and parenchyma regions of the tissue slices at the index level (external magnet localization) in the 1,3 and 6h IT-MDT experiments. (c2) ImageJ analysis indicating % of pixels in the image with MNPs (Prussian blue stained regions) in the pia region of the tissue slices from the MNP injection site in the 1,3 and 6h IT-MDT experiments. At the injection site, our analysis consistently shows only small MNP amounts compared to the target site.

34c2). A relatively small amount of pial MNP uptake was observed at the injection site in all the IT-MDT experiments (Figure 41c2). Both pial and parenchymal penetration of MNPs was observed in tissue slices corresponding to the targeting magnet region, whereas only pia uptake was observed in the tissue slices corresponding to the injection site in all the IT-MDT experiments. No MNP uptake was observed in the spinal cord tissue sections proximal to the targeting magnet.
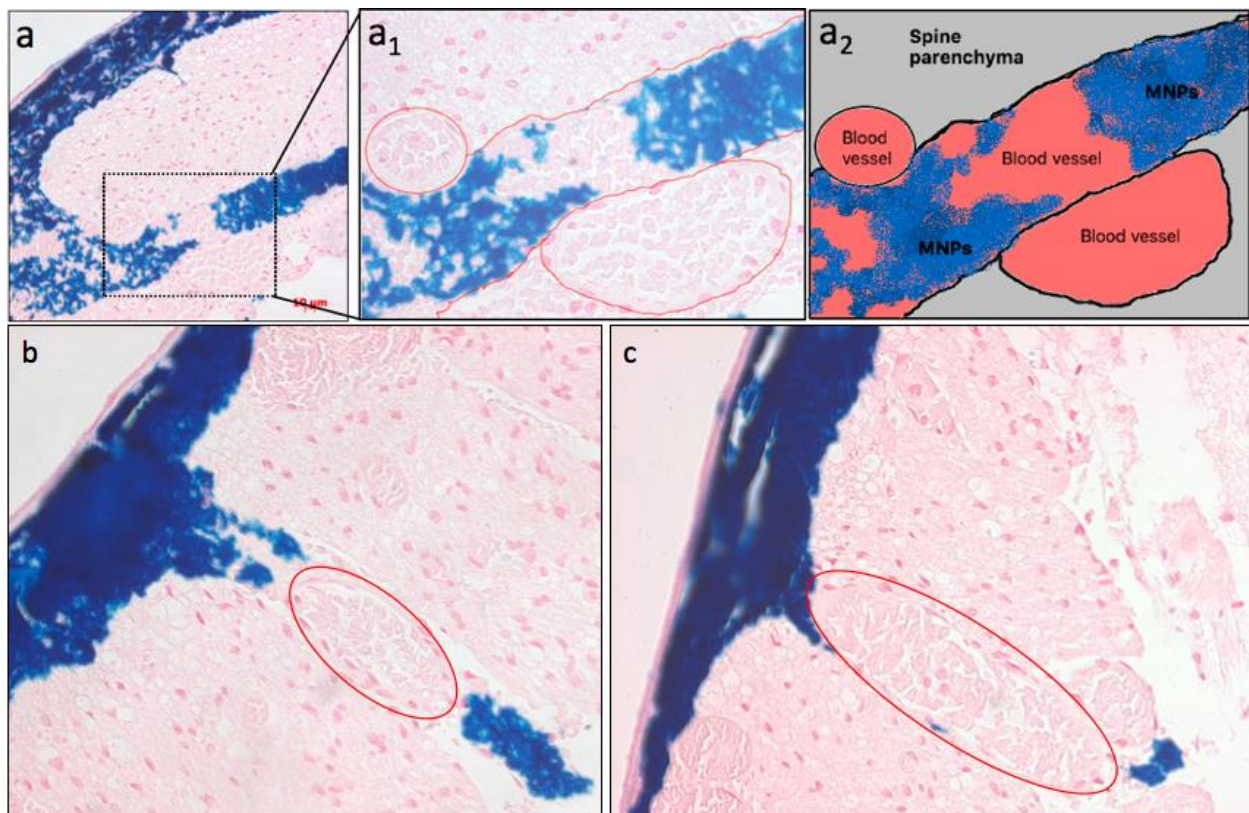


Figure 42. MNP penetration was tracked along perivascular spaces with H&E staining (cell bodies pink, MNPs-dark blue). (a) The processed tissue slice shows presence of blood vessels in the regions of deeper MNP tissue penetration. View with magnification elucidates that the observed MNP penetration into the spinal tissue occurs along perivascular spaces of penetrating blood vessels. Schematic-redrawn from the magnified image for clarity- traces conceptually the boundaries of the blood vessels and MNP perivascular colocalization (blood vessels are marked in red). (b)(c) Other tissue sections showing presence of blood vessels (marked in red) in the regions of MNP penetration.

Further histological analysis using Hematoxylin and Eosin (H&E) stain, along with Prussian blue staining, clearly indicated presence of blood vessels close to the region of deeper MNP penetration as shown in Figure 42. Eosin is a negatively-charged acidic dye, which stains basic (or acidophilic) structures – such as cytoplasmic proteins – red or pink. Hematoxylin is used to stain acidic (or basophilic) structures – such as the cell nucleus – a purplish blue. During the histological analysis of our spinal cord tissue sections, the H&E stain helped distinguish between endothelial cells (that contain a nucleus) and red blood cells (which do not contain a nucleus). The blood vessels in our tissue sections could be clearly identified - as the blood vessel wall contains endothelial cells, whereas the interior of the vessel contains red blood cells (Figure 42a).

## 5.5.  Discussion

We propose a novel administration technique harnessing strong magnetic fields to precisely localize therapeutics at targeted regions in the spinal cord. The ability to localize therapeutics at target tissues without further distribution away from the target site make it an appealing technique for novel, site-specific targeted drug delivery for many neurological disorders. The proposed IT-MDT technique is a novel strategy with the following advantages:

- The MNP drug conjugates do not have to traverse the BBB.
- The MNPs can be administered in high doses directly into the CSF and localized in any focal region of interest by externally placed magnets.
- Concentration of cytotoxic agents, such as chemotherapeutics, can be raised to effective levels in the CNS without systemic recirculation by conjugating them to an

MNP platform. This allows for high *local* chemotherapeutic dosages without significant dispersion into susceptible organs such as the heart or the kidney.

- The MNP concentrated in focal regions are visible using MRI, so that the extent of the MNP distribution and accumulation can be assessed.

Our laboratory has developed a superparamagnetic drug delivery platform, which can be used to steer pharmacologically active drugs to specific locations in the CNS. The gold-coated magnetite nanoparticle platform that we have developed has three carefully optimized properties for magnetic steering: (i) a superparamagnetic iron-oxide core for high magnetic susceptibility, (ii) a gold shell enabling conjugation of drug molecules via thiol bonding, and (iii) ability to track particle biodistribution *in vivo*. As mentioned in previous chapters, drug molecules can easily be loaded on the surface of the outer gold shell of our nanoparticles using thiol bonds or chemisorption. In our drug delivery platform, the active agents do not have to be chemically altered to cross the BBB.

We have demonstrated that we can successfully guide and localize MNPs at a specific site along the spinal cord using an external magnetic field. Iron oxide nanoparticles are already Federal Drug Administration (FDA) -approved for clinical use as MRI tracers to identify CSF leakage through the dura or other injuries ([210], [211]). We therefore take advantage of our iron oxide nanoparticles for exploiting this property to track MNPs and measure their localization at the target magnet site. *ImageJ* was also used to semi quantitatively confirmed the MNP localization in our MR experiments. The analysis indicated an increase in MNP localization with increased duration of magnet placement. Our histology results confirmed our observations from the MRI experiments, showing effective localization of MNPs near the target tissue (thoracic region), and virtually no

particle dispersion beyond the magnet into the cervical spine and brain. Axial slices of the

spinal cord stained using Prussian blue stain were analyzed with *ImageJ* software to

quantify MNP uptake within the tissue (area covered by the MNPs compared to the area of

whole tissue slice). *ImageJ* was used to delineate MNP distribution in specific regions of

tissue - spinal pia and parenchyma. In our 3 and 6-hour IT-MDT experiments, MNPs

crossed the pial layer and entered the spinal parenchyma at the site of magnet placement.

Our preliminary histology results are not conclusive but indicate that longer application of

an external magnetic field may produce deep tissue penetration as a large local

concentration of MNPs enhance penetration into the spinal tissue when compared to dilute

MNP solutions. Treatment of diseases such as intramedullary spinal cord tumors require

parenchymal penetration of drug molecules, and our results are promising for developing

treatments for such diseases. We have not performed any surface modification of our MNPs

to enhance spinal tissue penetration. A future step could include adding a layer of

poly(ethylene glycol) or PEG to the MNP surface to increase penetration of the drug vehicle

into deeper tissue regions. PEGylation has shown to increase tissue penetration of

nanoparticles in the CNS [212].

An interesting finding which was observed during histological analysis using H&E

stains was the path taken by the MNPs to travel deeper into the tissue. We followed deep

penetration paths and found that MNPs colocalized with perivascular spaces (Figure 42).

Taken together, our preliminary results demonstrate that the MNPs can penetrate into the

tissue by two routes, diffusion through the extracellular matrix, and preferred access

through perivascular spaces of the penetrating arteries (Virchow Robinson spaces). The

Nedergaard lab has also recently showed preferred transport of tracers via the

perivascular routes after cisternal injection [213]. Our results are encouraging because they demonstrate that our MNPs can penetrate the spinal parenchyma via an interstitial as well as a separate perivascular route for carrying drugs into spinal tissue.

## 6. CONCLUSIONS AND FUTURE WORK

### 6.1.  Summary

Delivering therapeutics to specific targeted sites in the CNS is currently a formidable challenge in the treatment of neurological disorders. This dissertation focused on a novel drug delivery technique called intrathecal magnetic drug targeting, or IT-MDT, which overcomes some of the severe limitations in current delivery techniques for the CNS. In brief, drug-loaded magnetic nanoparticles are administerd intrathecally into the CSF, and localized at specific CNS locations using an external magnetic field. *In vitro* bench-top and cell-based experiments, as well as *in vivo* experiments on rats were conducted to prove the feasibility of this technique. Computational simulations of permanent magnets were performed using COMSOL® and MATLAB® programs to assess the strength of magnetic field required at targeted regions of the CNS for adequate MNP collection to produce therapeutic efficacy. A mathematical model was developed to determine MNP accumulation at specific target sites in the CNS while under the influence of a magnetic field. The IT-MDT method was also improved by testing the use of magnetizable implants to build steeper magnetic gradients at target sites for increasing efficacy of the technique.

The overall goal of this research was to engineer a new treatment method for patients suffering from neurodegenerative disorders such as brain tumors, spasticity, chronic pain, and many others. In this final chapter, the significance and contributions of this IT-MDT research are outlined followed by a description of future work.

### 6.2  Contributions of this dissertation

Building off of the concept of magnetic drug targeting, the technique of IT-MDT was developed to maximize therapeutic effect of CNS drugs without causing systemic toxicity.

***In vitro IT-MDT experiments.*** The *in vitro* work has been described in detail in the

Appendix Section A. Superparamagnetic nanoparticles, composed of a magnetite core and a

gold shell, were synthesized. An *in vitro* model was built which was anatomically and

physiologically consistent with the human spine. IT-MDT expeiments were conducted on

this bench-top model, in which parameters such as magnetic field strength, duration of

magnetic field exposure, and distance between the target location and injection site, were

varied. Simulations were performed to study magnetic fields produced by permanent

magnets. Data from these experiments were used to optimize injection and targeting

parameters, as well as for designing appropriate magnetic fields for use in IT-MDT

experiments. Our experimental results showed that external magnets can guide and

localize intrathecally injected drug-loaded MNPs to specific diseased sites within the CSF

space throughout the CNS, while achieving large MNP collection efficiencies at target sites.

The data implied that very high drug concentration levels can be achieved at any specific

location, which is almost nine-times the therapeutic levels obtained in compared to regular

intrathecal administration. Using magnetizable implants, further produces a 20% increase

in collection efficiency of MNPs at specific sites.

***Quantum dot loaded MNPs as a drug deivery vehicle for IT-MDT.*** Fluorescent

QD-loaded MNPs were synthesized using thiol-gold chemistry. The gold shell of the

superparamagnetic nanoparticles is an extremely useful platform for loading drugs

containing a free sulfur group, due to the matural attraction of the sulfur atoms and gold

surfaces. Utilizing this unique property, mercaptopropionic acid-coated CdTe QDs were

loaded on the surface of our gold-coated superparamagnetic nanoparticles. The

development of these nanocomposites served two purposes– (1) It resulted in a drug

delivery platform for MDT, especially for drugs containing a sulfur bond and (2) It was used for proving the feasibility of the IT-MDT technique in an *in vivo* model, for which these nanocomposites were intrathecally injected into the CSF space of a rat, and targeted to specific locations in the CNS using an external magnet. Fluorescence molecular tomography (IVIS® imaging) was the main techique used for the real-time visualization of the movement of these nanocomposites.

**DOX-loaded MNP vehicle for tumor treatment.** The tumor drug doxorubicin (commercially known as Adriamycin®) was loaded on the surface of the MNPs using a biocompatible polymer gellan gum to develop a nanoparticle for IT-MDT based treatment of tumors in the CNS. As these nanoparticles will be used for IT-MDT, the influence of magnetic fields on the cellular uptake of MNPs was also determined. Confocal microscopy, flow cytometry and MTT assays were used to confirm that the magnetic fields enhanced the tumor cell uptake of these nanoparticles by about 6-18%, depending on the field strength of the magnet used and time of magnet application. Therefore, magnetic fields used for IT-MDT treatment of neurological disorders would not only localize the drug-loaded MNPs to a taget site resulting in higher theapeutic concentrations and lower administered dosages, but would also have an added advantage of increased cellular uptake which, in turn, enhances the drug uptake by the diseased cells.

**In vivo studies using MRI and histology for assessing tissue uptake of MNPs during IT-MDT.** Although our fluorescence molecular tomography studies using QD-nanocomposites indicated that external magnetic fields were successful in targeting MNPs at specific sites in the CNS after intrathecal administration, it was essential to confirm tissue uptake of MNPs after localization. MRI and histology provided

semi-quantitative and quantitative analysis of the MNP localization and tissue uptake

respectively. Analysis of both MRI and histology experiments confirmed the results

obtained in the *in vitro* experiments which indicated that increasing duration of magnet

application increased MNP localization. Semi-quantitative analysis using MRI indicated that

a 10% increase in collection efficiency of MNPs was achieved when the time of magnet

application was increased from 3 hours to 6 hours. Quantitative analysis of stained spinal

cord tissue slices using Image J software at the target site of MNP localization showed a

3.13% increase in tissue uptake from 3 hours to 6 hours of magnet field placement. The

difference in results between MRI and histology experiments is due to the fact that

histology is a far more accurate technique for quantitative analysis, when compared to MRI.

It also refers to the actual tissue uptake rather than the MNP collection at the site. The two

major routes of transport of MNPs in the spinal tissue were also established, which were

via extracellular spaces and perivascular spaces surrounding major arteries in the spinal

cord tissue.

   ***Computational modeling of magnetic fields generated from permanent magnets***

***and development of a mathematical model for accumulation of MNPs during IT-MDT.***

In this chapter, the theory behind generation of magnetic fields from both electric fields

and permanent magnets was explained, and related equations were described in detail.

Based on the equations, MATLAB program codes were written to generate magnetic fields

in both 2D and 3D spaces. These codes can be included as user-defined functions in

computational fluid dynamics software such as ANSYS fluent for simulating MNP collection

in the CNS due to external magnets. A mathematical model for predicting collection of

MNPs under the influence of pulsating CSF and external magnetic fields was also provided.

## 6.3    Future work

The feasibility and efficacy of IT-MDT has been proven using both *in vitro* and *in vivo* experiments. The positive effect of magetic fields on the cellular uptake of the MNPs was also demonstrated. A tumor drug (doxorubicin) loaded MNP was also  synthesized and its effectiveness was tested on cancer (glioma) cells. A next step would be to generate a spinal cord tumor model in an animal (rat or rabbit) and use the doxorubicin loaded MNPs for its IT-MDT-based treatment, showing a clear improvement in life expectancy and quality of life when compared to regular systemic or intrathecal administration of doxorubicin. For computational purposes, the MATLAB code in this dissertation needs to be incorporated into a CFD software for accurate simulation of IT-MDT in the human CNS. A 3D mesh of the human CSF space comprising of 0.5 million elements has already been generated by the Linninger Research group, which can be used for this purpose.

# CITED LITERATURE

[1] W. Eck *et al.*, "PEGylated gold nanoparticles conjugated to monoclonal F19 antibodies as targeted labeling agents for human pancreatic carcinoma tissue," *ACS Nano*, vol. 2, no. 11, pp. 2263–2272, Nov. 2008.

[2] P. K. Jain, K. S. Lee, I. H. El-Sayed, and M. A. El-Sayed, "Calculated absorption and scattering properties of gold nanoparticles of different size, shape, and composition: applications in biological imaging and biomedicine," *J. Phys. Chem. B*, vol. 110, no. 14, pp. 7238–7248, Apr. 2006.

[3] C. X. Jin Xie, "Controlled PEGylation of Monodisperse Fe3O4 Nanoparticles for Reduced Non-Specific Uptake by Macrophage Cells," *Adv. Mater.*, vol. 19, no. 20, pp. 3163–3166, 2007.

[4] P. Gangopadhyay, S. Gallet, E. Franz, A. Persoons, and T. Verbiest, "Novel superparamagnetic Core(Shell) nanoparticles for magnetic targeted drug delivery and hyperthermia treatment," *IEEE Trans. Magn.*, vol. 41, no. 10, pp. 4194–4196, Oct. 2005.

[5] I. P. Kaur, R. Bhandari, S. Bhandari, and V. Kakkar, "Potential of solid lipid nanoparticles in brain targeting," *J. Control. Release Off. J. Control. Release Soc.*, vol. 127, no. 2, pp. 97–109, Apr. 2008.

[6] M. T. K. Ryuta Saito, "Gadolinium-loaded liposomes allow for real-time magnetic resonance imaging of convection-enhaced delivery in the primate brain," *Exp. Neurol.*, vol. 196, no. 2, pp. 381–9, 2006.

[7] T. Inoue *et al.*, "Therapeutic efficacy of a polymeric micellar doxorubicin infused by convection-enhanced delivery against intracranial 9L brain tumor models," *Neuro-Oncol.*, vol. 11, no. 2, pp. 151–157, Apr. 2009.

[8] J. Ren *et al.*, "The targeted delivery of anticancer drugs to brain glioma by PEGylated oxidized multi-walled carbon nanotubes modified with angiopep-2," *Biomaterials*, vol. 33, no. 11, pp. 3324–3333, Apr. 2012.

[9] R. G. Thorne and C. Nicholson, "In vivo diffusion analysis with quantum dots and dextrans predicts the width of brain extracellular space," *Proc. Natl. Acad. Sci. U. S. A.*, vol. 103, no. 14, pp. 5567–5572, Apr. 2006.

[10] H. Yan *et al.*, "Imaging brain tumor by dendrimer-based optical/paramagnetic nanoprobe across the blood-brain barrier," *Chem. Commun.*, vol. 47, no. 28, p. 8130, 2011.

[11] E. A. Nance *et al.*, "A dense poly(ethylene glycol) coating improves penetration of large polymeric nanoparticles within brain tissue," *Sci. Transl. Med.*, vol. 4, no. 149, p. 149ra119, Aug. 2012.

[12] M. F. Kircher *et al.*, "A brain tumor molecular imaging strategy using a new triple-modality MRI-photoacoustic-Raman nanoparticle," *Nat. Med.*, vol. 18, no. 5, pp. 829–834, May 2012.

[13] M. Wankhede, A. Bouras, M. Kaluzova, and C. G. Hadjipanayis, "Magnetic nanoparticles: an emerging technology for malignant brain tumor imaging and therapy," *Expert Rev. Clin. Pharmacol.*, vol. 5, no. 2, pp. 173–186, Mar. 2012.

[14] B. Petri *et al.*, "Chemotherapy of brain tumour using doxorubicin bound to surfactant-coated poly(butyl cyanoacrylate) nanoparticles: revisiting the role of surfactants," *J. Control. Release Off. J. Control. Release Soc.*, vol. 117, no. 1, pp. 51–58, Jan. 2007.

[15] S. C. J. Steiniger *et al.*, "Chemotherapy of glioblastoma in rats using doxorubicin-loaded nanoparticles," *Int. J. Cancer J. Int. Cancer*, vol. 109, no. 5, pp. 759–767, May 2004.

[16] A. E. Gulyaev, S. E. Gelperina, I. N. Skidan, A. S. Antropov, G. Y. Kivman, and J. Kreuter, "Significant transport of doxorubicin into the brain with polysorbate 80-coated nanoparticles," *Pharm. Res.*, vol. 16, no. 10, pp. 1564–1569, Oct. 1999.

[17] A. C. Silva *et al.*, "Application of hyperthermia induced by superparamagnetic iron oxide nanoparticles in glioma treatment," *Int. J. Nanomedicine*, vol. 6, pp. 591–603, 2011.

[18] A. Jordan, R. Scholz, P. Wust, H. Fähling, and R. Felix, "Magnetic fluid hyperthermia (MFH): Cancer treatment with AC magnetic field induced excitation of biocompatible superparamagnetic nanoparticles," *J. Magn. Magn. Mater.*, vol. 201, no. 1–3, pp. 413–419, Jul. 1999.

[19] K. J. Widder, A. E. Senyei, and D. G. Scarpelli, "Magnetic Microspheres: A Model System for Site Specific Drug Delivery in Vivo," *Exp. Biol. Med.*, vol. 158, no. 2, pp. 141–146, Jun. 1978.

[20] K. J. Widder, A. E. Senyei, and D. F. Ranney, "Magnetically responsive microspheres and other carriers for the biophysical targeting of antitumor agents," *Adv. Pharmacol. Chemother.*, vol. 16, pp. 213–271, 1979.

[21] B. Chertok *et al.*, "Iron oxide nanoparticles as a drug delivery vehicle for MRI monitored magnetic targeting of brain tumors," *Biomaterials*, vol. 29, no. 4, pp. 487–496, Feb. 2008.

[22] B. Chertok, A. E. David, and V. C. Yang, "Polyethyleneimine-modified iron oxide nanoparticles for brain tumor drug delivery using magnetic targeting and intra-carotid administration," *Biomaterials*, vol. 31, no. 24, pp. 6317–6324, Aug. 2010.

[23] M. Arruebo, R. Fernández-Pacheco, M. R. Ibarra, and J. Santamaría, "Magnetic nanoparticles for drug delivery," *Nano Today*, vol. 2, no. 3, pp. 22–32, Jun. 2007.

[24] P. K. Menon, D. F. Muresanu, and A. Sharma, "Functionalized Magnetic Iron Oxide Nanoparticles Influence Spinal Cord Trauma-Induced Pathology: Neuroprotective Effects of Cerebrolysin Treatment.," *Cell Transplant.*, vol. 22, no. 5, 2013.

[25] J. S. Kim *et al.*, "Toxicity and Tissue Distribution of Magnetic Nanoparticles in Mice," *Toxicol. Sci.*, vol. 89, no. 1, pp. 338–347, Jan. 2006.

[26] Z. Sun *et al.*, "Characterization of cellular uptake and toxicity of aminosilane-coated iron oxide nanoparticles with different charges in central nervous system-relevant cell culture models," *Int. J. Nanomedicine*, vol. 8, pp. 961–970, 2013.

[27] R. Fernández-Pacheco *et al.*, "Magnetic nanoparticles for local drug delivery using magnetic implants," *J. Magn. Magn. Mater.*, vol. 311, no. 1, pp. 318–322, Apr. 2007.

[28] S. Jain, A. Pal, T. C. Nag, and R. Mathur, "Neuroregeneration and functional recovery by magnetic field stimulation and iron oxide nanoparticles in rats with spinal cord transection," *Brain Stimul. Basic Transl. Clin. Res. Neuromodulation*, vol. 8, no. 2, p. 328, Mar. 2015.

[29] A. Pal, A. Singh, T. C. Nag, P. Chattopadhyay, R. Mathur, and S. Jain, "Iron oxide nanoparticles and magnetic field exposure promote functional recovery by attenuating free radical-induced damage in rats with spinal cord transection," *Int. J. Nanomedicine*, vol. 8, pp. 2259–2272, 2013.

[30] P. L. Zadnik *et al.*, "Characterization of intratumor magnetic nanoparticle distribution and heating in a rat model of metastatic spine disease," *J. Neurosurg. Spine*, vol. 20, no. 6, pp. 740–750, Apr. 2014.

[31] M. L. Groves, P. L. Zadnik, and R. Sarabia-Estrada, "Theranostic Nanoparticle-Mediated Tumor Ablation in a Rat Model of Metastatic Spine Disease.'," Johns Hopkins School of Medicine.

[32] R. Weissleder, A. Bogdanov, E. A. Neuwelt, and M. Papisov, "Long-circulating iron oxides for MR imaging," *Adv. Drug Deliv. Rev.*, vol. 16, no. 2–3, pp. 321–334, Sep. 1995.

[33] Y.-X. J. Wang, S. M. Hussain, and G. P. Krestin, "Superparamagnetic iron oxide contrast agents: physicochemical characteristics and applications in MR imaging," *Eur. Radiol.*, vol. 11, no. 11, pp. 2319–2331, May 2001.

[34] B. Bonnemain, "Superparamagnetic agents in magnetic resonance imaging: physicochemical characteristics and clinical applications. A review," *J. Drug Target.*, vol. 6, no. 3, pp. 167–174, 1998.

[35] P. Jendelova, V. Herynek, L. Urdikova, and K. Glogarova, "Magnetic resonance tracking of transplanted bone marrow and embryonic stem cells labeled by iron oxide nanoparticles in rat brain and spinal cord," *J. Neurosci. Res.*, vol. 76, pp. 232–243, 2004.

[36] F. H. Wang *et al.*, "Magnetic resonance tracking of nanoparticle labelled neural stem cells in a rat's spinal cord," *Nanotechnology*, vol. 17, no. 8, p. 1911, 2006.

[37] S.-L. Hu *et al.*, "In vitro labeling of human umbilical cord mesenchymal stem cells with superparamagnetic iron oxide nanoparticles," *J. Cell. Biochem.*, vol. 108, no. 2, pp. 529–535, Oct. 2009.

[38] C.-C. Yang, Y.-H. Shih, M.-H. Ko, S.-Y. Hsu, H. Cheng, and Y.-S. Fu, "Transplantation of Human Umbilical Mesenchymal Stem Cells from Wharton's Jelly after Complete Transection of the Rat Spinal Cord," *PLoS ONE*, vol. 3, no. 10, Oct. 2008.

[39] E. Sykova and P. Jendelova, "In vivo tracking of stem cells in brain and spinal cord injury," in *Progress in Brain Research*, vol. 161, J. T. W. and A. I. R. Maas, Ed. Elsevier, 2007, pp. 367–383.

[40] F. Callera and C. M. T. P. de Melo, "Magnetic resonance tracking of magnetically labeled autologous bone marrow CD34+ cells transplanted into the spinal cord via lumbar puncture technique in patients with chronic spinal cord injury: CD34+ cells' migration into the injured site," *Stem Cells Dev.*, vol. 16, no. 3, pp. 461–466, Jun. 2007.

[41] Z.-F. Jia *et al.*, "Fluorescent Nanoparticles for Observing Primo Vascular System Along Sciatic Nerve," *J. Acupunct. Meridian Stud.*, vol. 3, no. 3, pp. 150–155, Sep. 2010.

[42] E. Lueshen, I. Venugopal, J. Kanikunnel, T. Soni, A. Alaraj, and A. Linninger, "Intrathecal magnetic drug targeting using gold-coated magnetite nanoparticles in a human spine model," *Nanomed.*, pp. 1–15, Jul. 2013.

[43] E. Lueshen, I. Venugopal, T. Soni, A. Alaraj, and A. Linninger, "Implant-Assisted Intrathecal Magnetic Drug Targeting to Aid in Therapeutic Nanoparticle Localization for Potential Treatment of Central Nervous System Disorders," *J. Biomed. Nanotechnol.*, vol. 11, no. 2, pp. 253–261, Feb. 2015.

[44] N. D. Jeffery, S. C. McBain, J. Dobson, and D. M. Chari, "Uptake of systemically administered magnetic nanoparticles (MNPs) in areas of experimental spinal cord injury (SCI)," *J. Tissue Eng. Regen. Med.*, vol. 3, no. 2, pp. 153–157, Feb. 2009.

[45]  I. Venugopal, S. Pernal, T. Fusinatto, D. Ashkenaz, and A. Linninger, "Quantum Dot Conjugated Magnetic Nanoparticles for Targeted Drug Delivery and Imaging," *Nano Biomed. Eng.*, vol. 8, no. 1, Mar. 2016.

[46]  I. Venugopal, S. Pernal, A. Duproz, J. Bentley, H. Engelhard, and A. Linninger, "Magnetic field-enhanced cellular uptake of doxorubicin loaded magnetic nanoparticles for tumor treatment," *Mater. Res. Express*, vol. 3, no. 9, p. 95010, 2016.

[47]  A. Bossavit, *Computational Electromagnetism: Variational Formulations, Complementarity, Edge Elements*. Academic Press, 1998.

[48]  M. Bartsch *et al.*, "Solution of Maxwell's equations," *Comput. Phys. Commun.*, vol. 73, no. 1, pp. 22–39, Dec. 1992.

[49]  Popa, Constantin, and Tudor Udrescu, "A fast solver for magnetostatic field problems," *ROMANIAN J. Phys.*, vol. 52, no. 3/4, p. 257, 2007.

[50]  B. V. de Wiele, A. Manzin, O. Bottauscio, M. Chiampi, L. Dupre, and F. Olyslager, "Finite-Difference and Edge Finite-Element Approaches for Dynamic Micromagnetic Modeling," *IEEE Trans. Magn.*, vol. 44, no. 11, pp. 3137–3140, Nov. 2008.

[51]  B. V. de Wiele, A. Manzin, L. Dupre, F. Olyslager, O. Bottauscio, and M. Chiampi, "Comparison of Finite-Difference and Finite-Element Schemes for Magnetization Processes in 3-D Particles," *IEEE Trans. Magn.*, vol. 45, no. 3, pp. 1614–1617, Mar. 2009.

[52]  A. Bondeson, T. Rylander, and P. Ingelström, *Computational Electromagnetics*. Springer Science & Business Media, 2005.

[53]  J. E. Miltat and M. J. Donahue, "Numerical Micromagnetics: Finite Difference Methods," in *Handbook of Magnetism and Advanced Magnetic Materials*, John Wiley & Sons, Ltd, 2007.

[54]  Humphries, S, "Finite-element methods for electromagnetic," 1997.

[55]  Wolfgang H; Andre B; Wolfgang R, "Solution of Magnetostatic Field Problems with the Integral Equation Method," *ICS Newsl.*, 2006.

[56]  K. Lipnikov, G. Manzini, F. Brezzi, and A. Buffa, "The mimetic finite difference method for the 3D magnetostatic field problems on polyhedral meshes," *J. Comput. Phys.*, vol. 230, no. 2, pp. 305–328, Jan. 2011.

[57]  Schöberl J., "Numerical Methods for Maxwell Equations," 2009.

[58]  Sarma, Mulukutla S, "Finite element formation for the numerical solution of three-dimensional nonlinear magnetostatic field problems as applied to the design of electric machinery.," 1976.

[59]  Trowbridge, C. W., "Progress in magnet design by computer," 1972.

[60]  M. J. Friedman, "Finite element formulation of the general magnetostatic problem in the space of solenoidal vector functions," *Math. Comput.*, vol. 43, no. 168, pp. 415–431, 1984.

[61]  E. A. Burfine, L. R. Anderson, and H. Brechna, "A Computer Code for Variable Permeability Magnetostatic Field Problems," Stanford Linear Accelerator Center, Stanford Univ., Calif., SLAC-56, Apr. 1966.

[62]  O. Aaboubi, J. P. Chopart, J. Douglade, A. Olivier, C. Gabrielli, and B. Tribollet, "Magnetic Field Effects on Mass Transport," *J. Electrochem. Soc.*, vol. 137, no. 6, pp. 1796–1804, Jun. 1990.

[63] E. J. Furlani and E. P. Furlani, "A model for predicting magnetic targeting of multifunctional particles in the microvasculature," *J. Magn. Magn. Mater.*, vol. 312, no. 1, pp. 187–193, May 2007.

[64] S. Sharma, V. K. Katiyar, and U. Singh, "Mathematical modelling for trajectories of magnetic nanoparticles in a blood vessel under magnetic field," *J. Magn. Magn. Mater.*, vol. 379, pp. 102–107, Apr. 2015.

[65] N. Tran and T. J. Webster, "Increased osteoblast functions in the presence of hydroxyapatite-coated iron oxide nanoparticles," *Acta Biomater.*, vol. 7, no. 3, pp. 1298–1306, Mar. 2011.

[66] C. R. Uthra, R. Vasanthakumari, C. R. Uthra, and R. Vasanthakumari, "A Mathematical Model for the Movement of Magnetic Nanoparticles in the Field of Small Magnets Described by Poiseuille Flow," *Appl. Math.*, vol. 5, no. 3, pp. 68–72, 2015.

[67] P. J. Cregg, K. Murphy, and A. Mardinoglu, "Calculation of nanoparticle capture efficiency in magnetic drug targeting," *J. Magn. Magn. Mater.*, vol. 320, no. 23, pp. 3272–3275, Dec. 2008.

[68] G. Hinds, J. M. D. Coey, and M. E. G. Lyons, "Influence of magnetic forces on electrochemical mass transport," *Electrochem. Commun.*, vol. 3, no. 5, pp. 215–218, May 2001.

[69] T. Lunnoo and T. Puangmali, "Capture Efficiency of Biocompatible Magnetic Nanoparticles in Arterial Flow: A Computer Simulation for Magnetic Drug Targeting," *Nanoscale Res. Lett.*, vol. 10, no. 1, p. 426, Dec. 2015.

[70] M. Waskaas and Y. I. Kharkats, "Effect of magnetic fields on convection in solutions containing paramagnetic ions," *J. Electroanal. Chem.*, vol. 502, no. 1–2, pp. 51–57, Apr. 2001.

[71] M. Waskaas and Y. I. Kharkats, "Magnetoconvection Phenomena: A Mechanism for Influence of Magnetic Fields on Electrochemical Processes," *J. Phys. Chem. B*, vol. 103, no. 23, pp. 4876–4883, Jun. 1999.

[72] E. P. Furlani and K. C. Ng, "Analytical model of magnetic nanoparticle transport and capture in the microvasculature," *Phys. Rev. E*, vol. 73, no. 6, p. 61919, Jun. 2006.

[73] E. P. Furlani and X. Xue, "Field, force and transport analysis for magnetic particle-based gene delivery," *Microfluid. Nanofluidics*, vol. 13, no. 4, pp. 589–602, Oct. 2012.

[74] Q. A. Pankhurst, J. Connolly, S. K. Jones, and J. Dobson, "Applications of magnetic nanoparticles in biomedicine," *J. Phys. Appl. Phys.*, vol. 36, no. 13, p. R167, 2003.

[75] K. M. Tangen, Y. Hsu, D. C. Zhu, and A. A. Linninger, "CNS wide simulation of flow resistance and drug transport due to spinal microanatomy," *J. Biomech.*, vol. 48, no. 10, pp. 2144–2154, Jul. 2015.

[76] K. Tangen, N. S. Narasimhan, K. Sierzega, T. Preden, A. Alaraj, and A. A. Linninger, "Clearance of Subarachnoid Hemorrhage from the Cerebrospinal Fluid in Computational and In Vitro Models," *Ann. Biomed. Eng.*, Jul. 2016.

[77] J. A. DiMasi, R. W. Hansen, H. G. Grabowski, and L. Lasagna, "Cost of innovation in the pharmaceutical industry," *J. Health Econ.*, vol. 10, no. 2, pp. 107–142, Jul. 1991.

[78] L. B. Cardinal, "Technological Innovation in the Pharmaceutical Industry: The Use of Organizational Control in Managing Research and Development," *Organ. Sci.*, vol. 12, no. 1, pp. 19–36, Jan. 2001.

[79]  T. K. Jain, J. Richey, M. Strand, D. L. Leslie-Pelecky, C. A. Flask, and V. Labhasetwar, "Magnetic nanoparticles with dual functional properties: Drug delivery and magnetic resonance imaging," *Biomaterials*, vol. 29, no. 29, pp. 4012–4021, Oct. 2008.

[80]  N. Kohler, C. Sun, A. Fichtenholtz, J. Gunn, C. Fang, and M. Zhang, "Methotrexate-Immobilized Poly(ethylene glycol) Magnetic Nanoparticles for MR Imaging and Drug Delivery," *Small*, vol. 2, no. 6, pp. 785–792, 2006.

[81]  S. Mornet, J. Portier, and E. Duguet, "A method for synthesis and functionalization of ultrasmall superparamagnetic covalent carriers based on maghemite and dextran," *J. Magn. Magn. Mater.*, vol. 293, no. 1, pp. 127–134, May 2005.

[82]  M. Liong *et al.*, "Multifunctional Inorganic Nanoparticles for Imaging, Targeting, and Drug Delivery," *ACS Nano*, vol. 2, no. 5, pp. 889–896, May 2008.

[83]  H. D. M. Hettiarachchi, Y. Hsu, T. J. H. Jr, and A. A. Linninger, "The Effect of Pulsatile Flow on Intrathecal Drug Delivery in the Spinal Canal," *Ann. Biomed. Eng.*, vol. 39, no. 10, pp. 2592–2602, Oct. 2011.

[84]  W. M. Pardridge, *Brain drug targeting: the future of brain drug development*. Cambridge ; New York: Cambridge University Press, 2001.

[85]  G. R. Reddy *et al.*, "Vascular Targeted Nanoparticles for Imaging and Treatment of Brain Tumors," *Clin. Cancer Res.*, vol. 12, no. 22, pp. 6677–6686, Nov. 2006.

[86]  W. S. Enochs, G. Harsh, F. Hochberg, and R. Weissleder, "Improved delineation of human brain tumors on MR images using a long-circulating, superparamagnetic iron oxide agent," *J. Magn. Reson. Imaging*, vol. 9, no. 2, pp. 228–232, 1999.

[87]  M. E. Davis, Z. (Georgia) Chen, and D. M. Shin, "Nanoparticle therapeutics: an emerging treatment modality for cancer," *Nat. Rev. Drug Discov.*, vol. 7, no. 9, pp. 771–782, Sep. 2008.

[88]  O. Veiseh, J. W. Gunn, and M. Zhang, "Design and fabrication of magnetic nanoparticles for targeted drug delivery and imaging," *Adv. Drug Deliv. Rev.*, vol. 62, no. 3, pp. 284–304, Mar. 2010.

[89]  D. A. Gorin *et al.*, "Magnetic/gold nanoparticle functionalized biocompatible microcapsules with sensitivity to laser irradiation," *Phys. Chem. Chem. Phys.*, vol. 10, no. 45, p. 6899, 2008.

[90]  Q. He and J. Shi, "Mesoporous silica nanoparticle based nano drug delivery systems: synthesis, controlled drug release and delivery, pharmacokinetics and biocompatibility," *J. Mater. Chem.*, vol. 21, no. 16, p. 5845, 2011.

[91]  J. E. Kipp, "The role of solid nanoparticle technology in the parenteral delivery of poorly water-soluble drugs," *Int. J. Pharm.*, vol. 284, no. 1–2, pp. 109–122, Oct. 2004.

[92]  J. Zhang and R. D. K. Misra, "Magnetic drug-targeting carrier encapsulated with thermosensitive smart polymer: Core–shell nanoparticle carrier and drug release response," *Acta Biomater.*, vol. 3, no. 6, pp. 838–850, Nov. 2007.

[93]  G. Huang, J. Gao, Z. Hu, J. V. St. John, B. C. Ponder, and D. Moro, "Controlled drug release from hydrogel nanoparticle networks," *J. Controlled Release*, vol. 94, no. 2–3, pp. 303–311, Feb. 2004.

[94]  J. Hu, D. K. P. Johnston, and I. I. I. Dr. Robert O. Williams, "Nanoparticle Engineering Processes for Enhancing the Dissolution Rates of Poorly Water Soluble Drugs," 03-Nov-

2004. [Online]. Available: http://informahealthcare.com/doi/abs/10.1081/DDC-120030422. [Accessed: 07-Mar-2013].

[95]  Y. Wang, S. Gao, W.-H. Ye, H. S. Yoon, and Y.-Y. Yang, "Co-delivery of drugs and DNA from cationic core–shell nanoparticles self-assembled from a biodegradable copolymer," *Nat. Mater.*, vol. 5, no. 10, pp. 791–796, Oct. 2006.

[96]  L. Zhang *et al.*, "Co-Delivery of Hydrophobic and Hydrophilic Drugs from Nanoparticle–Aptamer Bioconjugates," *ChemMedChem*, vol. 2, no. 9, pp. 1268–1271, 2007.

[97]  A. Jordan *et al.*, "Presentation of a new magnetic field therapy system for the treatment of human solid tumors with magnetic fluid hyperthermia," *J. Magn. Magn. Mater.*, vol. 225, no. 1, pp. 118–126, 2001.

[98]  H. B. Na, I. C. Song, and T. Hyeon, "Inorganic Nanoparticles for MRI Contrast Agents," *Adv. Mater.*, vol. 21, no. 21, pp. 2133–2148, 2009.

[99]  S. A. Corr *et al.*, "Linear Assemblies of Magnetic Nanoparticles as MRI Contrast Agents," *J. Am. Chem. Soc.*, vol. 130, no. 13, pp. 4214–4215, Apr. 2008.

[100]  J. Kim *et al.*, "Multifunctional Uniform Nanoparticles Composed of a Magnetite Nanocrystal Core and a Mesoporous Silica Shell for Magnetic Resonance and Fluorescence Imaging and for Drug Delivery," *Angew. Chem. Int. Ed.*, vol. 47, no. 44, pp. 8438–8441, 2008.

[101]  N. Nasongkla *et al.*, "Multifunctional Polymeric Micelles as Cancer-Targeted, MRI-Ultrasensitive Drug Delivery Systems," *Nano Lett.*, vol. 6, no. 11, pp. 2427–2430, Nov. 2006.

[102]  J. Kim *et al.*, "Designed Fabrication of a Multifunctional Polymer Nanomedical Platform for Simultaneous Cancer- Targeted Imaging and Magnetically Guided Drug Delivery," *Adv. Mater.*, vol. 20, no. 3, pp. 478–483, 2008.

[103]  J. E. Lee *et al.*, "Uniform Mesoporous Dye-Doped Silica Nanoparticles Decorated with Multiple Magnetite Nanocrystals for Simultaneous Enhanced Magnetic Resonance Imaging, Fluorescence Imaging, and Drug Delivery," *J. Am. Chem. Soc.*, vol. 132, no. 2, pp. 552–557, Jan. 2010.

[104]  J.-H. Park, G. von Maltzahn, E. Ruoslahti, S. N. Bhatia, and M. J. Sailor, "Micellar Hybrid Nanoparticles for Simultaneous Magnetofluorescent Imaging and Drug Delivery," *Angew. Chem.*, vol. 120, no. 38, pp. 7394–7398, 2008.

[105]  M.-C. Bourg, A. Badia, and R. B. Lennox, "Gold–Sulfur Bonding in 2D and 3D Self-Assembled Monolayers:  XPS Characterization," *J. Phys. Chem. B*, vol. 104, no. 28, pp. 6562–6567, Jul. 2000.

[106]  S. H. Lee, K. H. Bae, S. H. Kim, K. R. Lee, and T. G. Park, "Amine-functionalized gold nanoparticles as non-cytotoxic and efficient intracellular siRNA delivery carriers," *Int. J. Pharm.*, vol. 364, no. 1, pp. 94–101, Nov. 2008.

[107]  W. C. W. Chan and S. Nie, "Quantum Dot Bioconjugates for Ultrasensitive Nonisotopic Detection," *Science*, vol. 281, no. 5385, pp. 2016–2018, Sep. 1998.

[108]  Z. Kaul, T. Yaguchi, S. C. Kaul, T. Hirano, R. Wadhwa, and K. Taira, "Mortalin imaging in normal and cancer cells with quantum dot immuno-conjugates," *Cell Res.*, vol. 13, no. 6, pp. 503–507, Dec. 2003.

[109] A. F. van Driel, G. Allan, C. Delerue, P. Lodahl, W. L. Vos, and D. Vanmaekelbergh, "Frequency-Dependent Spontaneous Emission Rate from CdSe and CdTe Nanocrystals: Influence of Dark States," *Phys. Rev. Lett.*, vol. 95, no. 23, p. 236804, Dec. 2005.

[110] M. Mandal *et al.*, "Magnetite nanoparticles with tunable gold or silver shell," *J. Colloid Interface Sci.*, vol. 286, no. 1, pp. 187–194, Jun. 2005.

[111] L. P. Ramirez and K. Landfester, "Magnetic polystyrene nanoparticles with a high magnetite content obtained by miniemulsion processes," *Macromol. Chem. Phys.*, vol. 204, no. 1, pp. 22–31, 2003.

[112] A.-H. Lu, E. L. Salabas, and F. Schüth, "Magnetic Nanoparticles: Synthesis, Protection, Functionalization, and Application," *Angew. Chem. Int. Ed.*, vol. 46, no. 8, pp. 1222–1244, 2007.

[113] R. A. Frimpong, J. Dou, M. Pechan, and J. Z. Hilt, "Enhancing remote controlled heating characteristics in hydrophilic magnetite nanoparticles via facile co-precipitation," *J. Magn. Magn. Mater.*, vol. 322, no. 3, pp. 326–331, 2010.

[114] J. Duan, L. Song, and J. Zhan, "One-pot synthesis of highly luminescent CdTe quantum dots by microwave irradiation reduction and their Hg2+-sensitive properties," *Nano Res.*, vol. 2, no. 1, pp. 61–68, Mar. 2010.

[115] T. Lühmann, M. Rimann, A. G. Bittermann, and H. Hall, "Cellular uptake and intracellular pathways of PLL-g-PEG-DNA nanoparticles," *Bioconjug. Chem.*, vol. 19, no. 9, pp. 1907–1916, 2008.

[116] R. Bhadelia, A. Bogdan, R. Kaplan, and S. Wolpert, "Cerebrospinal fluid pulsation amplitude and its quantitative relationship to cerebral blood flow pulsations: a phase-contrast MR flow imaging study," *Neuroradiology*, vol. 39, no. 4, pp. 258–264, 1997.

[117] M. Freund *et al.*, "[Measurement of CSF flow in the spinal canal using MRI with an optimized MRI protocol: experimental and clinical studies]," *ROFO. Fortschr. Geb. Rontgenstr. Nuklearmed.*, vol. 173, no. 4, pp. 306–314, 2001.

[118] A. C. Lui, T. Z. Polis, and N. J. Cicutti, "Densities of cerebrospinal fluid and spinal anaesthetic solutions in surgical patients at body temperature," *Can. J. Anaesth.*, vol. 45, no. 4, pp. 297–303, 1998.

[119] J. Chatterjee, Y. Haik, and C.-J. Chen, "Size dependent magnetic properties of iron oxide nanoparticles," *J. Magn. Magn. Mater.*, vol. 257, no. 1, pp. 113–118, 2003.

[120] H. Itoh and T. Sugimoto, "Systematic control of size, shape, structure, and magnetic properties of uniform magnetite and maghemite particles," *J. Colloid Interface Sci.*, vol. 265, no. 2, pp. 283–295, Sep. 2003.

[121] J. A. Dearing, P. M. Bird, R. J. L. Dann, and S. F. Benjamin, "Secondary ferrimagnetic minerals in Welsh soils: a comparison of mineral magnetic detection methods and implications for mineral formation," *Geophys. J. Int.*, vol. 130, no. 3, pp. 727–736, 1997.

[122] V. I. Klimov *et al.*, "Optical Gain and Stimulated Emission in Nanocrystal Quantum Dots," *Science*, vol. 290, no. 5490, pp. 314–317, Oct. 2000.

[123] N.-M. Park, C.-J. Choi, T.-Y. Seong, and S.-J. Park, "Quantum Confinement in Amorphous Silicon Quantum Dots Embedded in Silicon Nitride," *Phys. Rev. Lett.*, vol. 86, no. 7, pp. 1355–1357, Feb. 2001.

[124] E. Dulkeith *et al.*, "Fluorescence Quenching of Dye Molecules near Gold Nanoparticles: Radiative and Nonradiative Effects," *Phys. Rev. Lett.*, vol. 89, no. 20, p. 203002, Oct. 2002.

[125] E. Dulkeith, M. Ringler, T. A. Klar, J. Feldmann, A. Muñoz Javier, and W. J. Parak, "Gold Nanoparticles Quench Fluorescence by Phase Induced Radiative Rate Suppression," *Nano Lett.*, vol. 5, no. 4, pp. 585–589, Apr. 2005.

[126] C. C. Berry, "Possible exploitation of magnetic nanoparticle?cell interaction for biomedical applications," *J. Mater. Chem.*, vol. 15, no. 5, p. 543, 2005.

[127] I. Brigger, C. Dubernet, and P. Couvreur, "Nanoparticles in cancer therapy and diagnosis," *Adv. Drug Deliv. Rev.*, vol. 64, Supplement, pp. 24–36, Dec. 2012.

[128] H. He, X. Sun, X. Wang, and H. Xu, "Synthesis of highly luminescent and biocompatible CdTe/CdS/ZnS quantum dots using microwave irradiation: a comparative study of different ligands," *Lumin. J. Biol. Chem. Lumin.*, vol. 29, no. 7, pp. 837–845, Nov. 2014.

[129] H. Qian, C. Dong, J. Weng, and J. Ren, "Facile one-pot synthesis of luminescent, water-soluble, and biocompatible glutathione-coated CdTe nanocrystals," *Small Weinh. Bergstr. Ger.*, vol. 2, no. 6, pp. 747–751, Jun. 2006.

[130] R. K. Singhal, M. E. Anderson, and A. Meister, "Glutathione, a first line of defense against cadmium toxicity," *FASEB J. Off. Publ. Fed. Am. Soc. Exp. Biol.*, vol. 1, no. 3, pp. 220–223, Sep. 1987.

[131] H. Soo Choi *et al.*, "Renal clearance of quantum dots," *Nat. Biotechnol.*, vol. 25, no. 10, pp. 1165–1170, Oct. 2007.

[132] B. D. Chithrani, A. A. Ghazani, and W. C. W. Chan, "Determining the Size and Shape Dependence of Gold Nanoparticle Uptake into Mammalian Cells," *Nano Lett.*, vol. 6, no. 4, pp. 662–668, Apr. 2006.

[133] R. Siegel, J. Ma, Z. Zou, and A. Jemal, "Cancer statistics, 2014," *CA. Cancer J. Clin.*, vol. 64, no. 1, pp. 9–29, 2014.

[134] M. Nahar *et al.*, "Functional Polymeric Nanoparticles: An Efficient and Promising Tool for Active Delivery of Bioactives," *Crit. Rev. Ther. Drug Carr. Syst.*, vol. 23, no. 4, pp. 259–318, 2006.

[135] K. Cho, X. Wang, S. Nie, and D. M. Shin, "Therapeutic nanoparticles for drug delivery in cancer," *Clin. Cancer Res.*, vol. 14, no. 5, pp. 1310–1316, 2008.

[136] D. Peer, J. M. Karp, S. Hong, O. C. Farokhzad, R. Margalit, and R. Langer, "Nanocarriers as an emerging platform for cancer therapy," *Nat. Nanotechnol.*, vol. 2, no. 12, pp. 751–760, Dec. 2007.

[137] Y. Matsumura and H. Maeda, "A New Concept for Macromolecular Therapeutics in Cancer Chemotherapy: Mechanism of Tumoritropic Accumulation of Proteins and the Antitumor Agent Smancs," *Cancer Res.*, vol. 46, no. 12 Part 1, pp. 6387–6392, Dec. 1986.

[138] F. Yuan *et al.*, "Vascular Permeability in a Human Tumor Xenograft: Molecular Size Dependence and Cutoff Size," *Cancer Res.*, vol. 55, no. 17, pp. 3752–3756, Sep. 1995.

[139] M. Arruebo, R. Fernández-Pacheco, M. R. Ibarra, and J. Santamaría, "Magnetic nanoparticles for drug delivery," *Nano Today*, vol. 2, no. 3, pp. 22–32, Jun. 2007.

[140] C. Sun, J. S. H. Lee, and M. Zhang, "Magnetic nanoparticles in MR imaging and drug delivery," *Adv. Drug Deliv. Rev.*, vol. 60, no. 11, pp. 1252–1265, Aug. 2008.

[141] A. Prokop and J. M. Davidson, "Nanovehicular intracellular delivery systems," *J. Pharm. Sci.*, vol. 97, no. 9, pp. 3518–3590, 2008.

[142] U. Zimmermann, G. Pilwat, F. Beckers, and F. Riemann, "Effects of external electrical fields on cell membranes," *Bioelectrochem. Bioenerg.*, vol. 3, no. 1, pp. 58–83, 1976.

[143] U. O. Häfeli, S. M. Sweeney, B. A. Beresford, E. H. Sim, and R. M. Macklis, "Magnetically directed poly(lactic acid) 90Y-microspheres: Novel agents for targeted intracavitary radiotherapy," *J. Biomed. Mater. Res.*, vol. 28, no. 8, pp. 901–908, 1994.

[144] H. Engelhard and D. Petruska, "Imaging and movement of iron-oxide-bound antibody microparticles in brain and cerebrospinal fluid.," *Cancer Biochem. Biophys.*, vol. 13, no. 1, pp. 1–12, 1992.

[145] U. O. Häfeli, S. M. Sweeney, B. A. Beresford, J. L. Humm, and R. M. Macklis, "Effective targeting of magnetic radioactive90Y-microspheres to tumor cells by an externally applied magnetic field. Preliminary in vitro and in vivo results," *Nucl. Med. Biol.*, vol. 22, no. 2, pp. 147–155, Feb. 1995.

[146] A. S. Lübbe *et al.*, "Preclinical Experiences with Magnetic Drug Targeting: Tolerance and Efficacy," *Cancer Res.*, vol. 56, no. 20, pp. 4694–4701, Oct. 1996.

[147] S. Goodwin, C. Peterson, C. Hoh, and C. Bittner, "Targeting and retention of magnetic targeted carriers (MTCs) enhancing intra-arterial chemotherapy," *J. Magn. Magn. Mater.*, vol. 194, no. 1–3, pp. 132–139, Apr. 1999.

[148] A. Jordan, R. Scholz, P. Wust, H. Fähling, and R. Felix, "Magnetic fluid hyperthermia (MFH): Cancer treatment with AC magnetic field induced excitation of biocompatible superparamagnetic nanoparticles," *J. Magn. Magn. Mater.*, vol. 201, no. 1, pp. 413–419, 1999.

[149] T. Yoon *et al.*, "Specific targeting, cell sorting, and bioimaging with smart magnetic silica core–shell nanomaterials," *Small*, vol. 2, no. 2, pp. 209–215, 2006.

[150] R. Weissleder, K. Kelly, E. Y. Sun, T. Shtatland, and L. Josephson, "Cell-specific targeting of nanoparticles by multivalent attachment of small molecules," *Nat. Biotechnol.*, vol. 23, no. 11, pp. 1418–1423, 2005.

[151] H.-Y. Park *et al.*, "Fabrication of magnetic core@ shell Fe oxide@ Au nanoparticles for interfacial bioactivity and bio-separation," *Langmuir*, vol. 23, no. 17, pp. 9050–9056, 2007.

[152] F. N. Crespilho, M. Emilia Ghica, M. Florescu, F. C. Nart, O. N. Oliveira Jr, and C. Brett, "A strategy for enzyme immobilization on layer-by-layer dendrimer–gold nanoparticle electrocatalytic membrane incorporating redox mediator," *Electrochem. Commun.*, vol. 8, no. 10, pp. 1665–1670, 2006.

[153] N. T. K. Thanh and Z. Rosenzweig, "Development of an aggregation-based immunoassay for anti-protein A using gold nanoparticles," *Anal. Chem.*, vol. 74, no. 7, pp. 1624–1628, 2002.

[154] X. Liu *et al.*, "A one-step homogeneous immunoassay for cancer biomarker detection using gold nanoparticle probes coupled with dynamic light scattering," *J. Am. Chem. Soc.*, vol. 130, no. 9, pp. 2780–2782, 2008.

[155] T. A. Taton, C. A. Mirkin, and R. L. Letsinger, "Scanometric DNA array detection with nanoparticle probes," *Science*, vol. 289, no. 5485, pp. 1757–1760, 2000.

[156] J. Dobson, "Gene therapy progress and prospects: magnetic nanoparticle-based gene delivery," *Gene Ther.*, vol. 13, no. 4, pp. 283–287, 2006.

[157] S. C. Goodwin, C. A. Bittner, C. L. Peterson, and G. Wong, "Single-Dose Toxicity Study of Hepatic Intra-arterial Infusion of Doxorubicin Coupled to a Novel Magnetically Targeted Drug Carrier," *Toxicol. Sci.*, vol. 60, no. 1, pp. 177–183, Mar. 2001.

[158] F. Wiekhorst *et al.*, "Quantification of Magnetic Nanoparticles by Magnetorelaxometry and Comparison to Histology After Magnetic Drug Targeting," *J. Nanosci. Nanotechnol.*, vol. 6, no. 9–1, pp. 3222–3225, Sep. 2006.

[159] M.-Y. Hua *et al.*, "Superhigh-magnetization nanocarrier as a doxorubicin delivery platform for magnetic targeting therapy," *Biomaterials*, vol. 32, no. 34, pp. 8999–9010, Dec. 2011.

[160] Y. Yuan *et al.*, "Epidermal Growth Factor Receptor Targeted Nuclear Delivery and High-Resolution Whole Cell X-ray Imaging of Fe3O4@ TiO2 Nanoparticles in Cancer Cells," *ACS Nano*, vol. 7, no. 12, pp. 10502–10517, 2013.

[161] A. Ito, M. Shinkai, H. Honda, and T. Kobayashi, "Medical application of functionalized magnetic nanoparticles," *J. Biosci. Bioeng.*, vol. 100, no. 1, pp. 1–11, Jul. 2005.

[162] M. Brust, D. J. Schiffrin, D. Bethell, and C. J. Kiely, "Novel gold-dithiol nano-networks with non-metallic electronic properties," *Adv. Mater.*, vol. 7, no. 9, pp. 795–797, 1995.

[163] M. Giersig and P. Mulvaney, "Preparation of ordered colloid monolayers by electrophoretic deposition," *Langmuir*, vol. 9, no. 12, pp. 3408–3413, 1993.

[164] M. Hasan, D. Bethell, and M. Brust, "The fate of sulfur-bound hydrogen on formation of self-assembled thiol monolayers on gold: 1H NMR spectroscopic evidence from solutions of gold clusters," *J. Am. Chem. Soc.*, vol. 124, no. 7, pp. 1132–1133, 2002.

[165] M. Brust, M. Walker, D. Bethell, D. J. Schiffrin, and R. Whyman, "Synthesis of thiol-derivatised gold nanoparticles in a two-phase liquid–liquid system," *J Chem Soc Chem Commun*, no. 7, pp. 801–802, 1994.

[166] M. Brust, J. Fink, D. Bethell, D. Schiffrin, and C. Kiely, "Synthesis and reactions of functionalised gold nanoparticles," *J Chem Soc Chem Commun*, no. 16, pp. 1655–1656, 1995.

[167] M. Arruebo, R. Fernández-Pacheco, S. Irusta, J. Arbiol, M. R. Ibarra, and J. Santamaría, "Sustained release of doxorubicin from zeolite–magnetite nanocomposites prepared by mechanical activation," *Nanotechnology*, vol. 17, no. 16, p. 4057, 2006.

[168] Y. Ma, S. Manolache, F. S. Denes, D. H. Thamm, I. D. Kurzman, and D. M. Vail, "Plasma synthesis of carbon magnetic nanoparticles and immobilization of doxorubicin for targeted drug delivery," *J. Biomater. Sci. Polym. Ed.*, vol. 15, no. 8, pp. 1033–1049, 2004.

[169] M. Muthana *et al.*, "A novel magnetic approach to enhance the efficacy of cell-based gene therapies," *Gene Ther.*, vol. 15, no. 12, pp. 902–910, 2008.

[170] S. W. Kamau *et al.*, "Enhancement of the efficiency of non-viral gene delivery by application of pulsed magnetic field," *Nucleic Acids Res.*, vol. 34, no. 5, pp. e40–e40, 2006.

[171] F. Scherer *et al.*, "Magnetofection: enhancing and targeting gene delivery by magnetic force in vitro and in vivo," *Gene Ther.*, vol. 9, no. 2, pp. 102–109, 2002.

[172] C. Plank, F. Scherer, U. Schillinger, C. Bergemann, and M. Anton, "Magnetofection: enhancing and targeting gene delivery with superparamagnetic nanoparticles and magnetic fields," *J. Liposome Res.*, vol. 13, no. 1, pp. 29–32, 2003.

[173] T. Yoon, J. S. Kim, B. G. Kim, K. N. Yu, M. Cho, and J. Lee, "Multifunctional nanoparticles possessing a 'magnetic motor effect' for drug or gene delivery," *Angew. Chem.*, vol. 117, no. 7, pp. 1092–1095, 2005.

[174] J. Sommertune *et al.*, "Polymer/Iron Oxide Nanoparticle Composites—A Straight Forward and Scalable Synthesis Approach," *Int. J. Mol. Sci.*, vol. 16, no. 8, pp. 19752–19768, Aug. 2015.

[175] P. Twentyman and M. Luscombe, "A study of some variables in a tetrazolium dye (MTT) based assay for cell growth and chemosensitivity.," *Br. J. Cancer*, vol. 56, no. 3, p. 279, 1987.

[176] D. Glick, S. Barth, and K. F. Macleod, "Autophagy: cellular and molecular mechanisms," *J. Pathol.*, vol. 221, no. 1, pp. 3–12, 2010.

[177] J. M. Gump and A. Thorburn, "Autophagy and apoptosis: what is the connection?," *Trends Cell Biol.*, vol. 21, no. 7, pp. 387–392, 2011.

[178] L. Yu *et al.*, "Regulation of an ATG7-beclin 1 program of autophagic cell death by caspase-8," *Science*, vol. 304, no. 5676, pp. 1500–1502, 2004.

[179] G. Han, P. Ghosh, M. De, and V. M. Rotello, "Drug and gene delivery using gold nanoparticles," *NanoBiotechnology*, vol. 3, no. 1, pp. 40–45, Apr. 2007.

[180] G. F. Paciotti *et al.*, "Colloidal Gold: A Novel Nanoparticle Vector for Tumor Directed Drug Delivery," *Drug Deliv.*, vol. 11, no. 3, pp. 169–183, Jan. 2004.

[181] S. Dhar, E. M. Reddy, A. Shiras, V. Pokharkar, and B. L. V. Prasad, "Natural Gum Reduced/Stabilized Gold Nanoparticles for Drug Delivery Formulations," *Chem. – Eur. J.*, vol. 14, no. 33, pp. 10244–10250, 2008.

[182] M. Tako, "The Principle of Polysaccharide Gels," *Adv. Biosci. Biotechnol.*, vol. 6, no. 1, pp. 22–36, 2015.

[183] L. Gutiérrez *et al.*, "Synthesis methods to prepare single- and multi-core iron oxide nanoparticles for biomedical applications," *Dalton Trans. Camb. Engl. 2003*, vol. 44, no. 7, pp. 2943–2952, Feb. 2015.

[184] H. Nobuto *et al.*, "Evaluation of systemic chemotherapy with magnetic liposomal doxorubicin and a dipole external electromagnet," *Int. J. Cancer*, vol. 109, no. 4, pp. 627–635, 2004.

[185] S. Huth *et al.*, "Insights into the mechanism of magnetofection using PEI-based magnetofectins for gene transfer," *J. Gene Med.*, vol. 6, no. 8, pp. 923–936, 2004.

[186] S. W. Gersting *et al.*, "Gene delivery to respiratory epithelial cells by magnetofection," *J. Gene Med.*, vol. 6, no. 8, pp. 913–922, 2004.

[187] S.-J. Sung *et al.*, "Effect of polyethylene glycol on gene delivery of polyethylenimine," *Biol. Pharm. Bull.*, vol. 26, no. 4, pp. 492–500, 2003.

[188] M. Ogris, P. Steinlein, M. Kursa, K. Mechtler, R. Kircheis, and E. Wagner, "The size of DNA/transferrin-PEI complexes is an important factor for gene expression in cultured cells.," *Gene Ther.*, vol. 5, no. 10, pp. 1425–1433, 1998.

[189] Q. A. Pankhurst, J. Connolly, S. K. Jones, and J. Dobson, "Applications of magnetic nanoparticles in biomedicine," *J. Phys. Appl. Phys.*, vol. 36, no. 13, p. R167, Jul. 2003.

[190] Wahajuddin and S. Arora, "Superparamagnetic iron oxide nanoparticles: magnetic nanoplatforms as drug carriers," *Int. J. Nanomedicine*, vol. 7, pp. 3445–3471, 2012.

[191] N. J. Abbott, "Blood-brain barrier structure and function and the challenges for CNS drug delivery," *J. Inherit. Metab. Dis.*, vol. 36, no. 3, pp. 437–449, May 2013.

[192] T. M. Barchet and M. M. Amiji, "Challenges and opportunities in CNS delivery of therapeutics for neurodegenerative diseases," *Expert Opin. Drug Deliv.*, vol. 6, no. 3, pp. 211–225, Mar. 2009.

[193] D. J. Begley, "Delivery of therapeutic agents to the central nervous system: the problems and the possibilities," *Pharmacol. Ther.*, vol. 104, no. 1, pp. 29–45, Oct. 2004.

[194] A. Misra, S. Ganesh, A. Shahiwala, and S. P. Shah, "Drug delivery to the central nervous system: a review," *J. Pharm. Pharm. Sci. Publ. Can. Soc. Pharm. Sci. Société Can. Sci. Pharm.*, vol. 6, no. 2, pp. 252–273, Aug. 2003.

[195] J. M. Scherrmann, "Drug delivery to brain via the blood-brain barrier," *Vascul. Pharmacol.*, vol. 38, no. 6, pp. 349–354, Jun. 2002.

[196] A. S. Pitek, D. O'Connell, E. Mahon, M. P. Monopoli, F. Baldelli Bombelli, and K. A. Dawson, "Transferrin Coated Nanoparticles: Study of the Bionano Interface in Human Plasma," *PLoS ONE*, vol. 7, no. 7, Jul. 2012.

[197] K. Ulbrich, T. Hekmatara, E. Herbert, and J. Kreuter, "Transferrin- and transferrin-receptor-antibody-modified nanoparticles enable drug delivery across the blood–brain barrier (BBB)," *Eur. J. Pharm. Biopharm.*, vol. 71, no. 2, pp. 251–256, Feb. 2009.

[198] F. Danhier, E. Ansorena, J. M. Silva, R. Coco, A. Le Breton, and V. Préat, "PLGA-based nanoparticles: An overview of biomedical applications," *J. Controlled Release*, vol. 161, no. 2, pp. 505–522, Jul. 2012.

[199] P. Kocbek, N. Obermajer, M. Cegnar, J. Kos, and J. Kristl, "Targeting cancer cells using PLGA nanoparticles surface modified with monoclonal antibody," *J. Controlled Release*, vol. 120, no. 1–2, pp. 18–26, Jul. 2007.

[200] C. Alexiou *et al.*, "Locoregional Cancer Treatment with Magnetic Drug Targeting," *Cancer Res.*, vol. 60, no. 23, pp. 6641–6648, Dec. 2000.

[201] R. K. Jain and T. Stylianopoulos, "Delivering nanomedicine to solid tumors," *Nat. Rev. Clin. Oncol.*, vol. 7, no. 11, pp. 653–664, Nov. 2010.

[202] A. S. Lübbe *et al.*, "Clinical experiences with magnetic drug targeting: a phase I study with 4'-epidoxorubicin in 14 patients with advanced solid tumors," *Cancer Res.*, vol. 56, no. 20, pp. 4686–4693, Oct. 1996.

[203] M. J. Glantz, A. Van Horn, R. Fisher, and M. C. Chamberlain, "Route of intracerebrospinal fluid chemotherapy administration and efficacy of therapy in neoplastic meningitis," *Cancer*, vol. 116, no. 8, pp. 1947–1952, Apr. 2010.

[204] H.-J. Stemmler *et al.*, "Intrathecal trastuzumab (Herceptin) and methotrexate for meningeal carcinomatosis in HER2-overexpressing metastatic breast cancer: a case report," *Anticancer. Drugs*, vol. 19, no. 8, pp. 832–836, Sep. 2008.

[205] R. D. Penn, "Intrathecal baclofen for spasticity of spinal origin: seven years of experience," *J. Neurosurg.*, vol. 77, no. 2, pp. 236–240, Aug. 1992.

[206] J. A. Paice, W. Winkelmüller, K. Burchiel, G. B. Racz, and J. P. Prager, "Clinical realities and economic considerations: Efficacy of intrathecal pain therapy," *J. Pain Symptom Manage.*, vol. 14, no. 3, pp. S14–S26, Sep. 1997.

[207] A. Shahriari and M. Khooshideh, "Intrathecal fentanyl added to lidocaine for Cesarean delivery under spinal anesthesia--a randomised clinical trial," *Middle East J. Anaesthesiol.*, vol. 19, no. 2, pp. 397–406, Jun. 2007.

[208] Y. Jun, J.-H. Lee, and J. Cheon, "Chemical design of nanoparticle probes for high-performance magnetic resonance imaging," *Angew. Chem. Int. Ed Engl.*, vol. 47, no. 28, pp. 5122–5135, 2008.

[209] H. B. Na, I. C. Song, and T. Hyeon, "Inorganic Nanoparticles for MRI Contrast Agents," *Adv. Mater.*, vol. 21, no. 21, pp. 2133–2148, Jun. 2009.

[210] O. Algin, O. Taskapilioglu, E. Zan, B. Hakyemez, and M. Karaoglanoglu, "Detection of CSF leaks with magnetic resonance imaging in intracranial hypotension syndrome," *J. Neuroradiol. J. Neuroradiol.*, vol. 38, no. 3, pp. 175–177, Jul. 2011.

[211] B. T. Farrell *et al.*, "Using iron oxide nanoparticles to diagnose CNS inflammatory diseases and PCNSL," *Neurology*, vol. 81, no. 3, pp. 256–263, Jul. 2013.

[212] E. A. Nance *et al.*, "A dense poly(ethylene glycol) coating improves penetration of large polymeric nanoparticles within brain tissue," *Sci. Transl. Med.*, vol. 4, no. 149, p. 149ra119, Aug. 2012.

[213] J. J. Iliff *et al.*, "A paravascular pathway facilitates CSF flow through the brain parenchyma and the clearance of interstitial solutes, including amyloid β," *Sci. Transl. Med.*, vol. 4, no. 147, p. 147ra111, Aug. 2012.

[214] P. R. Band, J. F. Holland, J. Bernard, M. Weil, M. Walker, and D. Rall, "Treatment of central nervous system leukemia with intrathecal cytosine arabinoside," *Cancer*, vol. 32, no. 4, pp. 744–748, Oct. 1973.

[215] R. D. Penn, "Intrathecal medication delivery," *Neurosurg. Clin. N. Am.*, vol. 14, no. 3, pp. 381–387, Jul. 2003.

[216] N. Bani-hashem, B. Hassan-nasab, E. A. Pour, P. A. Maleh, A. Nabavi, and A. Jabbari, "Addition of intrathecal Dexamethasone to Bupivacaine for spinal anesthesia in orthopedic surgery," *Saudi J. Anaesth.*, vol. 5, no. 4, pp. 382–386, 2011.

[217] M.-C. Luo *et al.*, "An efficient intrathecal delivery of small interfering RNA to the spinal cord and peripheral neurons," *Mol. Pain*, vol. 1, p. 29, Sep. 2005.

[218] V. L. Ghafoor, M. Epshteyn, G. H. Carlson, D. M. Terhaar, O. Charry, and P. K. Phelps, "Intrathecal drug therapy for long-term pain management," *Am. J. Health-Syst. Pharm. AJHP Off. J. Am. Soc. Health-Syst. Pharm.*, vol. 64, no. 23, pp. 2447–2461, Dec. 2007.

[219] B. M. Onofrio and T. L. Yaksh, "Long-term pain relief produced by intrathecal morphine infusion in 53 patients," *J. Neurosurg.*, vol. 72, no. 2, pp. 200–209, Feb. 1990.

[220] C. Alexiou, R. Jurgons, C. Seliger, O. Brunke, H. Iro, and S. Odenbach, "Delivery of superparamagnetic nanoparticles for local chemotherapy after intraarterial infusion and magnetic drug targeting," *Anticancer Res.*, vol. 27, no. 4A, pp. 2019–2022, Aug. 2007.

[221] M. G. Krukemeyer, W. Wagner, M. Jakobs, and V. Krenn, "Tumor regression by means of magnetic drug targeting," *Nanomed.*, vol. 4, no. 8, pp. 875–882, Dec. 2009.

[222] M. Mandal *et al.*, "Magnetite nanoparticles with tunable gold or silver shell," *J. Colloid Interface Sci.*, vol. 286, no. 1, pp. 187–194, Jun. 2005.

[223] Y. Zhang, N. Kohler, and M. Zhang, "Surface modification of superparamagnetic magnetite nanoparticles and their intracellular uptake," *Biomaterials*, vol. 23, no. 7, pp. 1553–1561, 2002.

[224] H. W. Stockman, "Effect of Anatomical Fine Structure on the Dispersion of Solutes in the Spinal Subarachnoid Space," *J. Biomech. Eng.*, vol. 129, no. 5, p. 666, 2007.

[225] Y. Hsu, H. D. M. Hettiarachchi, D. C. Zhu, and A. A. Linninger, "The frequency and magnitude of cerebrospinal fluid pulsations influence intrathecal drug distribution: key factors for interpatient variability," *Anesth. Analg.*, vol. 115, no. 2, pp. 386–394, Aug. 2012.

[226] M. C. Henry-Feugeas, I. Idy-Peretti, B. Blanchet, D. Hassine, G. Zannoli, and E. Schouman-Claeys, "Temporal and spatial assessment of normal cerebrospinal fluid dynamics with MR imaging," *Magn. Reson. Imaging*, vol. 11, no. 8, pp. 1107–1118, Jan. 1993.

[227] L. Laitinen, "Origin of Arterial Pulsation of Cerebrospinal Fluid," *Acta Neurol. Scand.*, vol. 44, no. 2, pp. 168–176, May 1968.

[228] B. Polyak *et al.*, "High field gradient targeting of magnetic nanoparticle-loaded endothelial cells to the surfaces of steel stents," *Proc. Natl. Acad. Sci. U. S. A.*, vol. 105, no. 2, pp. 698–703, Jan. 2008.

[229] C. Alexiou *et al.*, "A High Field Gradient Magnet for Magnetic Drug Targeting," *IEEE Trans. Appl. Supercond.*, vol. 16, no. 2, pp. 1527–1530, Jun. 2006.

[230] I. Mohammed and A. Hussain, "Intrathecal baclofen withdrawal syndrome- a life-threatening complication of baclofen pump: a case report," *BMC Clin. Pharmacol.*, vol. 4, p. 6, Aug. 2004.

[231] L. W. Kao, Y. Amin, M. A. Kirk, and M. S. Turner, "Intrathecal baclofen withdrawal mimicking sepsis," *J. Emerg. Med.*, vol. 24, no. 4, pp. 423–427, May 2003.

[232] J. Bardutzky, V. Tronnier, S. Schwab, and H.-M. Meinck, "Intrathecal baclofen for stiff-person syndrome: life-threatening intermittent catheter leakage," *Neurology*, vol. 60, no. 12, pp. 1976–1978, Jun. 2003.

[233] K. W. Shirley, S. Kothare, J. H. Piatt, and T. A. Adirim, "Intrathecal baclofen overdose and withdrawal," *Pediatr. Emerg. Care*, vol. 22, no. 4, pp. 258–261, Apr. 2006.

[234] H. E. Perry, R. O. Wright, M. W. Shannon, and A. D. Woolf, "Baclofen overdose: drug experimentation in a group of adolescents," *Pediatrics*, vol. 101, no. 6, pp. 1045–1048, Jun. 1998.

[235] W. J. Dawes, J. M. Drake, and D. Fehlings, "Microfracture of a baclofen pump catheter with intermittent under- and overdose," *Pediatr. Neurosurg.*, vol. 39, no. 3, pp. 144–148, Sep. 2003.

[236] Y. Tunali, H. Hanimoglu, T. Tanriverdi, L. Hanci, and M. Hanci, "Intrathecal Baclofen Toxicity and Deep Coma in Minutes," *J. Spinal Cord Med.*, vol. 29, no. 3, pp. 237–239, 2006.

[237] D. Sharma, "A biologically friendly single step method for gold nanoparticle formation," *Colloids Surf. B Biointerfaces*, vol. 85, no. 2, pp. 330–337, Jul. 2011.

[238] I. M. Banat, R. S. Makkar, and S. S. Cameotra, "Potential commercial applications of microbial surfactants," *Appl. Microbiol. Biotechnol.*, vol. 53, no. 5, pp. 495–508, May 2000.

[239] R. Weissleder *et al.*, "Superparamagnetic iron oxide: pharmacokinetics and toxicity," *AJR Am. J. Roentgenol.*, vol. 152, no. 1, pp. 167–173, Jan. 1989.

[240] C. Lasagna-Reeves *et al.*, "Bioaccumulation and toxicity of gold nanoparticles after repeated administration in mice," *Biochem. Biophys. Res. Commun.*, vol. 393, no. 4, pp. 649–655, Mar. 2010.

[241] A. Tomkins, "Assessing micronutrient status in the presence of inflammation," *J. Nutr.*, vol. 133, no. 5 Suppl 2, p. 1649S–1655S, May 2003.

**APPENDIX A- INTRATHECAL MAGNETIC DRUG TARGETING USING GOLD COATED MAGNETITE NANOPARTICLES IN A HUMAN SPINE MODEL**

(Previously published as Lueshen, E., Venugopal, I., Kanikunnel, J., Soni, T., Alaraj, A., and Linninger, A. (2014) Intrathecal magnetic drug targeting using gold-coated magnetite nanoparticles in a human spine model, Nanomedicine 9(8), 1155-1169.)

## A.1. Summary

To test the feasibility of the proposed intrathecal magnetic drug targeting technique, our lab developed a physiologically and anatomically consistent *in vitro* human spine model. Gold-coated magnetite nanoparticles are infused into the model and targeted to specific regions using external magnetic fields. Experiments and simulations aiming to determine the effect of key parameters such as magnet strength, duration of magnetic field exposure, magnet location, and ferrous implants on the collection efficiency of superparamagnetic nanoparticles in targeted regions were performed. The experimental results aid in understanding nanoparticle distribution and retention in different intrathecal regions guided by magnetic fields. Our experiments indicate that IT-MDT is a promising technique for concentrating and localizing drugs at targeted sites within the spinal canal for treating diseases affecting the CNS.

## A.2. Introduction

Intrathecal drug delivery is a standard technique involving direct injection of drugs into the CSF surrounding the brain and the spinal cord. It has been a standard treatment for different CNS disorders such as leptomeningeal metastases ([203], [204], [214]) and spasticity [215], and has been widely used for pain management [206] and in spinal anesthesia ([207], [216]). Recent attempts even aim at using intrathecally delivered siRNA

to treat diseases of the CNS ([83], [217]). Once injected, the drugs are rapidly dispersed within the spinal canal by both molecular diffusion and by pulsatile motion of CSF [83].

To maximize the therapeutic effect without excessive risk of toxicity in non-targeted zones, the intrathecally injected drugs should be concentrated at specific locations within the spinal canal. For example, in pain management therapies morphine needs to reach specific receptor sites located on the dorsal horns of the spinal cord to elicit an analgesic effect ([215], [218], [219]). In the case of IT morphine administration, the drug molecules need to transport across the pia mater and then diffuse through spinal cord tissue to reach the dorsal horns. Intrathecally administered therapeutics for chemotherapy also have small local targets in which similar transport processes are necessary to cross the ependymal surfaces in the spinal canal and then diffuse to the desired site of action. Such issues are currently overcome by using high drug doses so that the required concentration reaches the target region to aid diffusion into the spinal cord and produce a therapeutic effect. Due to CSF pulsations, as well as the presence of nerve roots and trabeculae which enhance mixing, these high drug concentrations are rapidly spread throughout the entire CNS. At this point, there is no way to deliver the drug locally, where it is needed in high concentrations, without having large amounts of drug spread throughout the entire brain and spinal canal, which may cause side effects.

We have recently shown that pulsatile CSF motion causes intense mixing of intrathecally delivered drugs [83]. Even though CSF flow within the spinal canal has a small Reynolds number, there is still vivid fluid exchange because the fluid laminae are intertwined due to CSF pulsations. In this chapter, we present a novel approach of using magnetically guided nanoparticles, which are capable of being functionalized with different

types of drugs, for localizing and concentrating the particles at specific locations in an *in vitro* model of the human spine. Our results indicate that superparamagnetic gold coated magnetite nanoparticles can be preferentially confined within an area of interest by guiding the particles with an external magnetic field. We have also provided computational results which aided in determining the optimal magnetic field for efficient IT-MDT. If this novel technique can be successfully utilized with the required drug conjugated to the nanoparticles, the drugs can be locally delivered within the spinal canal at high concentrations, minimizing unwanted side effects of the drug away from the target region.

Our approach builds on the methods of magnetic drug targeting. MDT is a type of active drug targeting method in which drug-functionalized MNPs are injected into the body and then localized to the target region by use of an external magnetic field. The drug will then desorb from the MNPs and begin its therapeutic mechanism of action. The most notable benefits of MDT reside in local drug action and minimization of systemic side effects. Until now, MDT methods have been mainly used to target drugs delivered systemically through blood vessels and have shown great promise ([21], [220], [221]). The novelty of our approach lies in applying the methods of MDT within the CSF filled spinal canal, not in blood vessels, to achieve a localized therapeutic effect using much smaller drug doses and reducing systemic toxicity for novel treatments of CNS diseases.

This chapter is organized as follows. Nanoparticle synthesis is presented first, followed by a description of our *in vitro* human spine model and experimental setup. Computer simulations to determine the optimal magnetic field for IT-MDT are then discussed, as well as a description of our experimental procedure used to measure the MNP collection efficiency. The results section presents the MNP characterization and the

outcomes from our three different sets of experiments which were performed to determine MNP collection efficiency within each spinal zone as a function of either the strength of the applied external magnet, the duration of magnetic field exposure, or the distance between the target location and the site of nanoparticle injection. Preliminary results from experiments in which the targeting magnet was placed at a physiological distance away from the spinal canal on top of the epidermis, as well as some implant assisted IT-MDT experiments, are also presented. The chapter closes with a discussion of our experimental results and conclusions.

## A.3.    Materials and Methods

In all our experiments, we used externally placed permanent magnets to target superparamagnetic gold coated magnetite nanoparticles at specific locations within an *in vitro* model of the human spine. The main aim of these experiments was to systematically study the spatial distribution of the MNPs in the presence of static magnetic fields within the intrathecal space, and to investigate the possibility of localizing and concentrating the nanoparticles at different regions within the human spine model. In this section, we explain (i) the materials and methods used for nanoparticle synthesis, (ii) our *in vitro* human spine model, (iii) the simulations used to determine optimal magnetic fields, and (iv) our experimental procedure to determine MNP collection efficiency.

### A.3.1.  Synthesis of Gold Coated Magnetite Nanoparticles ($Fe_3O_4$@Au MNPs)

The nanoparticles utilized for all our experiments had a magnetite core with diameter varying between 8-12 nm as shown in Figure 43A. Magnetite cores within this diameter range are beneficial because they display the property of superparamagnetism, which means they exhibit net magnetization only in the presence of an external magnetic

120

field. Superparamagnetism allows MNPs to transport freely throughout the spine model until they are in the presence of the externally applied magnetic field, which then acts to trap the MNPs at that defined location. Once the applied magnetic field is removed, these superparamagnetic nanoparticles lose their previously induced magnetization and re-disperse in the fluid. The nanoparticle cores were synthesized by a coprecipitation technique, described in Mandal and colleagues (2005) and various other articles, using ferrous and ferric salts to form magnetite [222]. These superparamagnetic magnetite cores were then coated by a gold layer of thickness varying between 8-15 nm by a surface adsorption technique. The overall hydrodynamic diameter of the particles was found to be between 20-25 nm as shown in Figure 43B. The gold coating on the magnetite served two purposes. (i) It prevented oxidation of the magnetite core into maghemite by forming an inert biocompatible protective coating. (ii) It also forms an excellent platform for conjugating drugs to the nanoparticle surface since gold has a natural affinity for thiol bonds [223]. These particles were suspended in a TX-100 surfactant solution to introduce micelles and help prevent agglomeration. The nanoparticles were characterized by using transmission electron microscopy (TEM), energy dispersive x-ray spectroscopy (EDS) and superconducting quantum interference device (SQUID) magnetometry.

### A.3.2. *In Vitro* Human Spine Model

An *in vitro* model of the human spine was built to conduct MDT experiments to help determine the feasibility of IT-MDT. It was important that the model possessed physiologically and anatomically consistent dimensions to conserve the main hydrodynamic properties of CSF which are crucial to intrathecal drug delivery in humans.

These essential components include the spinal canal, spinal cord, nerve roots, filum terminale, as well as the ability of the CSF to pulsate.
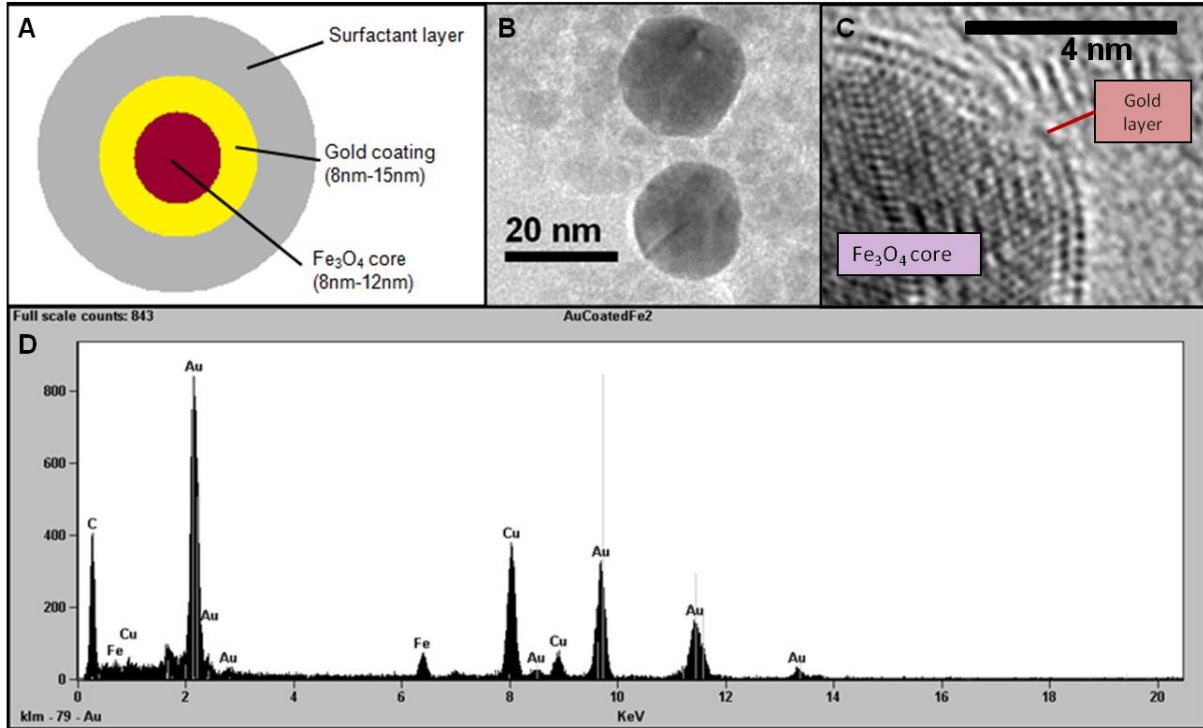


Figure 43. (A) Schematic of $Fe_3O_4$@Au nanoparticle (B) TEM image of nanoparticles showing hydrodynamic diameter to be between 20-25 nm (C) TEM image showing a partially gold coated $Fe_3O_4$ core which confirms the core diameter to be around 8-12 nm (D) The energy density spectrum of $Fe_3O_4$@Au nanoparticles determined using EDS indicates the presence of elements Au, Fe and O.

The model, as shown in Figure 44, consisted of a cylindrical polystyrene tube (49 cm length; 1.52 cm inner diameter) which represented the spinal canal and a cylindrical section of pressure-treated hard wood at the center of the tube which served as a surrogate for the spinal cord. Black rubber pieces (2 mm in diameter) were used to represent spinal nerve roots located above the cauda equina which are important in enhancing the mixing of intrathecally injected nanoparticles [224]. A latex deformable membrane was tightly fixed to the mouth of the distal neck and served as the filum terminale which expands and

contracts during the pulsatile motion of fluid inside the model. The void volume, which

served as the subarachnoid space (SAS), was filled with artificial CSF.
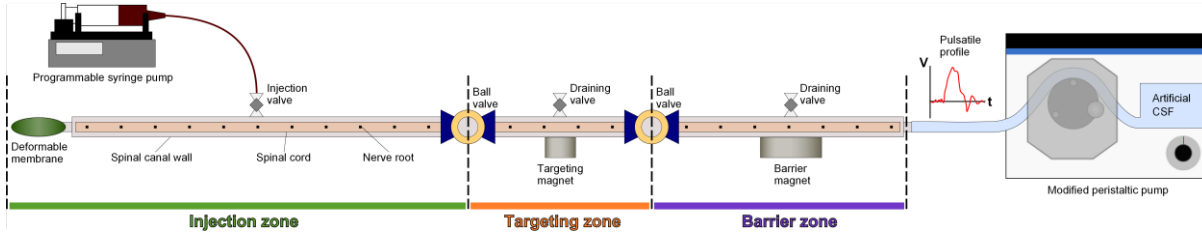


Figure 44. Schematic of entire experimental setup with the *in vitro* human spine model which clearly shows the three different zones (injection, targeting, and barrier zones).

IT drug distribution varies depending on different patient specific parameters such as the frequency and magnitude of CSF pulsations, the velocity and stroke volume of CSF, and heart rate [225]. Previous research has shown CSF flow velocities varying from 0.3-5.1 cm/s and CSF stroke volumes varying from 0.1-3.0 mL/s depending on a patient's health, spinal anatomy, heart rate, and blood pressure ([116], [226]). In our experiments a CSF velocity of 1.5 cm/s and a stroke volume of 2 mL were imposed, which are within the ranges cited previously. To produce pulsatile fluid motion equal in amplitude and frequency to that of a typical resting human's CSF pulsations, the proximal end of the model was connected to a peristaltic pump and two of the three metal cylinders that drive the pump were removed. This created a ramping pulse function. Since CSF pulsates at a frequency of the heart beat [227], the pump was set at 72 beats per minute (bpm) which, according to the American Heart Association, is within the 60-80 bpm range of normal resting heart rate in humans. The inclusion of pulsatile fluid motion and spinal nerve roots in our model was important because of the large effects these two parameters have on CSF fluid mechanics as seen *in vivo*.

For controlled nanoparticle injection into the model, a programmable syringe pump was used. The BD 15 mL syringe was connected to the model via a plastic catheter which allowed for controlled infusion of nanoparticles into the spinal canal. Nanoparticle injections always occurred in the lumbar region of our model.

Nanoparticles were targeted to a specific site in the spine model by using an external magnetic field (targeting magnet) placed exactly below the region of interest. This field was produced in our system by using Neodynium-Iron-Boron (NdFeB) rare earth magnets (K&J Magnetics, Inc.) of various dimensions, lbs pull force values, and surface field strengths – 0.396 T (3960 gauss), 0.507 T (5070 gauss), 0.528 T (5280 gauss) and 1.05 T (10,500 gauss). As depicted in Figure 44, magnetic fields were applied along the spinal canal at two specific locations: target site (middle of apparatus) and barrier site (right end of apparatus). The target site was located at the treatment area where nanoparticles should by concentrated. The barrier site magnet was placed to prevent the small fraction of nanoparticles escaping the target site from exiting the model. Ball valves were used to separate the spine model and its contained fluid into three different zones: injection, targeting, and barrier zones (Figure 44). To determine the mass fraction of nanoparticles retained by the magnet within the target region and the remaining nanoparticles in the other two zones, the ball valves were closed and the fluid contained within each zone was eluted through individual draining valves, dried, and weighed.

### A.3.3. Multiphysics Simulation-Based Determination of Optimum Magnetic Field

COMSOL 4.2a, an engineering, design, and finite element analysis software environment for the modeling and simulation of any physics-based system, was used to study the magnetic fields produced by different permanent magnets and to design

appropriate fields with these magnets for use in our experiments. Figure 45 and 46 display the magnetic fields produced by the simulations, which match the fields produced by the magnets used for the *in vitro* IT-MDT experiments. Specifically, Figure 45A shows the magnetic field lines of our *in vitro* spine model with the exact magnets used experimentally, while Figure 45B displays the magnetic field lines when both the targeting and barrier magnets have the same dimensions and strength. Figure 46 shows the magnetic fields present around both the targeting magnet and barrier magnet in our model. From the inserts displayed in Figure 46, one can see that the strength of the magnetic field in the CSF-filled SAS opposite the targeting magnet is in the range of 0.051-0.098 T, while the strength of B-field in the SAS opposite the barrier magnet is in the range of 0.092-0.167 T. Both magnetic field strength ranges were shown to be strong enough to capture MNPs while overcoming the pulsatile motion and mixing of the CSF.

### A.3.4. Experimental Procedure to Determine MNP Collection Efficiency

All experiments were conducted by injecting 1 mL of 0.017 g/mL $Fe_3O_4$@Au nanoparticle solution into the *in vitro* human spine model in the lumbar region using a programmable syringe pump over 1 minute. The surface field strength of the barrier magnet used was 1.05 T. The strength of the target magnet varied depending on the experiment under consideration. Once the experiments were completed, each compartment — corresponding to a particular zone — was rinsed separately and magnetically decanted. The solutions collected were placed in a convection oven and heated for 1 hour at (175°C) until completely dry to determine the dry weight of these fractions. The fraction of nanoparticles collected within each zone was used to determine the overall collection efficiency (CE) of each experiment trial.
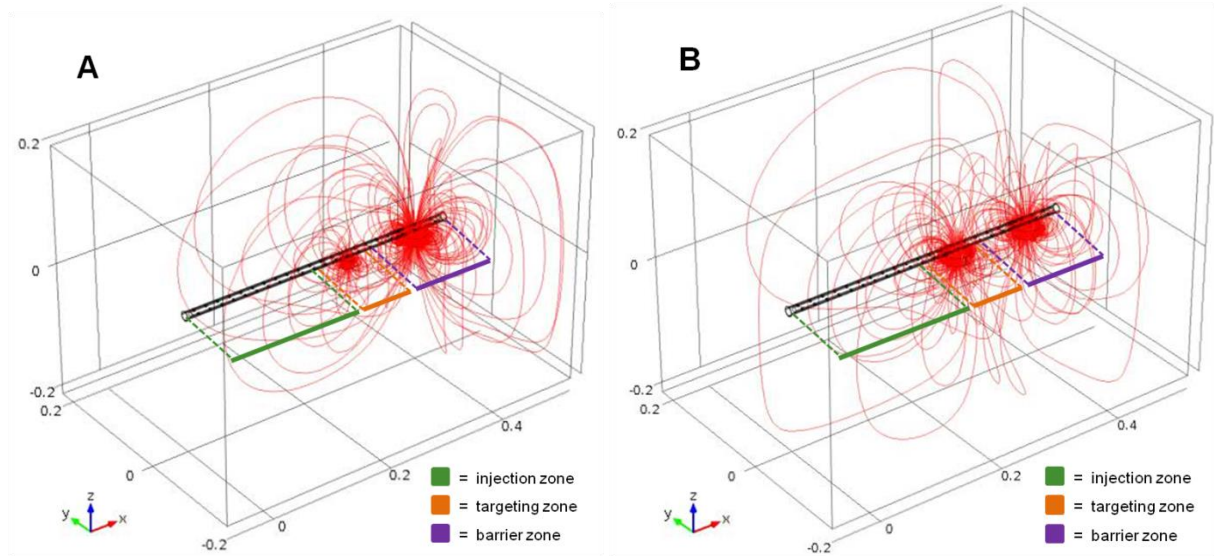
Figure 45. Magnetic field lines produced by (A) *in vitro* human spine model with the 0.528 T targeting magnet and the 1.05 T barrier magnet and by (B) spine model in which both magnets are of 1.05 T surface field strength.

Three sets of experiments were performed to determine the nanoparticle CE in each zone depending on either the strength of the applied external magnet, time duration of magnetic field exposure, or distance between target location and site of nanoparticle solution injection. Additional preliminary experiments to determine the



Figure 46. Magnetic field produced by targeting magnet and barrier magnet (shown in xz-plane). Subarachnoid space opposite the targeting magnet experiences a magnetic field in the range of 0.051-0.098 T , while the subarachnoid space opposite the barrier magnet experiences a B field in the range of 0.092-0.167 T.

effect of a 4 cm physiological distance between the spinal canal and the magnet located on the skin surface, as well as the effect of ferrous implants, on the nanoparticle CE were also performed.

126

## A.4. RESULTS

### A.4.1. Nanoparticle Characterization

The nanoparticles were characterized by TEM and EDS at the University of Illinois at Chicago (UIC) Research Resources Center, as well as by SQUID magnetometry at Northwestern University. The TEM images confirmed the size of both our magnetite core to be about 8-12 nm and the entire gold-coated magnetite nanoparticle to be between 20-25 nm. These TEM results, along with the SQUID magnetometer results shown in Figure 7, confirmed that our nanoparticles were superparamagnetic which helped prevent agglomeration in the absence of an external magnetic field. From the plot of magnetization vs. applied magnetic field
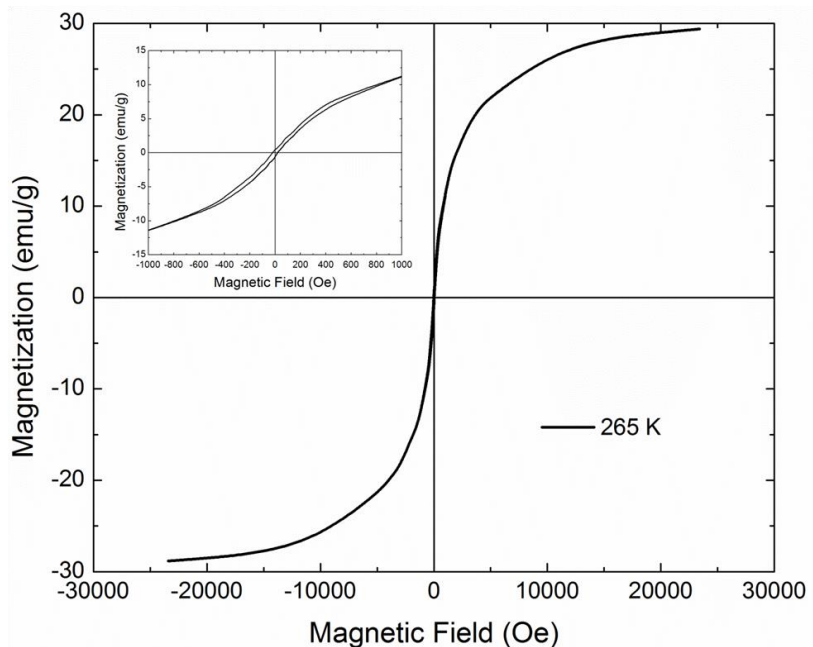
Figure 47. Plot of magnetization vs. magnetic field, obtained by SQUID magnetometry, for the $Fe_3O_4$@Au magnetic nanoparticles used in our *in vitro* intrathecal magnetic drug targeting experiments.

(M-H loop) at 265 K (Figure 47), the saturation magnetization ($M_s$), remnant magnetization ($M_r$), and coercivity ($H_c$) were determined for our $Fe_3O_4$@Au nanoparticles to be as follows: $M_s$ = 29.5 emu/g; $M_r$ = 0.52 emu/g; $H_c$ = 21.1 Oe at 265 K. The EDS results indicated the presence of gold (Au), iron (Fe) and oxygen (O) in our nanoparticle sample.

Disregarding the other elements present from in EDS sample grid (C and Cu), we validated the presence of both Au and $Fe_3O_4$ in our nanoparticle samples.

## A.4.2. Collection Efficiency as a Function of Magnet Strength

To prove the hypothesis that stronger magnets achieve more efficient MNP retention, we performed experiments in which the magnet strength in the targeting zone was varied. Based on the results from our simulations of magnetic field gradients and field strengths produced by magnets of differing size and composition, NdFeB magnets with surface field strengths of 0.396 T, 0.507 T, and 0.528 T were selected for use in the targeting zone. These magnets were shown to have magnetic field gradients and strengths within the SAS of our human spine model capable of confining the bulk of the nanoparticle transport within the target region. Experimental run times (duration for which the pulsations were produced after injection) remained fixed at 15 minutes for all the trials. Two different 0.528 T surface field strength magnets, but with differing pull force strengths (35 lb pull force and 1045 lb pull force), were tested as well.

MNP CE within the targeting zone increased as the surface field strength and lb pull force strength of the magnet increased, while the MNP retention simultaneously decreased in both the injection and barrier zones, as can be seen in Figure 48. Percentage retentions of 48%, 62%, 73%, and 98% were observed for the surface magnetic field strengths of 0.396 T, 0.507 T, 0.528 T (35 lb pull force), and 0.528 T (1045 lb pull force) respectively. Note that stronger lbs pull force magnet out of the two 0.528 T surface field strength magnets was able to capture nearly all of the MNPs and showed a 98% CE. Statistical analysis revealed significant differences between the nanoparticle collection efficiencies obtained when any of the different magnet strengths were applied; all p-values were much

smaller than the
0.05 significance
level. These MNP
CEs within the
targeting zone
when a magnetic
field was applied
were greater than
the average CE in
the targeting zone

of control
experiments in
which no



Figure 48. Graph showing the nanoparticle collection efficiency (CE) as a function of magnet strength at the targeting zone. Error bars represent the standard deviation in nanoparticle CE within each zone for the different experiments. With magnetic targeting, the nanoparticle CE increased almost 9-fold when compared to the control experiments.

magnetic field was applied. For example, the 35 lb pull force, 0.528 T surface field strength magnet exhibited a 664% increase in nanoparticle CE within the targeting zone as compared to the control, and the 1045 lb pull force, 0.528 T surface field strength magnet exhibited an astonishing 891% increase in CE.

The CE vs. magnet strength experiments showed that the nanoparticle CE depended on magnitude of the applied external magnetic field, as well as the pull force strength of the magnet, within the targeting zone of the spine model. Although the strongest magnet with 1045 lb pull force strength gave the highest nanoparticle CE of 98% within the targeting zone (Figure 48), its bulky size (4" x 2") may be a disadvantage in future clinical trials. Therefore, the much smaller 35 lb pull force magnet (3/4" x 1/2") was selected as our

target magnet of choice for the remainder of our experiments in which magnet placement was within the epidural space of our model. In future clinical trials of IT-MDT, magnets with different strength, size, and shape may be optimized to fit the needs of patients or the disease being treated.

### A.4.3. Collection Efficiency as a Function of Time

The variation in MNP CE with time at a specific target site within the *in vitro* human spine model was investigated. In these experiments a target magnet of 0.528 T surface field strength and 35 lb pull force strength was used within the targeting zone and experimental times were varied before MNP collection from each zone. Different trials were run for each of these experimental times:  0.5 min, 1 min, 2 min, 5 min, 10 min, 15 min, and 60 min.

The time dependent variations in nanoparticle CE are shown in Figure 49. During the first five minutes of each experiment, a significant portion of the nanoparticles still resided in the injection zone. As each experiment progressed, the nanoparticle recovery from the targeting zone increased due to the transport of nanoparticles into this zone by the pulsatile CSF fluid flow and their subsequent capture by the magnetic field.

It was observed that the CE in the targeting zone increased significantly during the first 15 minutes of these experiments, reaching 73.0% CE. After 15 minutes, MNP capture in the targeting zone was practically completed with a mean CE of 74.1% at 60 minutes (p-value = 0.4085). No significant change in the magnetic retention value was observed beyond 60 minutes. The CE vs. time experiments showed that the nanoparticle collection efficiency at the target site in the spine model increased with time and reached a final steady value around 74%.
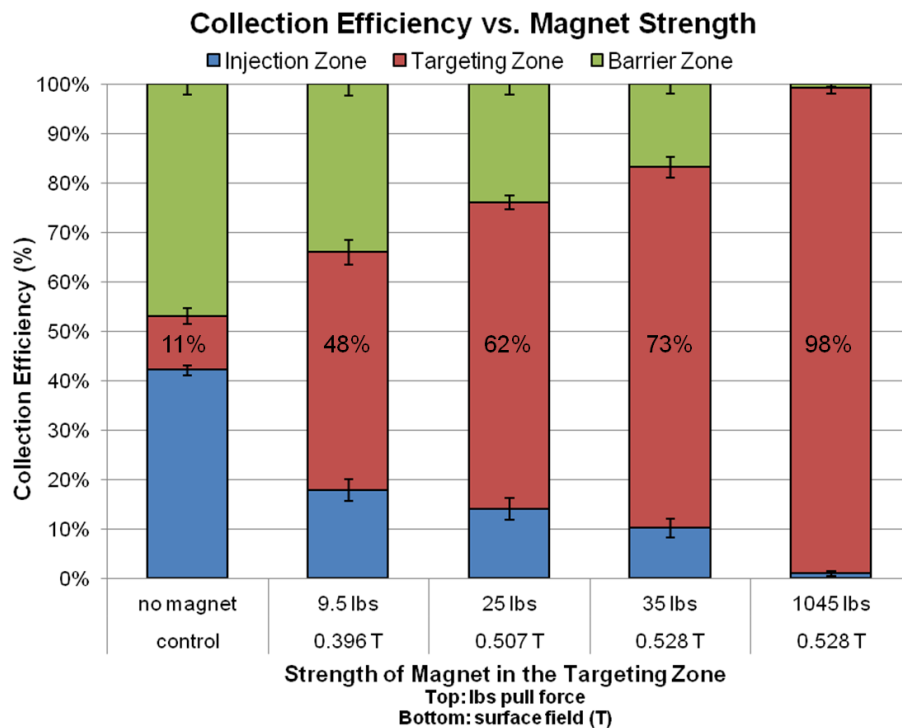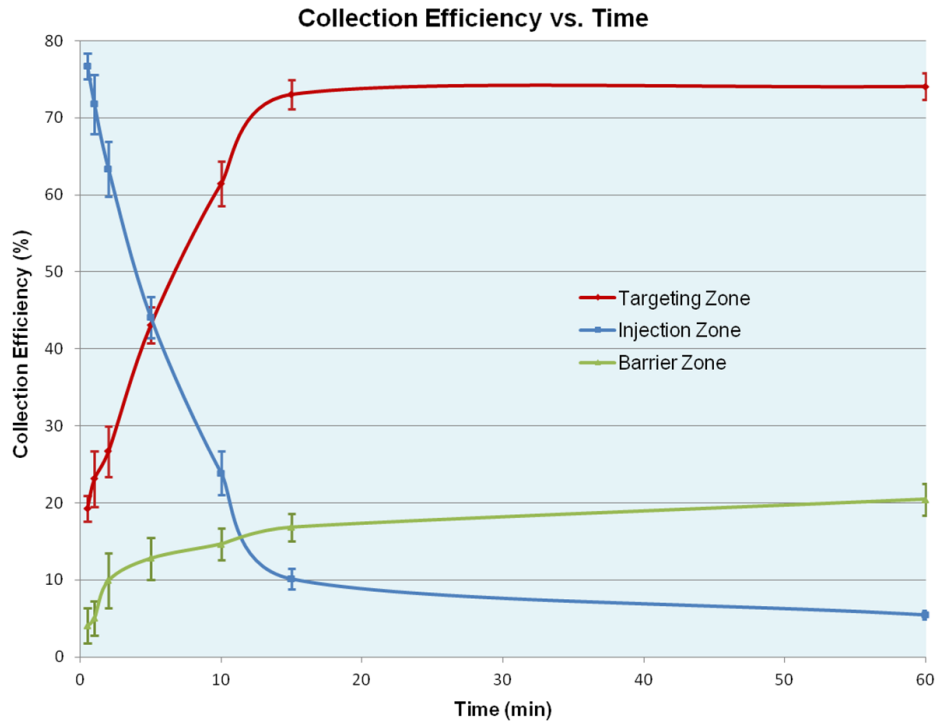
Figure 49. Graph showing the nanoparticle collection efficiency (CE) as a function of time. Error bars represent the standard deviation in nanoparticle CE within each zone at the different measurement times. As CE within the targeting zone increases, CE within both the injection and barrier zones simultaneously decrease.

### A.4.4. Collection Efficiency as a Function of Magnet Location along Spine Model

To test whether any desired region could be effectively targeted with high nanoparticle CE, we performed experiments in which we varied the location of the applied external magnetic field along the spine model. In other words, we varied the physical location of the target zone. While it was expected that only the hydrodynamic drag force and the magnetic force affect nanoparticle collection, it was essential to prove that targeting was possible in any zone with the same level of efficiency for the same magnet. These experiments were also important to demonstrate that surface effects or surface friction from the model acting on the nanoparticles did not significantly impact

131

nanoparticle collection and that gravity effects could be assumed negligible. A target

magnet with 0.528 T surface field strength and 35 lb pull force was placed in the injection

zone (at 3.0 cm from the injection site), targeting zone (at 16.0 cm from the injection

site) and barrier zone (at 26.0 cm from the injection site) during three separate sets of

experiments and experimental run time was maintained at 15 minutes.

In these experiments, maximum retention values between 73% and 75% were

observed at each targeting location within the three different zones. High collection

efficiencies were achieved for nanoparticle localization in the lumbar region ("injection

zone") with 75% CE, thoracic region ("targeting zone") with 73% CE, as well as the cervical region ("barrier zone") with 74% CE. It is important to note that the maximum retention at every zone had little variance (73% - 75%) as shown in Figure 50. Statistical analysis



Figure 50. Graph showing the variation of nanoparticle collection efficiency (CE) at different target zones in the *in vitro* human spine model as a function of the distance of the targeting magnetic field from the injection site. No matter which zone was chosen as the treatment site where the magnet was to be placed (region targeted; displayed in red), CE reached between 73% - 75%. Green and blue colored bars correspond to the non-targeted regions. Note, the different patterns correspond to the three zones; diagonal brick pattern = "injection zone"; square pattern = "targeting zone"; horizontal wave pattern = "barrier zone".

revealed no significant differences between the MNP collection efficiencies obtained at any

of the target magnet locations along the spine model: 3 cm vs. 16 cm (p = 0.3429), 16 cm vs. 26 cm (p-value = 0.4128), and 3 cm vs. 26 cm (p = 0.6985).

The CE vs. distance of targeting magnet field from injection site experiments showed that the position of the applied magnetic field always yielded high nanoparticle retention irrespective of its distance from the injection site. To determine if the MNPs leaving the spine model from the barrier zone due to pulsations was significant, Prussian blue staining (used for indicating the presence of iron) was performed on the solution leaving the model. The test showed that MNPs that escaped the magnetic barrier was negligible.

### A.4.5. Magnetic Guidance at Physiological Distance & Implant-Assisted Guidance

The previous experiments used permanent magnets placed in the epidural space of the *in vitro* human spine model. To test whether effective IT-MDT could be achieved at physiological distances, meaning the distance between spinal canal and the epidermis (as shown in Figure 51A), we conducted additional experiments with a 4 cm void space between the targeting magnet and the *in vitro* human spine model. This distance is equivalent to placing magnets non-invasively on the surface of a patient's back when performing IT-MDT clinically. Two different sets of experiments were conducted; one set with only the 4 cm physiological separation; the other set with the 4 cm separation and inclusion of two ferrous implants within the epidural space of the model. Both sets of experiments used 0.528 T surface field strength, 1045 lb pull force strength magnet in order to achieve a strong magnetic field at a physiological distance from the magnet.

In the first set of experiments with only 4 cm physiological separation, an average nanoparticle CE of 52% was obtained within the targeting zone during both 15- and 60-minute trials. These results are a 473% increase (nearly 5-fold increase) in MNP

133

collection efficiency when compared to the control where no magnetic field was applied. The magnetic field simulations indicated that the field within the spinal canal dropped to a range of 0.116-0.160 T (Figure 51C) from the previous range of 0.068-0.332 T (Figure 51B) obtained during experiments in which the smaller 0.528 T surface field strength, 35 lb pull force strength magnet was placed within the epidural space of the spine model. Along with this reduction in field strength, simulations also showed that the magnetic field within the spinal canal had smaller gradients when the magnet was placed at a 4 cm physiological distance away from the model compared to when the targeting magnet was placed within the epidural space. This computed drop in magnetic field strength and magnetic field gradient is consistent with the experimental results of a 52% MNP CE compared to the 73% CE obtained in previous experiments with magnet placement within the epidural space.

In the second set of experiments, two cylindrical ferrous implants (1/8" diameter x 3" length) were placed within the epidural space of the model, one dorsal implant and one ventral implant, while maintaining the magnet placement at a physiological 4 cm distance. This preliminary test mimics the effect of implant-assisted MDT, which aims to create a high gradient magnetic field to obtain larger nanoparticle retention values.

The results from these implant-assisted IT-MDT experiments showed an average nanoparticle CE of around 76% within the targeting zone during both 15- and 60-minute experiments. The implant-assisted IT-MDT results produced a 146% increase in MNP CE over the IT-MDT experiments which only had the physiological separation and no implant; a highly efficient 691% increase over the control experiments.
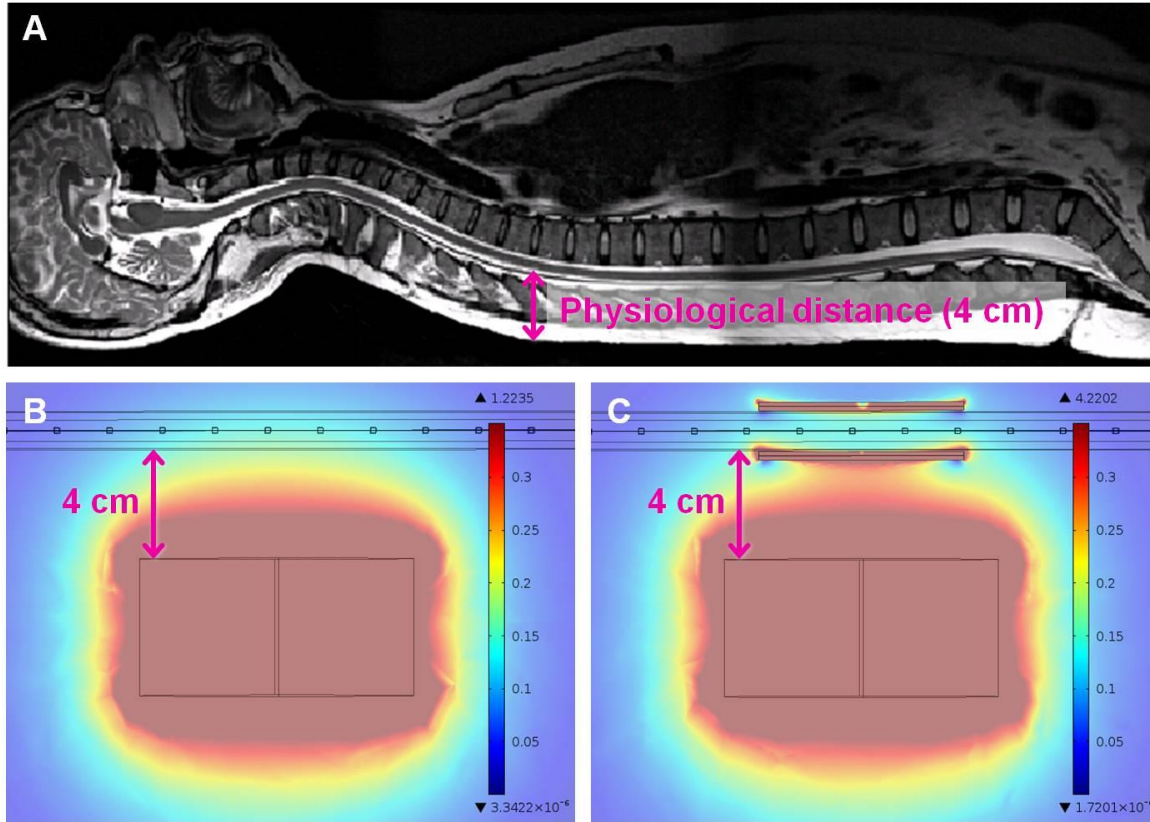
Figure 51 (A) Patient MRI showing the 4 cm physiological distance between intrathecal space and epidermis (B) Simulated magnetic field $\vec{B}$ produced by the 0.528 T surface field, 1045 lb pull force strength magnet placed at a 4 cm distance away from the spinal canal; magnetic field within the spinal canal is within a 0.116-0.160 T range (C) Simulated $\vec{B}$ field when two ferrous implants were placed within epidural space; high gradient magnetic field created within the spinal canal is within a 0.067-0.626 T range.

As shown in Figure 51C, the ferrous implants concentrated the magnetic flux density ($\vec{B}$ field) around the spinal canal, which created a high gradient field (0.067-0.626 T) within the SAS. Due to the high gradient field, large nanoparticle collection efficiencies were obtained, like those obtained when 35 lb pull force targeting magnet was placed within the epidural space and no implants were present.

## A.5.   Discussion

Our experiments confirm that IT-MDT can be controlled using three critical parameters: *targeting magnet strength, magnet placement along the spinal canal, and*

*magnetic field gradient*. The experiments with varying targeting magnet strength showed that an increase in the surface field enhanced MNP retention within the targeting zone with collection efficiencies up to 9-times greater than control. During these experiments, we observed that the MNPs preferentially collected towards the edges of the magnet surface (regions with largest field gradients). This preference emphasizes the importance of generating high gradient magnetic fields in MDT applications ([228], [229]). Our implant-assisted IT-MDT experiments confirm that a high gradient magnetic field is desirable within the targeting region to achieve the highest concentration of drug-functionalized MNPs.

When the targeting magnet location was varied along the *in vitro* spine model, position of the applied magnetic field always yielded high MNP retention regardless of its distance from the injection site. Therefore, very high MNP concentrations can be attained at any desired targeting location within the spinal canal. This is a significant point to consider when developing personalized treatment therapies for future patients. Our CE vs. time experiments established that MNP targeting and settlement reached final values within 15 minutes when experiments were conducted using the spinal canal dimensions and CSF pulsation parameters. For different dimensions and pulsation parameters, the duration of magnetic targeting and nanoparticle settlement is expected to vary. Our recent studies quantify how the frequency and magnitude of a patient's CSF pulsations influence intrathecal drug distribution [225]. Accordingly, slight deviations from the suggested 15 minute MNP targeting and settlement time can be expected for different parameters. However, the relatively short duration of magnetic targeting may be advantageous for future clinical applications of IT-MDT.

Also, another result crucial for developing personalized therapies is that high CE can be achieved when placing a strong magnet at a distance equal to the physiological separation between a patient's spinal canal and epidermis, either with or without a ferrous spinal implant.

Our envisioned therapy for CNS disorders consists of delivering and localizing MNPs, which would be conjugated to the required drugs, to specific regions within the spinal canal using an external magnetic field, followed by controlled release of the drug for desired treatment. For example, while treating leptomeningeal metastases or other CNS tumors where the chemotherapeutic drug needs to be concentrated near the site of cancerous cell proliferation, we could conjugate the nanoparticles to a drug such as methotrexate and then guide them to the required treatment location using an external magnetic field [220]. IT-MDT may also be a treatment option for IT gene therapies where only a localized effect is desired.

In regards to personalized therapies, IT-MDT shows great promise since large MNP collection efficiencies are possible within a short duration (only 15 minutes) regardless of the targeting location. The specific site within the spinal canal, as well as the amount of drug to be delivered to the site, would determine the placement of the external magnetic field and its strength for personalized treatment. IT-MDT has clear advantages for targeted drug delivery in very high concentrations with the potential to greatly diminish systemic toxicity while using much smaller drug doses as compared to standard IT drug infusion protocols in which continuous infusion is required for maintaining a sufficiently high drug concentration at the target site despite dispersion throughout the entire CNS.

For example, during standard IT baclofen infusions, the drug is continuously administered at rates of 100-900 μg/day ([230], [231]). We hypothesize that a much smaller dose of baclofen would be required using our magnetically targeted intrathecal treatment since most of the infused drug-functionalized MNPs would be confined to the desired treatment area. Although continuous intrathecal baclofen infusion has demonstrated benefits such as >80% and >65% of patients showing improvement in tone and spasticity, respectively, severe side effects due to high baclofen dosages commonly occur. Overdose due to pump and spinal catheter system malfunction, which has occurred in 40% of patients receiving IT baclofen therapy [232], produces symptoms such as respiratory arrest, hypotension, hyporeflexia, quadriplegia, apnea, seizures, autonomic instability, hallucinations, hypothermia, cardiac abnormalities and absence of all reflexes ([233], [234]). Severe withdrawal symptoms such as hallucinations, tachycardia, hyper or hypotension, seizures, rebound spasticity, rhabdomyolysis ([232], [235]) and life threatening complications like coma, may arise due to baclofen overdose [236]. Such problems may be resolved using our proposed magnetically targeted IT treatment where the quantity of drug injected would be minimal as compared to the continuous IT infusion method.

In our *in vitro* model, the barrier magnet prevented escape of MNPs from the spinal canal to the brain region. Such a barrier function that seals the brain from IT delivered drugs could have an important clinical significance. For example, in cases with toxic drugs like baclofen, this barrier magnetic field could serve as a valuable safety net to block drug from reaching the brain. The small amount of MNPs at the barrier magnet could then be guided back down to the target thoracic region by physical translocation. Once within the

target region, the magnet would remain in place until the drug has desorbed from the MNPs and produced a therapeutic effect. The magnets would then be removed, and the bare gold-coated MNPs would become dispersed in the pulsatile CSF due to their superparamagnetic nature and continue transportation into the brain where they would be cleared by the body's natural processes and excreted by the kidneys.

While performing IT-MDT in vivo, biological surfactants such as lecithin [237] or surfactin [238] may enhance biocompatibility and prevent side effects. Even though iron oxide nanoparticles appear to be biologically safe [239], any possible adverse reaction to the magnetite core of the MNPs would be prevented by the gold coating since gold is inert and well tolerated by the human body. Similarly, before implanting a magnet in vivo, it should be coated with a thin layer of biocompatible silicone to reduce the possibility of magnet corrosion and degradation from exposure to physiological conditions. Toxicological studies during subcutaneous and vascular delivery of gold nanoparticles in vivo have also shown no cytotoxic effects [240]. Once the nanoparticles are cleared from the CNS, and if the gold coating happens to desorb from the nanoparticles, magnetite can be metabolized into elemental iron by hydrolytic enzymes and the generated reactive oxygen species regulated by ferritin and transferrin receptors [241]. The iron will then be integrated into the normal body stores and later incorporated into hemoglobin [208].

# APPENDIX B - LICENSES & PERMISSION GRANTED TO USE MY PREVIOUSLY PUBLISHED ARTICLES IN MY DISSERTATION

This is THE COPYRIGHT CLEARANCE from FUTURE MEDICINE- NANOMEDICINE granting permission for use of my article (42) in my PhD dissertation.

Copyright
Clearance
Center

**Confirmation Number: 11603726**
**Order Date: 11/07/2016**

## Customer Information

**Customer:** Indu Venugopal
**Account Number:** 3001081239
**Organization:** Indu Venugopal
**Email:** indu.v30@gmail.com
**Phone:** +1 (979)7774886
**Payment Method:** Invoice

### This is not an invoice

**Order Details**

**Nanomedicine**

| | Billing Status: **N/A** |
| --- | --- |

| | | | |
| --- | --- | --- | --- |
| **Order detail ID:** | 70155830 | **Permission Status:** ✅ Granted | |
| **ISSN:** | 1743-5889 | **Permission type:** | Republish or display content |
| **Publication Type:** | Journal | **Type of use:** | Thesis/Dissertation |
| **Volume:** | | **Order License Id:** | 3983641508114 |
| **Issue:** | | | |
| **Start page:** | | **Requestor type** | Academic institution |
| **Publisher:** | FUTURE MEDICINE LTD | **Format** | Electronic |
| | | **Portion** | chapter/article |
| | | **Title or numeric reference of the portion(s)** | Entire article |
| | | **Title of the article or chapter the portion is from** | Intrathecal magnetic drug targeting using gold-coated magnetite nanoparticles in a human spine model |
| | | **Editor of portion(s)** | N/A |
| | | **Author of portion(s)** | Lueshen, Eric; Venugopal, Indu; Kanikunnel, Joseph; Soni, Tejen; Alaraj, Ali; Linninger, Andreas |
| | | **Volume of serial or monograph** | 9 |
| | | **Issue, if republishing an article from a serial** | 8 |
| | | **Page range of portion** | |
| | | **Publication date of portion** | June 2014 |
| | | **Rights for** | Main product |
| | | **Duration of use** | Life of current edition |

| | |
|---|---|
| **Creation of copies for the disabled** | no |
| **With minor editing privileges** | no |
| **For distribution to** | Worldwide |
| **In the following language(s)** | Original language of publication |
| **With incidental promotional use** | no |
| **Lifetime unit quantity of new product** | Up to 499 |
| **Made available in the following markets** | Worldwide through the University of Illinois at Chicago Library System |
| **The requesting person/organization** | Indu Venugopal/ University of Illinois at Chicago |
| **Order reference number** | |
| **Author/Editor** | Indu Venugopal |
| **The standard identifier of New Work** | PhD dissertation |
| **Title of New Work** | PhD dissertation |
| **Publisher of New Work** | University of Illinois at Chicago |
| **Expected publication date** | Dec 2016 |
| **Estimated size (pages)** | 120 |

**Note:** This item was invoiced separately through our **RightsLink service.** More info          $ 0.00

---

**Total order items: 1**                                          **Order Total: $0.00**

About Us | Privacy Policy | Terms & Conditions | Pay an Invoice

141

This is a statement from *NANO BIOMEDICINE AND ENGINEERING* granting permission for use of my article (45).

---

**M** Gmail                                                    **Indu Venugopal <indu.v30@gmail.com>**

---

**PERMISSION IS GRANTED FOR YOUR ORDER**

2 messages

---

吴筱 <xwu567@sjtu.edu.cn>                                       Wed, Nov 9, 2016 at 8:35 PM
To: ivenug2 <ivenug2@uic.edu>

PERMISSION IS GRANTED FOR YOUR ORDER

Title: Quantum Dot Conjugated Magnetic Nanoparticles for Targeted Drug Delivery and Imaging

Author: Indu Venugopal, Sebastian Pernal, Taylor Fusinatto, David Ashkenaz, Andreas Linninger
Publication: Nano Biomedicine and Engineering
Publisher: Open-Access House of Science and Technology (OAHOST)
Date: Nov. 10, 2016
Copyright© 2016 Indu Venugopal, Sebastian Pernal, Taylor Fusinatto, David Ashkenaz and Andreas Linninger. This is an open-access article distributed under the terms of the Creative Commons Attribution License, which permits unrestricted use, distribution, and reproduction in any medium, provided the original author and source are credited.

---

发件人: "ivenug2" <ivenug2@uic.edu>
收件人: "吴筱" <xwu567@sjtu.edu.cn>
发送时间: 星期一, 2016年 11 月 07日 上午 10:21:15
主题: Re: Permission to use published article in Phd dissertation

Dear Dr. Xiao,

Thank you for your quick response. I am requesting to use the figures and the text of my article in my dissertation document which will definitely include multiple citations to the published article in
Nano biomedicine and engineering.

My university requires us to get permission from the journal for this purpose, despite me being first author.

Thank you very much, and any help on this front would be highly appreciated as I intend to defend my dissertation very soon.

Sincerely,
Indu Venugopal

This is a statement from *MATERIALS RESEARCH EXPRESS* granting permission for use of my article (46).

Journal website (home): http://iopscience.iop.org/journal/2053-1591
Website giving exact statement:
- http://ioppublishing.org/author-rights/
- http://ioppublishing.org/wp-content/uploads/2016/11/J-VAR-LF-0216-Author-Rights-New-7.pdf

---

● post the Accepted Manuscript to an institutional repository or a subject repository (in both cases only where non-commercial) where necessary to comply with the requirements of the HEFCE post-2014 REF policy. The process is as follows:

– for articles with a Date of Acceptance between 1 April 2016 and 31 March 2017, Named Authors may make a Closed Deposit of the Accepted Manuscript to the non-commercial repository within three months of the Date of Publication of the article; or

– for articles with a Date of Acceptance on or after 1 April 2017, Named Authors may make a Closed Deposit of the Accepted Manuscript to the non-commercial repository within three months of the Date of Acceptance of the article; and

– after the Embargo Period, the full text of the Accepted Manuscript may be made available on the non-commercial repository for anyone with an internet connection to read and download

---

## APPENDIX C – MATLAB CODES FOR COMPUTATIONS IN CHAPTER 2

**MATLAB CODE FOR GENERATING THE A and B fields**
```
%Generating A field
clear
close all
clc

mSize = 21;
MPI= zeros(mSize,mSize);
MPO= zeros(mSize,mSize);

dx =1;
dy =1;

e = 9e10;
thr = 10;

while (e>thr)
    for i= 2:mSize-1
    for j= 2:mSize-1
    if(i==11 && j==11); MPO(i,j)=1e4;
    else

    [a1 a2 a3 a4 a5 a6]=computecoefficients(i,j);
    MPO (i,j) = ((a4*(dx/dy)*MPI(i,j-1))+(a2*(dx/dy)*MPI(i,j+1))+(a1*(dy/dx)*MPI(i-
    1,j))+(a3*(dy/dx)*MPI(i+1,j)))/a5 ;
    end
    end
    end
     e=max(max((MPI-MPO).^2))
    MPI = MPO;
end

%Plotting A field
W = MPO;
U = zeros(mSize,mSize);
V = zeros(mSize,mSize);
[X,Y] = meshgrid(0:100,0:100);
Z = zeros(mSize,mSize);
quiver3(X,Y,Z,U,V,W,2);
hold on
surf(U,V);
hold off

% Plotting the gradient of A field
[FX,FY] = gradient(W);
figure()
quiver(FX,FY)

%Plotting the curl of A field
[X,Z] = meshgrid(0:10,0:10);
cav = curl(X,Z,U,W);
```

```
[FcavX,FcavY] = gradient(cav);
figure()
quiver(FcavX,FcavY)

 pcolor(X,Z,cav);
hold on;
quiver(X,Z,U,W,0.5)

[X,Z] = meshgrid(0:100,0:100);
[curlx,curlz,cav] = curl(X,Z,U,W);
pcolor(X,Z,cav);
hold on;
quiver(X,Z,U,W,0.5)

[X,Z] = meshgrid(0:10,0:10);
[curlx,curlz,cav] = curl(X,Z,U,W)
pcolor(X,Z,cav); shading interp
hold on;

% Function used for computing coefficients
function [a1,a2,a3,a4,a5,a6]= computecoefficients(i,j)

a1 = 1/(1.25*10^-6); %N
a2 = 1/(1.25*10^-6); %E
a3 = 1/(1.25*10^-6); %S
a4 = 1/(1.25*10^-6); %W

if i == 2; a1= a1*2; end
if i == 10; a3= a3*2; end
if j == 2; a4= a4*2; end
if j == 10; a2= a2*2; end

a5 = a1+a2+a3+a4;
a6=0;
% if(i==50 && j==50); a6=1000; end
```

**MATLAB CODE FOR GENERATING THE Vm, H and B fields**

```
%Generating H field
clear
close all
clc

mSize = 101;
VmI= zeros(mSize,mSize);
VmO= zeros(mSize,mSize);

dx =1;
dy =1;
e = 9e10;
thr = 1;

while (e>thr)
for i= 2:mSize-1
for j= 2:mSize-1
```

```
[a1 a2 a3 a4 a5]=computecoefficientsthree(i,j);

if(i==50 && j==50);
VmO (i,j) = ((a4*(dx/dy)*VmI(i,j-1))+(a2*(dx/dy)*VmI(i,j+1))+(+400000)+(a3*(dy/dx)*VmI(i+1,j)))/a5 ;
elseif (i==50 && j==51);
VmO (i,j) = ((a4*(dx/dy)*VmI(i,j-1))+(a2*(dx/dy)*VmI(i,j+1))+(+400000)+(a3*(dy/dx)*VmI(i+1,j)))/a5 ;
elseif (i==51 && j==50);
VmO (i,j) = ((a4*(dx/dy)*VmI(i,j-1))+(a2*(dx/dy)*VmI(i,j+1))+(a1*(dy/dx)*VmI(i-1,j))+(-400000))/a5 ;
elseif (i==51 && j==51);
VmO (i,j) = ((a4*(dx/dy)*VmI(i,j-1))+(a2*(dx/dy)*VmI(i,j+1))+(a1*(dy/dx)*VmI(i-1,j))+(-400000))/a5 ;
else
VmO (i,j) = ((a4*(dx/dy)*VmI(i,j-1))+(a2*(dx/dy)*VmI(i,j+1))+(a1*(dy/dx)*VmI(i-
1,j))+(a3*(dy/dx)*VmI(i+1,j)))/a5 ;
end
end
end
e= max(max((VmI-VmO).^2))
VmI = VmO;
end

%Plotting the H field
W = VmO;
U = zeros(mSize,mSize);
V = zeros(mSize,mSize);
Z = zeros(mSize,mSize);
[X,Y] = meshgrid(0:100,0:100);
quiver3(X,Y,Z,U,V,W,2);
hold on
surf(U,V);
hold off

%Plotting the H field
[FX,FY] = gradient(VmO);
figure()
quiver(FX,FY,0.5)
surf(FX,FY)


%Plotting the B field
figure()
quiver(1.25*10^-6*FX,1.25*10^-6*FY,0.5)
surf(1.25*10^-6*FX,1.25*10^-6*FY)

figure()
[startx,starty] = meshgrid(0:100,0:100);
h= streamline(X,Y,1.25*10^-6*FX,1.25*10^-6*FY,startx,starty)
set(h,'Color','red')
view(3)

% Function used for computing coefficients
function [a1,a2,a3,a4,a5]= computecoefficientsthree(i,j)

a1 = 1.25*10^-6; %N
a2 = 1.25*10^-6; %E
```
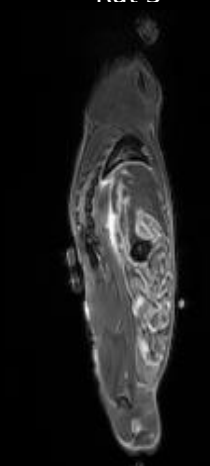
```
a3 = 1.25*10^-6; %S
a4 = 1.25*10^-6; %W

if i == 2; a1= a1*2; end
if i == 100; a3= a3*2; end
if j == 2; a4= a4*2; end
if j == 100; a2= a2*2; end
if (i == 50 && j==50); a4= 0; a1=0; a2 = 1.05*1.25*10^-3; a3 = 1.05*1.25*10^-3; end
if (i == 50 && j==51); a2= 0; a1=0; a3 = 1.05*1.25*10^-3; a4 = 1.05*1.25*10^-3; end
if (i == 51 && j==50); a4= 0; a3=0; a2 = 1.05*1.25*10^-3; a1 = 1.05*1.25*10^-3; end
if (i == 51 && j==51); a2= 0; a3=0; a1 = 1.05*1.25*10^-3; a4 = 1.05*1.25*10^-3; end
a5 = a1+a2+a3+a4;
```
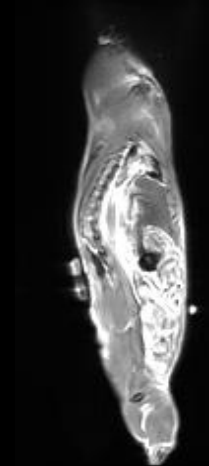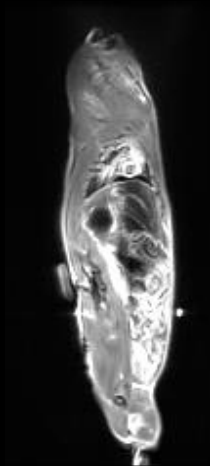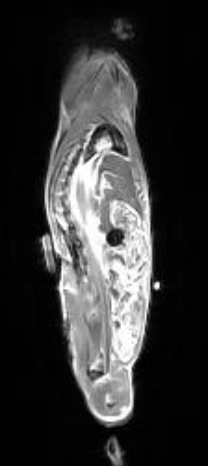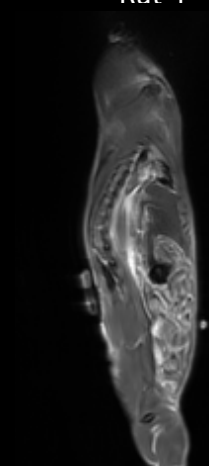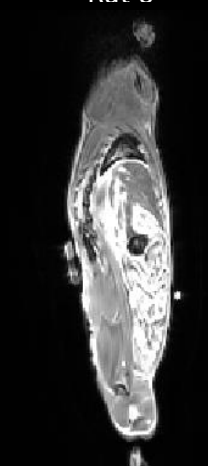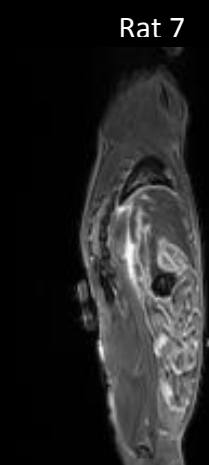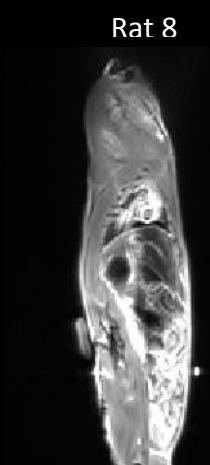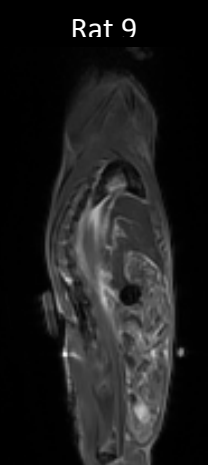
**APPENDIX D – Other MRI images for IT-MDT experiments showing localization of MNPs at target site**

| | | | |
|---|---|---|---|
| **1 hour IT-MDT** | Rat 1 | Rat 2 | Rat 3 |
| **3 hour IT-MDT** | Rat 4 | Rat 5 | Rat 6 |
| **6 hour IT-MDT** | Rat 7 | Rat 8 | Rat 9 |

# VITA

NAME:           Indu Venugopal

EDUCATION:     B.E., Biotechnology, Manipal University, Karnataka, India, 2009

                M.S., Biochemical Engineering, University College London, 2010

                Ph.D., Bioengineering, University of Illinois at Chicago, 2016

HONORS:         Best Masters Research Project award, University College London, 2010

                W.C. and May Preble Deiss Award for graduate research, University of
                Illinois at Chicago, Illinois, 2013

                UIC Graduate Student Council Travel Award, University of Illinois at
                Chicago, Illinois, 2013

                UIC Student Travel Presenter Award, University of Illinois at Chicago,
                Illinois, 2013

PUBLICATIONS: Lueshen, E., Venugopal, I., Kanikunnel, J., Soni, T., Alaraj, A. and Linninger,
                A.: Intrathecal magnetic drug targeting using gold-coated magnetite
                nanoparticles in a human spine model. <u>Nanomedicine</u>. 9: 1155-1169,
                2014.

                Lueshen, E., Venugopal, I., Soni, T., Alaraj, A. and Linninger, A.: Implant-
                assisted intrathecal magnetic drug targeting to aid in therapeutic
                nanoparticle localization for potential treatment of central nervous system
                disorders. <u>Journal of biomedical nanotechnology</u>, 11: 253-261, 2015.

                Venugopal, I., Sirhan, R., Basati, S. and Linninger, A. A.: Prototype
                Biosensor for Detection of Myelin Basic Protein Biomarker in
                Hydrocephalus Diagnosis. <u>Sensor Letters</u>, 14: 84-92, 2016.

                Venugopal, I., Pernal, S., Fusinatto, T., Ashkenaz, D. and Linninger, A.:
                Quantum Dot Conjugated Magnetic Nanoparticles for Targeted Drug
                Delivery and Imaging. <u>Nano Biomedicine & Engineering</u>, 8: 24-38, 2016.

                Venugopal, I., Pernal, S., Duproz, A., Bentley, J., Engelhard, H., and
                Linninger, A.: Magnetic field-enhanced cellular uptake of doxorubicin